SMALL-ANGLE X-RAY SCATTERING STUDIES OF NANOSTRUCTURED RESPIRATOR AND BATTERY MATERIALS

by

Matthew J. McDonald

Submitted in partial fulfillment of the requirements

for the degree of Master of Science

at

Dalhousie University

Halifax, Nova Scotia

October 2013

TABLE OF CONTENTS

LIST OF TABLES

LIST OF FIGURES

ABSTRACT

This work represents a small-angle X-ray scattering (SAXS) investigation into the structure of two rather different materials: chemically impregnated activated carbons (IACs) and the nanostructured alloy of tin-cobalt-carbon.

Five impregnant species, namely sodium benzoate, potassium biphthalate, zinc chloride, potassium carbonate, and silver nitrate, were impregnated into activated carbon using the incipient wetness or imbibing method to various loadings and examined. Using a modified version of the Kalliat model and a suitable interpretation, two different impregnant behaviours arose: one marked by good chemical dispersion over all classes of carbon pores, the other characterized by a formation of large grains but little deposition in micropores or formation of small grains.

A special apparatus was constructed to collect SAXS data of Li-ion coin cells with beryllium windows using a nanostructured SnCoC electrode. When one such cell was charged and discharged, the entry and exit of lithium atoms into the SnCoC material caused structural deformations, which were visible in SAXS data through the use of the modified Kalliat model. The size of the SnCo grains changed as lithium was inserted and removed from the SnCoC electrode. However, when the cell voltage was less than 0.2 V the SnCo grain size was constant, suggesting lithium insertion and removal below 0.2 V was occurring in the carbon matrix.

LIST OF ABBREVIATIONS AND SYMBOLS USED

A, B_{gr}, C_{mi}, D	constants used in Kalliat model
a, b	Debye autocorrelation lengths for pores and grains
A_{beam}	cross sectional area of the incident beam
AC/IAC	activated carbon / impregnated activated carbon
A_{sample}	cross sectional area of the sample
$A(\boldsymbol{q})$	scattering amplitude at direction $\boldsymbol{q}$
BET	Brunauer-Emmett-Teller
d_{hkl}	distance between crystal planes of identification (hkl)
f	scattering factor, form factor (SAXS), atomic form factor (WAXS)
GC	Kuraray GC brand activated carbon
$Icalc_i$, $Idata_i$	calculated, experimental data points
I_e	scattering intensity from a free electron
$I(\boldsymbol{q})$	scattering intensity at direction $\boldsymbol{q}$
I_X	scattering intensity of sample
I_0	scattering intensity of background, incident beam intensity
I_{0K}	Kalliat constant
$\boldsymbol{K}$	scattered beam direction
$\boldsymbol{K_0}$	incident beam direction
KHP	potassium biphthalate
m, M	sample mass
$m_{initial}$	mass before impregnation

m_{final}	mass after heating
n	number of particles, fractal dimension for Kalliat model
N	number of particles
NaBz	sodium benzoate
$\boldsymbol{q}$, q	scattering vector, magnitude of scattering vector
Q	invariant (SAXS)
$\boldsymbol{r}$	distance vector
R, R_{sp}	radius of a hard sphere / radius of a spherical pore
r_e	classical radius of the electron
R_g	radius of gyration
SAXS	small-angle X-ray scattering
SEM	scanning electron microscopy
$S(q)$	structure factor
t	sample thickness
t_x	transmission of sample
Type A, Type B	impregnant behavioural classifications
V	volume of concern
V_{gr}	micrograin volume
V_{xmi}	volume of impregnant in micropore
V^0_{mi}	micropore volume
WAXS	wide-angle X-ray scattering
x	volume fraction of impregnant in micropore
XRD	X-ray diffraction

$\gamma(r)$	correlation function
η	electron density fluctuation
η^2_{av}	average squared fluctuation from mean electron density
2θ	scattering angle
λ	X-ray wavelength
μ	coefficient of X-ray absorption, mean
ρ, $\rho(\boldsymbol{r})$	mass density, electron density, electron density at position $\boldsymbol{r}$
ρ_{av}	average electron density
ρ_x	electron density of impregnant
σ	standard deviation
φ	phase difference, void fraction
χ^2	fitting error
$\wp(\boldsymbol{r})$	autocorrelation function

ACKNOWLEDGMENTS

I would first like to thank my supervisor, Dr. Jeff Dahn, for his support, patience, encouragement, helpfulness and willingness to teach. I have learned a lot during my time here and I consider it to have been a very great opportunity for me to come to Halifax and do research with the Dahn group.

I would also like to thank all the Dahn Lab members past and present that I have collaborated with and received help from over the past couple years, especially Jock Smith, John Camardese, Robbie Sanderson, Deijun Xiong, Chris Burns, Remi Petibon, Eric McCalla and others. Thanks for making this time a very pleasant one. Simon Trussler also deserves recognition for his help in the construction of various special SAXS holders and pieces. Thanks also go out to NSERC and 3M for funding (and in the latter case, samples!).

Finally, I'd like to express gratitude to my family and Monica, whose encouragement and support has helped me on days where data analysis wasn't quite going as well as possible.

CHAPTER 1 INTRODUCTION

1.1 INTRODUCTION

Small-angle X-ray scattering (SAXS) is a very useful tool for examining the structure of a variety of materials with nanometer-scale features, especially when complemented with other scientific techniques like electron microscopy. Generally, SAXS is most effective when studying materials with feature sizes from a few angstroms to a few dozen nanometers, such as carbonaceous materials, sputtered thin films, polymers, and colloidal suspensions [1-7]. Modern SAXS equipment promises quick data collection at excellent resolution and the ability to probe materials in many different forms such as powders, liquids, and thin films. Decades of theoretical work and advances in computational power and technique have also contributed to a significantly improved outlook for modeling the scattering intensity from more complicated systems [8-9]. This thesis represents an investigation into the structure of two rather different materials: chemically impregnated activated carbons (IACs) and the nanostructured Li-ion battery electrode material alloy of tin-cobalt-carbon.

Microporous activated carbons are widely used in filtration systems for liquids and gases [10-12]. They can contain different classes of pores, such as micropores ($\leq$ 20 Å in width), mesopores (20-500 Å in width) and macropores ($\geq$ 500 Å in width) [13] and generally function by trapping unwanted chemicals via adsorption to pore walls. Figure 1.1 a) and b) show the pore structure of a microporous carbon, while c) and d) show the

atomic structure of a microporous carbon, which illustrates that topological defects in the graphene sheets that make up the larger structure can cause rippling and the presence of micropores [14].

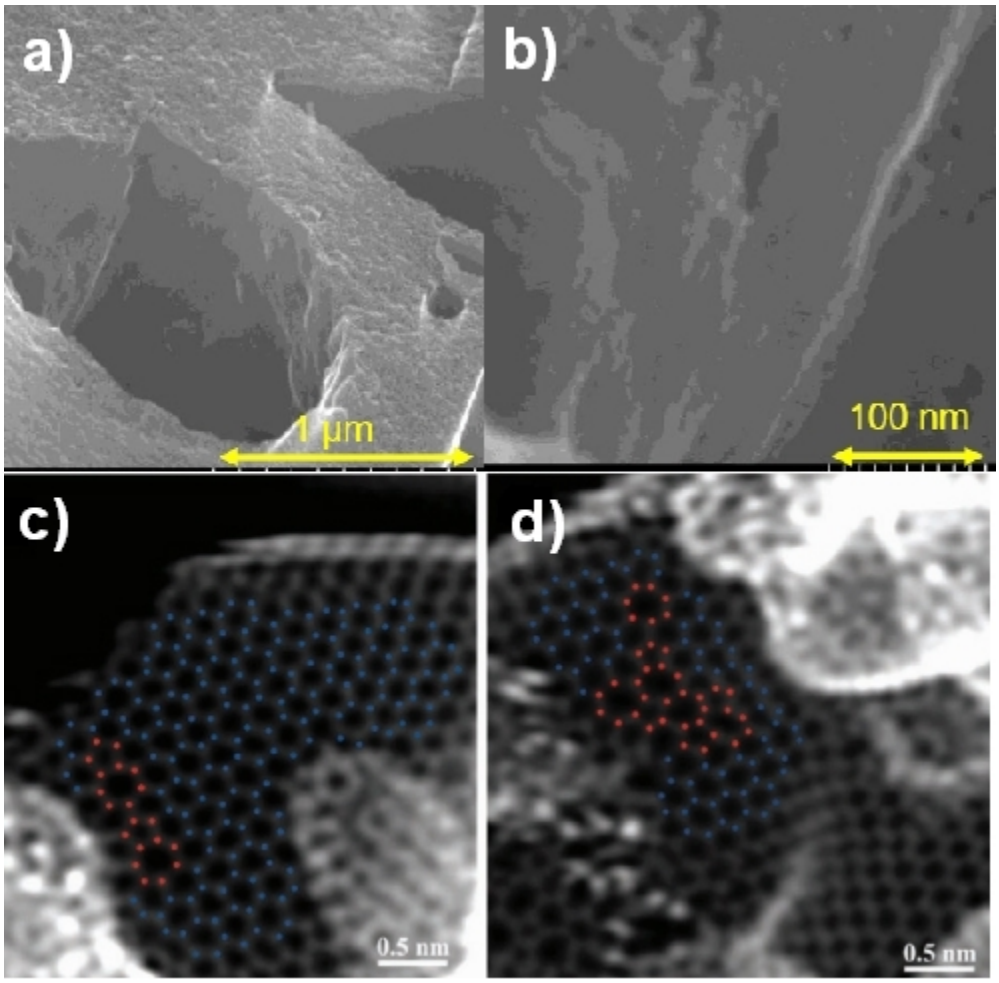

Figure 1.1 A set of scanning electron microscopy images of microporous activated carbon. a) and b) show details of the pore structure, while c) and d) show the lattice structure of the carbon matrix. In c) and d), hexagonally latticed atoms are shown in blue, while defects are marked in red. Adapted from Figure 1.2 of [15] and 3 of [14].

In the presence of acid gases, organic vapours, mercury, or other industrial pollutants, impregnation of activated carbons with various compounds can greatly increase the effectiveness of the base material by either helping to adsorb or to react with the species to be filtered [16-18]. Often, efficient filtering depends on a good distribution of impregnant within the activated carbon pores, as opposed to a predisposition to form large grains [19, 20]. It is thus important to know how the impregnant is distributed in the pores of various sizes within the activated carbon host. This can be quickly and easily accomplished with SAXS.

Activated carbon can be impregnated with a wide variety of chemical species using the incipient wetness or imbibing method [21, 22], described in detail in Chapter 2. The scattering data from such samples can be modeled using a modified form of the Kalliat model [4], described in Chapter 3. The parameters of this model can then be used to compare impregnant distribution differences between samples. The results of Kuraray GC brand activated carbon samples impregnated with several different chemical species (sodium benzoate, potassium biphthalate, zinc chloride, potassium carbonate, and silver nitrate) to a variety of loadings and examined using SAXS are given in Chapter 4. The conclusions drawn from the study suggest that impregnants tend to behave in one of two broad categories. In the first type the impregnant fills micropores and forms impregnant grains in meso- and macropores, whose number tends to increase with loading. In the second type the impregnant mainly agglomerates in the macropores, having little effect on micropores or the smaller mesopores which remain substantially devoid of impregnant.

Tin-cobalt-carbon (SnCoC) alloys have been previously studied in some depth, beginning with the release of the Sony Nexelion^{TM} commercial lithium-ion battery [23]. It can be broadly described as SnCo grains, around 5 nm in size, surrounded by a carbon matrix. Figure 1.2 shows an illustration of this structure. This material makes an effective electrode material for use in lithium-ion batteries. As a cell is charged and discharged, the entry and exit of lithium ions to the SnCoC material causes structural deformation [24], which is visible in SAXS data. In the work described by this thesis, nanostructured $Sn_{30}Co_{30}C_{40}$ material was created using ball milling, described in Chapter 2, coated on copper foil, and used to create a Li/$Sn_{30}Co_{30}C_{40}$ cell that was charged and discharged while SAXS data was taken. This is the first work directly examining the mechanism of lithiation of SnCoC. The results, given in Chapter 5, show a definite change in feature size with lithiation and effectively describe the lithiation processes of the different components of the alloy at different voltages.

Data collection of the IAC samples required little more than stock sample holders and tools as well as the NanoSTAR SAXS machine discussed in Chapter 2. However, examining the SnCoC material with SAXS presented additional problems as it was desired to be able to lithiate and delithiate the SnCoC in a coin cell while simultaneously taking X-ray data in transmission mode (i.e, with X-rays permeating through the entire cell). The solution to this problem, found in more detail in Chapter 2, involved using beryllium discs in place of the more traditional components of a coin cell, and creating a special coin cell holder and charging device.

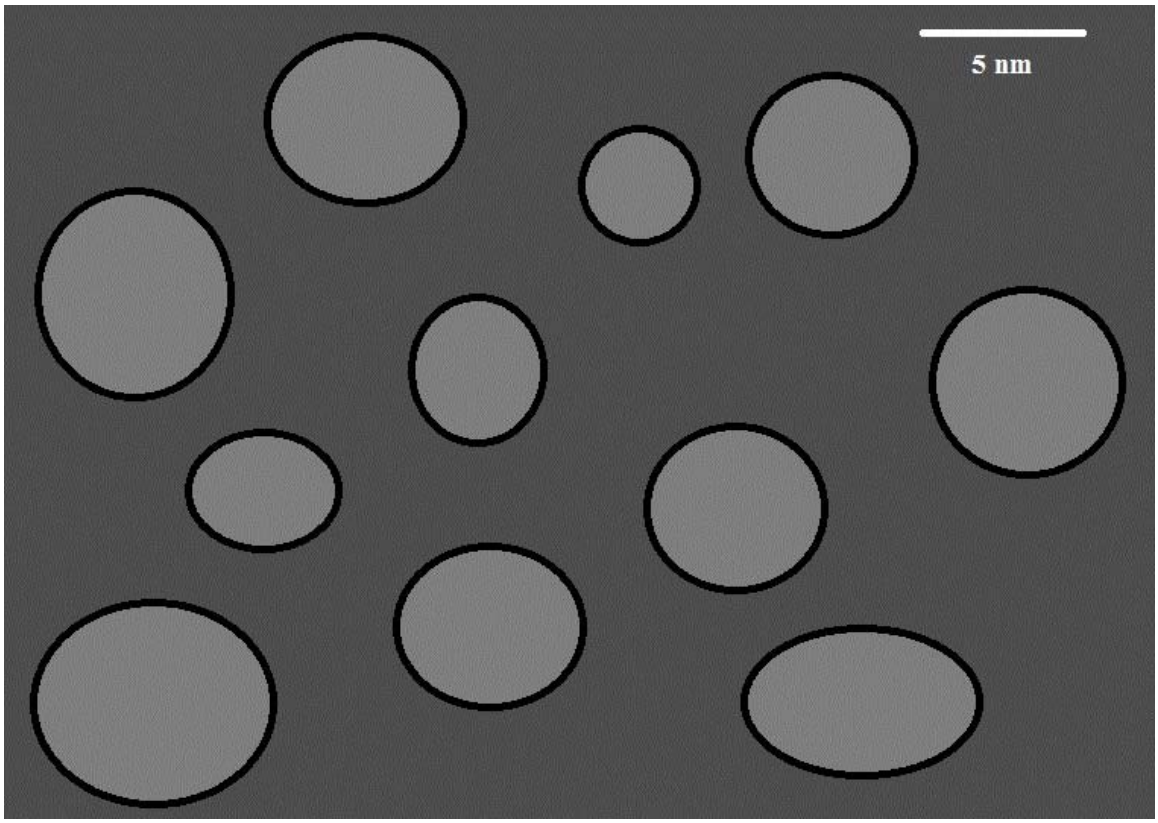

Figure 1.2 A depiction of the structure of the SnCoC material, with SnCo grains of approximately 5nm suspended in a carbon matrix.

CHAPTER 2 EXPERIMENTAL TECHNIQUES & EQUIPMENT

2.1 MATERIALS STUDIED

For the activated carbon impregnation studies, solutions were prepared from reagent-grade sodium benzoate ($NaC_7H_5O_2$ or NaBz, 1.2 M), potassium biphthalate ($KC_8H_5O_4$ or KHP, 0.58 M), zinc chloride ($ZnCl_2$, 4.9M), potassium carbonate (K_2CO_3, 1.08 M), and silver nitrate ($AgNO_3$, 2.5 M), obtained from Sigma-Aldrich. These were chosen on the basis of contact angle results, solubility, and lab availability. As electronic density contrast gives rise to SAXS intensity, examined in more detail in Chapter 3, Table 2.1 contains the electronic densities of the chemical species used.

The impregnated activated carbon samples were prepared using Kuraray GC (a product designation: GC does not indicate glassy carbon) from Kuraray Chemical Co. in Osaka, Japan. This coconut-shell derived carbon has a particle mesh size of 12 × 35 (corresponding to a particle size of about 1.70 mm by 0.5 mm) and an ash content of about 0.4% (weight/weight). The Brunauer–Emmett–Teller (BET) surface area [25] has been determined by nitrogen adsorption to be 1570 ± 50 m^2/g [26]. Boehm titrations [27] have been performed on Kuraray GC in previous work [21, 22], which reported a total of ≤ 0.18 mmol / g of acidic surface groups.

Species	Electronic density (e^-/cm^3)
Carbon *(graphite)*	6.827×10^{23}
$NaC_7H_5O_2$	4.628×10^{23}
$KC_8H_5O_4$	5.028×10^{23}
$AgNO_3$	1.203×10^{24}
$ZnCl_2$	8.216×10^{23}
K_2CO_3	6.783×10^{23}
Ag	2.752×10^{24}
H_2O (*l*)	3.344×10^{23}

Table 2.1 Electron densities for the chemical impregnants used. Included are graphitic carbon and liquid water for comparison as well as metallic silver, which forms in carbons imbibed with silver nitrate. All species have electron densities within a factor of four of that of graphite.

SAXS was used to examine nanostructured SnCoC material for use as lithium-ion cell electrodes as well. This alloyed material was produced using a process known as roller milling. Similar to other similar manufacturing processes such as ball milling and attritor milling, this involves placing the constituent powders of a sample into a disc-like chamber along with metal ball bearings, and mechanically rotating the chamber at a constant frequency (here, around 100 rpm). The procedure creates composite materials by using collisions between a sample's constituent powders, ball bearings, and the walls of the chamber to fracture and cold weld the different constituents together [23].

The SnCoC alloyed material had atomic ratios of 30, 30, and 40 for tin, cobalt and carbon respectively and was produced in a batch of 30g. The structure of this material can be described as SnCo grains, 5 nm in size or larger, surrounded by a carbon matrix [28]. These grains change in size as a cell is cycled and the grains are lithiated and delithiated, and this process is visible through SAXS as shown in Chapter 5.

Figure 2.1 shows that wide-angle X-ray diffraction peaks of this material were very broad and located at scattering angles of about 32 and 43 degrees, which compares well with earlier studies of SnCoC [23].

2.2 THE IMBIBING METHOD OF IMPREGNATING POROUS MATERIAL

One method of filling a porous material with a chemical species is called the imbibing or incipient wetness process [21, 22]. For small, laboratory-scale samples, this process involves using a pipette to evenly distribute a fixed amount of solution of a given species into a glass jar containing a mass of activated carbon that has been previously oven-dried under air at 120°C for several hours to remove latent moisture. The jar containing the activated carbon and solution is then sealed and shaken until the carbon appears dry, having fully absorbed the chemical solution. During this stage, impregnant molecules will adsorb to carbon pore walls with their affinity for the carbon measurable by taking contact angle data [22]. Depending on the species, the impregnant may also react with naturally present surface groups or other co-impregnants. Typically, each solution will have an imbibing limit, measured in mL of solution per gram of carbon and determined

by inspection: it is where small grains of the carbon began to stick to the walls of the container, yet an inspection of the sample revealed no obvious carbon surface wetness.

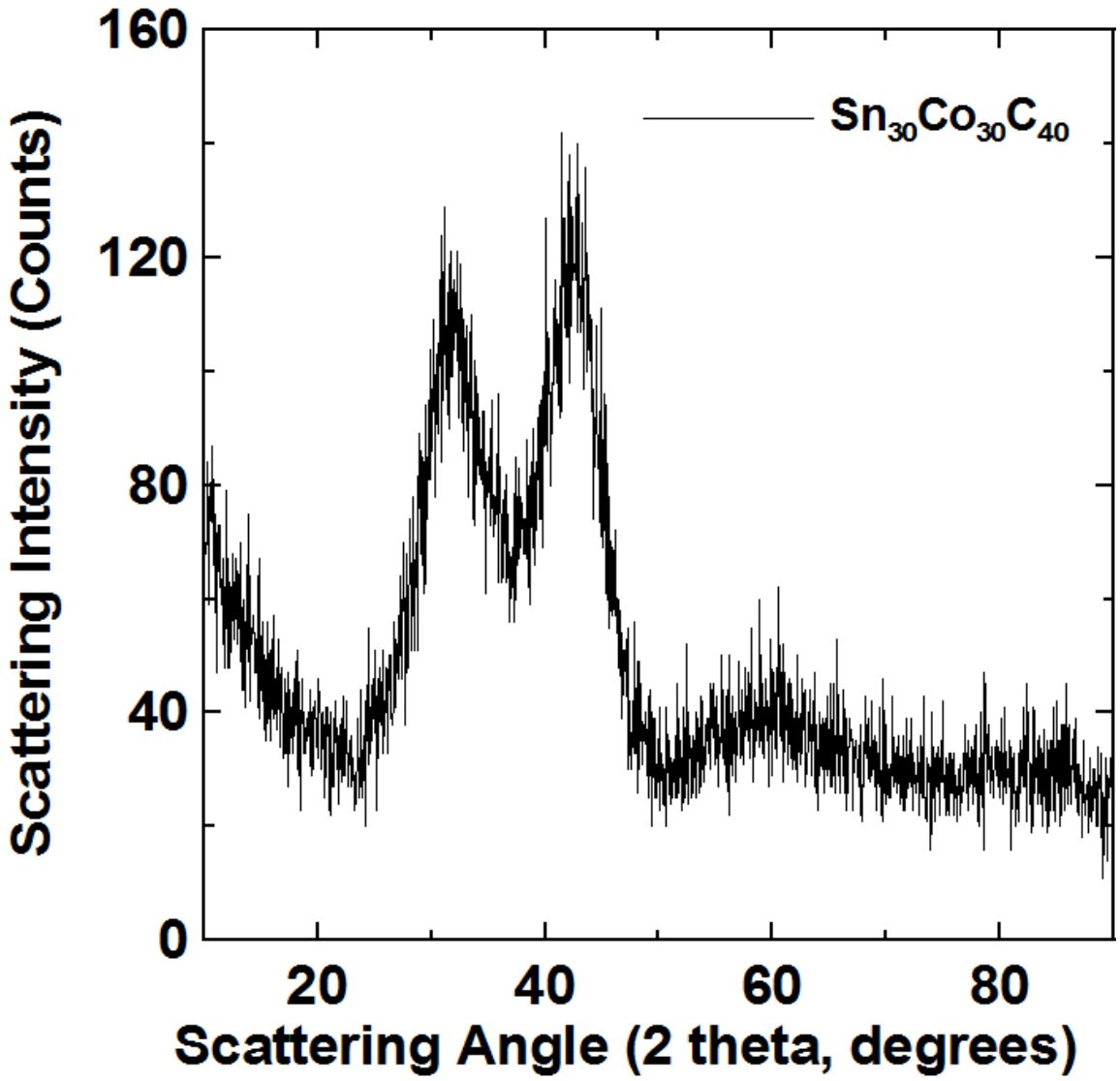

Figure 2.1 Wide-angle X-ray scattering data of the $Sn_{30}Co_{30}C_{40}$ material produced. This sample was milled for approximately 250 hours. The peaks match those of $Sn_{30}Co_{30}C_{40}$ that have been carefully characterized in reference [23].

This is shown in Figure 2.2 b), where a small fraction of granules are beginning to stick to the glass jar, while Figure 2.2 a) shows an underimbibed carbon with visibly dry grains and panel c) shows an overimbibed carbon with visibly wet grains. If necessary, impregnant solutions can be diluted to preserve the imbibing limit in cases where lower loadings are desired.

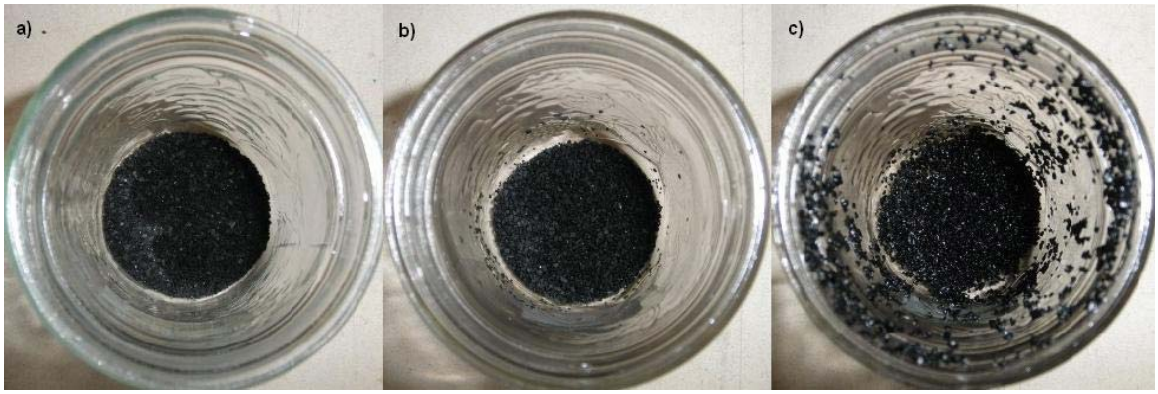

Figure 2.2 An example of the incipient wetness or imbibing method. Panel a) shows a sample of activated carbon that has been under-imbibed. The carbon granules are dry and move freely. Panel b) shows carbon at the imbibing limit, where grains are beginning to stick to the walls of the container and to each other, though no obvious wetness is present. Panel c) shows over-imbibed carbon, where excess fluid is visible and granules attach in groups.

The fully imbibed material is then placed in an alumina boat or other stable, non-reactive holder and dried in an oven under air at 120°C for approximately two hours. This temperature will dry the sample but for most species will not cause an impregnant to undergo a chemical reaction: if this is the case, the drying temperature can be altered or

the drying can be completed in a different environment. The desired chemical loading can be defined as:

$$\% \text{ loading} = 100\% \times (m_{final}-m_{initial})/m_{initial}, \quad (2.1)$$

where $m_{initial}$ is the mass of the dry, un-impregnated activated carbon and m_{final} is the mass of the carbon after heating. Where necessary, the imbibing process is repeated after drying to achieve this desired loading. As the impregnant loading increases, the imbibing limit for the next imbibe tends to decrease as carbon pores fill with impregnant and so there is a maximum to the number of imbibing steps possible which varies from species to species.

All samples studied were based on impregnated Kuraray GC. For the species listed in Section 2.1, the first imbibing used 0.70 mL/g carbon for all species except $AgNO_3$, which accepted 0.80 mL/g. Imbibing limits decreased substantially beyond the first imbibings, as evidenced in Chapter 4, and so extrapolating implied maximum loadings studied by SAXS were within about 10% of the highest that could be achieved. Each sample contained 5 g of dry carbon before impregnation and no evidence of chemical reaction was witnessed during the oven drying phase of the imbibing process. Samples were weighed before and after imbibing steps using a Sartorius balance with an accuracy of ± 1 mg. The uncertainty in the determined loading through this process is roughly 1-3 %, since activated carbon uptakes atmospheric water vapour during weighing, relocation or storage.

2.3 THE IN-SITU SAXS CELL

The construction of a coin cell for use in transmission-mode small-angle X-ray scattering experiments poses unique challenges. X-rays need to penetrate through the entire cell without an unacceptable amount of signal absorption or noise from the contents not under examination, but otherwise the cell should be comparable in form and function to any other. The cell should be able to operate under vacuum and easily connect to a charging system.

The primary solution to these issues is to use beryllium in the form of thin discs placed in the coin cell. Beryllium has a low atomic number and is thus relatively permeable to X-rays, is a stable metal in air and argon at the assembly and experimental conditions of atmospheric to medium vacuum pressures (about 60 mTorr) and room temperature, and does not corrode when placed next to lithium in a coin cell until charged to the relatively high voltage of about 4 V. A typical coin cell consists of a can, electrodes, separators, electrolyte, metal spacer & spring, and cap. In the in-situ X-ray coin cells constructed, the cap and can of the coin cell are cut out to make room for beryllium discs, the discs are glued to the cap and can with Roscobond adhesive, and the cell is constructed as normal but with the spacer and spring removed to maintain the stack height of the coin cell (and to increase the X-ray permeability of the cell). A diagram of such a cell is shown in Figure 2.3.

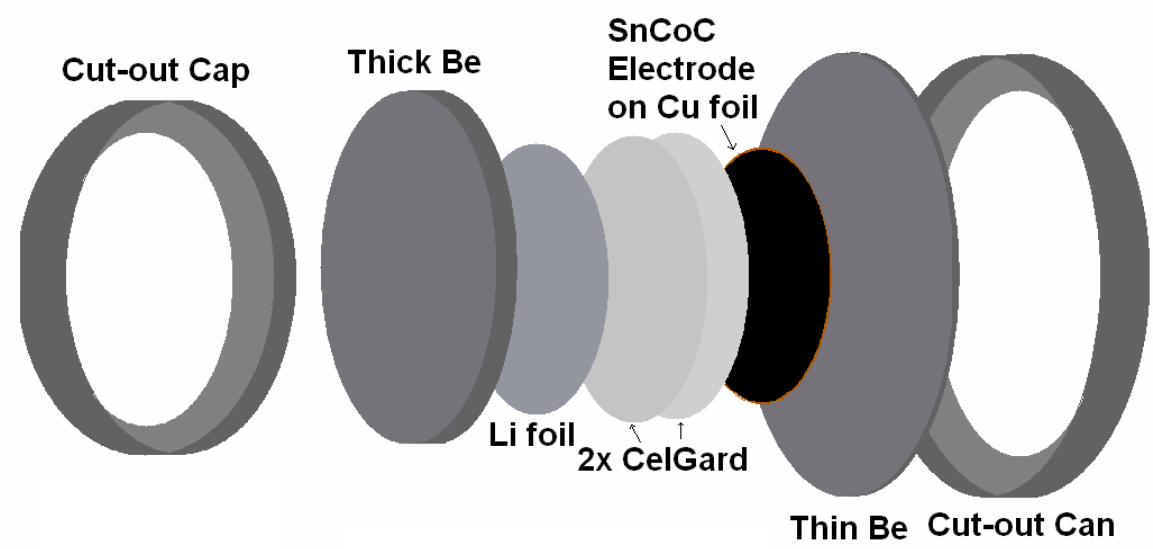

Figure 2.3 The components of the transmission-mode in-situ coin cell with SnCoC electrode. Beryllium discs are glued to the cap and can with Roscobond brand adhesive.

As depicted in Figure 2.3, the SnCoC electrodes studied were deposited on copper foil of thickness 35 microns, but electrodes can also be deposited directly onto the beryllium discs to improve the signal to noise ratio. It is important to construct a "dummy cell" of all the materials except the electrode of interest in order to get a signal that can be subtracted from the full cell. This process, detailed in Section 2.4, will yield the scattering data of the SnCoC electrode without the contributions from copper, lithium, etc.

Table 2.2 gives the thicknesses of each of the materials in the in-situ SAXS coin cell. When the cell is constructed, all seams must be sealed with a vacuum-safe epoxy such as Torr seal. Electrical conductivity between the cap, can and respective beryllium discs must also be ensured as the Roscobond may provide an insulating barrier. This can be done by using silver paint and a few mm of soldering wire to act as a conductive lead.

Finally, metal "tabs" can be carefully placed on the outer region of the cap and can, away from the beryllium discs, and the coin cell is ready for experimentation. An in-situ cell is shown in Figure 2.4 without the Torr seal, silver paint, and tabs for clarity.

Material	Thickness (microns)
Beryllium (can)	525 ± 5
Cu foil	35 ± 5
SnCoC Electrode	10 ± 5
Separator (ea.)	25 ± 5
Lithium foil	125 ± 5
Beryllium (cap)	1435 ± 5
Total (excl. cap/can)	2180 ± 40

Table 2.2 Thicknesses of the various materials used in construction of the in-situ SAXS coin cell. The two beryllium discs vary in both thickness and radius: the can disc has radius 1.05 cm, while the cap disc has radius 0.875 cm.

2.4 EQUIPMENT USED

A pinhole collimated Bruker-AXS NanoSTAR equipped with a 30W microfocus Incoatec IμSCu source and Vantec-2000 area detector was used to collect small-angle X-ray scattering data and is shown in Figure 2.5. The generator operated at 40kV and 650 μA,

and a 400 μm diameter beam of Cu-Kα (1.5418 Å) radiation was selected using pinholes and a set of Göbel mirrors. Scattering angles ranged from 0.23 to 5.00^{o}.

Figure 2.4 The transmission-mode in-situ coin cell viewed from the can, with scale. Normally, Torr seal would be used in the seam to prevent loss of electrolyte under the operating vacuum of SAXS, and silver paint and conducting wire placed from the can to the central beryllium disc.

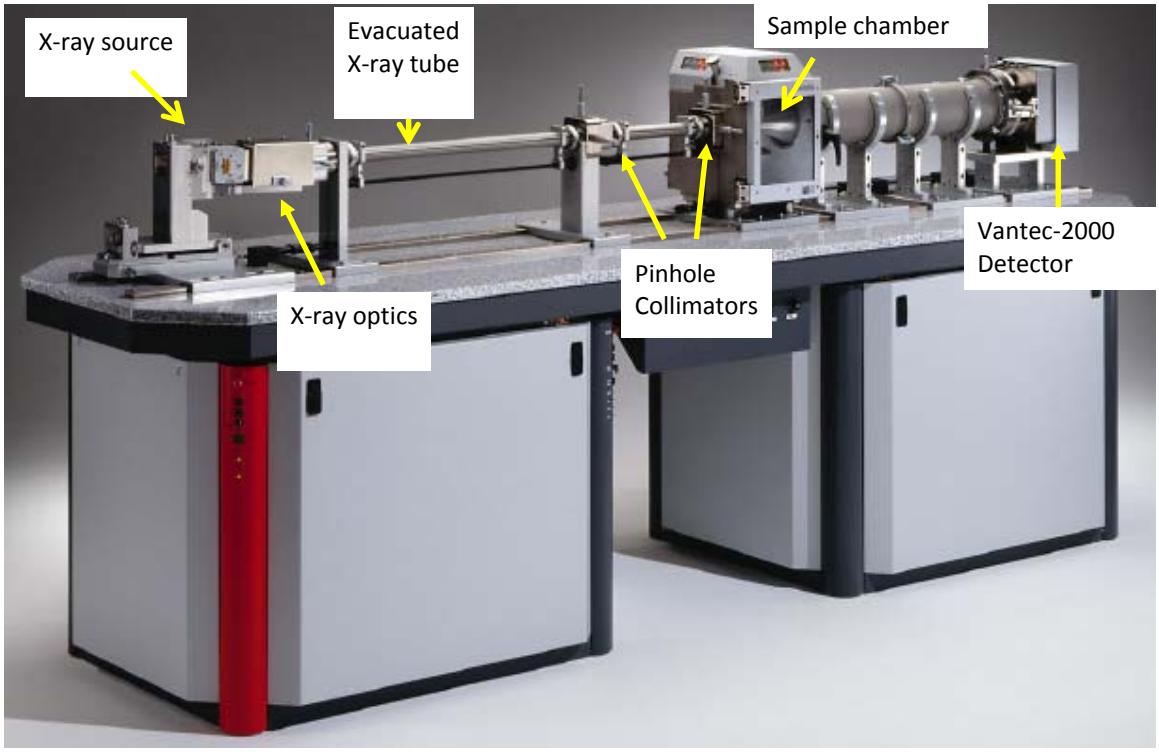

Figure 2.5 The NanoSTAR SAXS machine with components labeled. Taken from the Bruker-AXS NanoSTAR manual.

For activated carbon samples, the sample holder consisted of a 1.62 mm thick stainless steel plate with nine rectangular holes of width 0.7 cm and height 0.3 mm, each vertically separated by 1.00 cm. 10-20 mg (higher loaded samples having greater densities in the same volume) of the activated carbon was ground into a fine powder with a mortar and pestle and packed into the plate openings, supported by a layer of Scotch brand adhesive tape on each side. A holder with several loaded samples is shown in Figure 2.6. Data were collected for 3000 s per sample.

Figure 2.6 The carbon holder attachment with three samples loaded. Adhesive tape covers the front and back of the samples. The holder is screwed on to a triangular-shaped metal attachment that slots directly into the NanoSTAR sample stage.

For in-situ coin cells, a specialized holder was constructed that allowed the "slotting" of the cell while alligator clips connected to the leads, shown in Figure 2.7. The four-wire charging system exited the NanoSTAR system via a KF-40 feedthrough flange, and an external cable led to the charger, a Maccor Series 4000. Data was collected continuously over set intervals, intending to capture different states of electrode lithiation. Exact timing depended on the charging currents and voltages, though data was generally taken for

3000 s per "snapshot". SnCoC coin cells were typically cycled from 0.005 V to 1.200 V at constant current of 45 μA, with more detail given in Chapter 5.

Since the incident beam intensity can vary slightly from dataset to dataset, and within sets of nine impregnated carbon samples, incident intensity was standardized and data corrected to take this into account. As well, sample mass absorption was taken into account by dividing by the transmission factor, calculated using the following relation:

$$t_X = \frac{I_{X+GC} - t_{GC} \times I_X}{I_{GC} - t_{GC} \times I_0}, \tag{2.2}$$

where t_x is the transmission of the sample, t_{GC} is the known transmission factor of a glassy carbon standard, and for a set length of time, I_{X+GC} is the number of detector counts that result from placing the sample and glassy carbon in the beam, I_X is the number of detector counts from the sample alone, I_{GC} is the number of detector counts from the glassy carbon alone, and I_0 is the number of detector counts from the background (tape, solvent, vacuum, etc). The transmission factor can be cross-checked with reference absorption data [29]. Comparison between experimentally observed and calculated transmission factors for a variety of different IACs has shown agreement within approximately ± 10% [30]. This process of correcting for beam intensity and mass absorption is called “normalization” in Chapters 4 and 5.

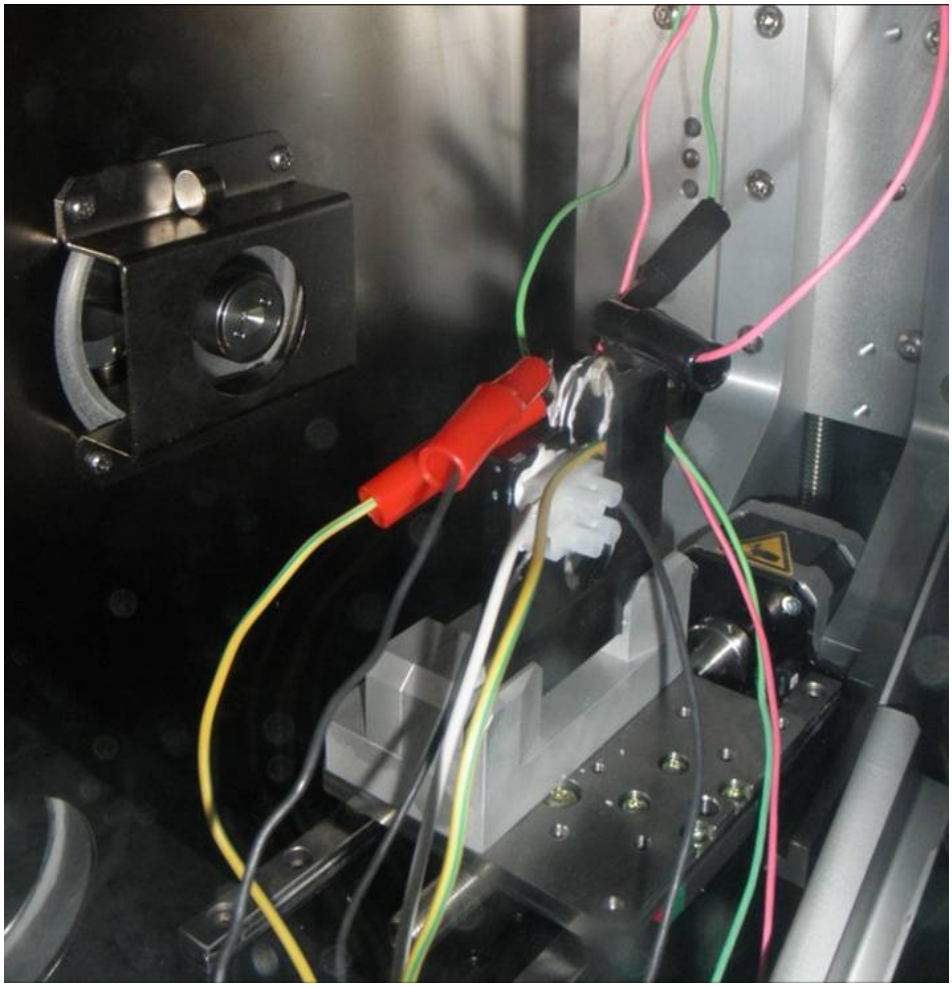

Figure 2.7 An in-situ coin cell connected to the charger and placed in the "slot" holder. On the left is the X-ray beam pinhole leading to the sample chamber. The sample stage is visible here: it can move sideways and vertically.

Useful signal can be separated from unwanted signal if the transmissions of both components and the signal from the unwanted component are known. For a two-component system made up of materials A and B, the total intensity I_{a+b} is simply the sum of contributing intensities:

$$I_{a+b} = \frac{I_{(a+b)m}}{t_{a+b}} = \frac{I_{am}}{t_a} + \frac{I_{bm}}{t_b} = I_a + I_b, \tag{2.3}$$

where I_{am} and I_{bm} are the measured intensities of components *A* and *B*, *m* signifying "measured", and t_a, t_b, and t_{a+b} are the transmission factors for components *A*, *B*, and the total system respectively. Since $t_{a+b} = t_a t_b$, if $I_{(a+b)m}$, t_{a+b} or t_a, and t_b are known, then a simple rearrangement of the equation will give I_a, the signal from the wanted component.

Absolute calibration of the direct beam was completed by finding the transmission of a 200 μm thick piece of Cu foil through the process described above, removing the beam-stop from the nanoSTAR, and counting the amount of photons hitting the detector per second, adjusting for detector efficiency and Cu foil transmission. The result can be written in photons/s·m^2 or, using Planck's constant and the frequency of X-rays, converted into W/m^2. In conjunction with the Thomson equation for a free electron described in Chapter 3, the energy per second scattered from an electron in a given direction can then be calculated in photons/s, Watts, or detector counts/s in order to calculate absolute quantities of certain variables.

Wide-angle X-ray scattering data was collected using a JD-2000 diffractometer utilizing a Phillips PW 1720 X-ray generator operating at 40 kV and 30 mA. A Cu target X-ray tube was combined with a diffracted beam monochromator to select Cu-Kα radiation. The operating parameters include a 1.0 s dwell time per 0.05^o step.

A Hitachi S-3400 cold field emission scanning electron microscope was used to examine sample morphology.

2.5 FITTING

While modeling, fitting parameter error can be minimized using a standard least-squares routine over the entire range of data between experimental and calculated data points, with χ^2 as the measure of the goodness of fit:

$$\chi^2 = \sum_{i=1}^{n} (\ln(Icalc_i)) - (\ln(Idata_i))^2 . \quad (2.4)$$

CHAPTER 3 SAXS THEORY & MODELS

3.1 WHAT IS SCATTERING AND WHY IS IT DONE?

The scattering of particles and waves is a very wide field that includes both small- and wide-angle X-ray scattering, neutron scattering, and ordinary diffraction of light as illustrated by the famous double-slit experiments of Thomas Young in the early 1800s. Scattering theory includes both elastic scattering, where the source photons, neutrons, etc do not lose energy (kinetic or otherwise) as they bounce away from the sample, and the generally more complicated inelastic scattering, where energy is lost. Many scientific apparatuses, especially those in material science where the size, structure, identification or other properties of a particular material are being examined, use the principles of elastic scattering in their design. The general goal behind any elastic scattering experiment is to be able to model the resulting intensity (defined variously) of scatterers, typically given as a function of scattering angle, in terms of some parameters of the target material. One thing that ties all the disparate applications of elastic scattering together is the Fourier transform. This essentially allows the prediction of the intensity of scattered objects at a given point, given some properties of the source and sample and the spatial variability of the sample. Alternatively, it enables the discovery of the distribution and form of the sample given the intensity of the scatterers, which makes it ideal for scattering experiments.

Small-angle X-ray scattering (SAXS) is one physical application of the Fourier transform. In particular, it is a branch of X-ray diffraction (XRD), made possible by some convenient properties of the scattering of X-rays at low angles and generally applied to materials with specific properties such as a lack of long-range order. For example, these conditions tend to exclude crystals from study, the focus of the other branch of XRD, wide-angle X-ray scattering (WAXS). However, to understand and use SAXS the general application of the Fourier transform and the theory of physical scattering of X-rays must be first covered.

3.2 X-RAY DIFFRACTION THEORY BASICS

When X-rays are incident upon matter, they lose some of their initial intensity. This is because X-rays interact with matter in several different ways: some may be absorbed by atoms by the photoelectric effect, leading to fluorescence or Auger electrons, while some merely change their direction, wavelength, or both, and pass through the substance [31]. In fact, a material-dependent coefficient of absorption μ can be determined easily: the decrease in intensity in an X-ray beam passing through matter has been experimentally found to be proportional both to the intensity of the beam and also the mass per unit area of the substance. This can be stated mathematically:

$$dI = -\mu I dm, \tag{3.1}$$

where *dI* is the (negative) change in intensity of the beam passing through a slice of material with thickness *dz*, *I* is beam intensity, and *dm* is the mass per unit area. Integrating Equation 3.1 and using the fact that mass per unit area is equal to density ρ multiplied by thickness *t* yields:

$$I(t) = I_0 \exp(-\mu\rho t), \tag{3.2}$$

where I_0 is the initial intensity of the beam. The quantity $\mu\rho$ is also known as the linear absorption coefficient. Typically, tables of these values can be found in any X-ray reference text such as Cullity & Stock [29].

The general idea behind the scattering of X-rays consists of the observation that most photons are scattered in all directions by the presence of electric charge, but with amplitude depending on direction. In the classical conception of an unpolarized source, sufficient for this discussion, X-rays accelerate charged particles such as electrons, these moving charges then producing radiation of their own in all directions. The practical result is that some X-rays lose energy in the process, known as incoherent or Compton scattering, while the remainder may change direction but do not lose energy, which are the X-rays of interest [31]. The classically-derived Thomson formula for unpolarized X-rays gives the total (elastic and inelastic) X-ray scattering from a free electron:

$$I_e = r_e^{\,2} I_0 \frac{1+\cos^2(2\theta)}{2}, \tag{3.3}$$

where I_e is the energy scattered per unit solid angle per second, I_0 is the power of the incident beam of X-rays, 2θ is the angle of scattering, and r_e is known as the classical radius of the electron, defined as:

$$r_e = \frac{\mu_0 e^2}{4 m_e \pi}, \tag{3.4}$$

where μ_0 is the permeability of free space, 1.257×10^{-6} N·A^{-2}, e is the charge of an electron, 1.602×10^{-19} C, and m_e is the mass of an electron, 9.11×10^{-31} kg. Since the scattered intensity of X-rays is inversely dependent on the square of mass, the contribution from protons, some 1836 times more massive but with the same amount of charge, is neglected.

Interference between scattered X-rays causes variation in the detected intensity beyond the Thomson formula. Otherwise, SAXS, observing at small scattering angle, would show a practically unchanging function of intensity. Therefore, it is useful to derive an expression for the phase difference between X-rays in terms of a position vector (typically measured from the centre of an atom or some other suitable origin) and either the wave vector or scattering angle, all quantities that are easy to work with. The primary method of doing this is to construct a simple diagram showing the concurrent scattering of two X-rays from different targets [32]. In Figure 3.1, a monochromatic, parallel beam of X-rays of wavelength λ and direction $\boldsymbol{K_0}$ is incident upon two identical scattering targets, A and B, and scatters off both with angle 2θ, traveling in a new direction $\boldsymbol{K}$. Taking $\boldsymbol{r}$ as the vector from A to B, the path length difference δ can be written as:

$$\delta = (d_1 + d_2) = (\vec{r} \cdot \hat{K}_0 + -\vec{r} \cdot \hat{K}) = -\vec{r} \cdot (\hat{K} - \hat{K}_0). \quad (3.5)$$

Since the phase difference φ of a wave is defined as:

$$\varphi = 2\pi \frac{\delta}{\lambda}, \quad (3.6)$$

the difference in phase between the X-ray scattering from A and that from B is equal to:

$$\varphi = -\frac{2\pi}{\lambda} \vec{r} \cdot (\hat{K} - \hat{K}_0). \quad (3.7)$$

It is convenient to separate the position vector from the rest of the equation and define the scattering vector ***q*** as follows:

$$\vec{q} = \frac{2\pi}{\lambda} (\hat{K} - \hat{K}_0) = (\Delta \vec{k}), \quad (3.8)$$

where $\Delta \boldsymbol{k}$ is the change in the X-ray wave vector from incident to scattered. The magnitude of ***q*** can be easily determined by drawing the incident and scattered rays as well as ***q*** itself and using simple trigonometry. It is equal to:

$$|\vec{q}| = 4\pi \frac{\sin(\theta)}{\lambda}, \quad (3.9)$$

where the argument of the sine function is only half the scattering angle.

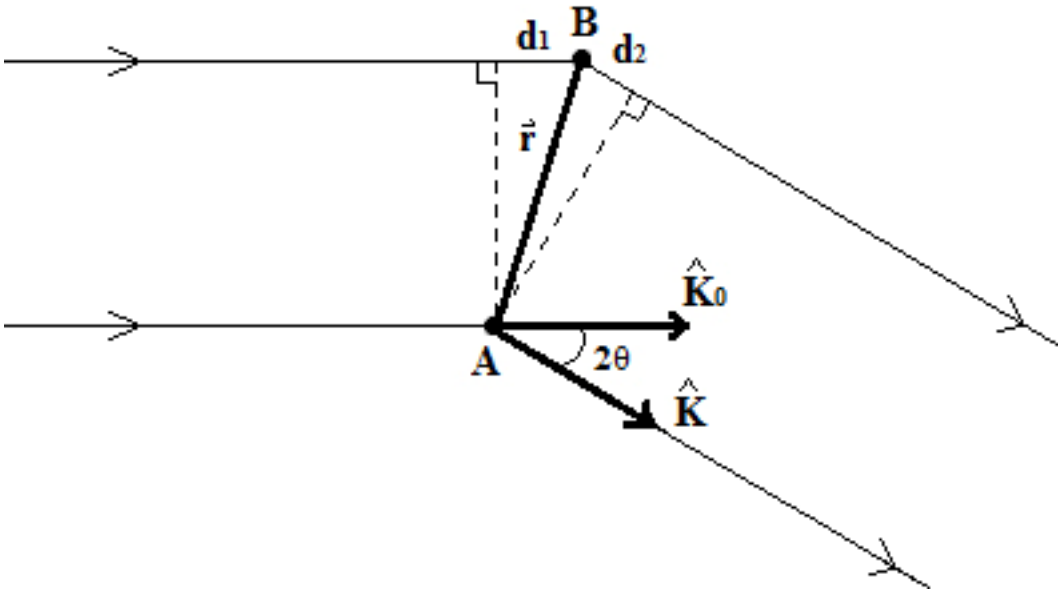

Figure 3.1 A diagram of two scatterers, A and B, along with the paths of X-rays scattering off these targets, the angle between the incident and scattered directions, and the path length differences between the two beams. Dashed lines are normal to X-ray paths.

An important classical question in optics was finding the amplitude resulting from the interference of n scattered waves, each with some amplitude A and phase φ. Here the scattering factor f can be introduced, defined simply as the ratio between the incident and scattered amplitude of an X-ray, i.e, $A = f \cdot A_0$. The solution to the interference problem is to treat phases as geometric angles, amplitudes as moduli and then find the resultant sum of the waves.

This can be written concisely in complex notation:

$$A = A_0 \sum_{j=0}^{n} f_j e^{i\varphi_j}, \tag{3.10}$$

Equation 3.10 can then be combined with the prior description of the phase of a scattered X-ray:

$$\varphi = -\frac{2\pi}{\lambda} \vec{r} \cdot (\hat{K} - \hat{K}_0) = -\vec{r} \cdot \vec{q} = -\vec{q} \cdot \vec{r}, \tag{3.11}$$

to give a general description of the resultant amplitude from scattering of X-rays by *n* discrete pieces of charge:

$$A(q) = \sum_{j=1}^{n} f_j \exp(-i\vec{q} \cdot \vec{r}_j), \tag{3.12}$$

where the scattering factors f_j are more precisely defined in terms of the equivalent number of independent electrons located at $\boldsymbol{r}_j$. At $q = 0$, the amplitude from each discrete charge is f_j times larger than if that charge was replaced by a single free electron, the amplitude of which being derived in the process of gaining Equation 3.3. Equation 3.12 is also known as the structure factor or *S(q)*. In WAXS, these scattering factors f_j are known as the atomic form factors [33], and are a function of both number of electrons and scattering vector *q*, as illustrated by the commonly used approximation:

$$f(q)_{WAXS} = \sum_{i=1}^{4} a_i \exp\left(-b_i\left(\frac{q}{4\pi}\right)^2\right) + c, \tag{3.13}$$

where all constants a_i, b_i, and c vary from atom to atom. Typically, these values are calculated using relativistic Hartree–Fock or Dirac–Slater wavefunctions to determine the shape and extent of the "electronic clouds" of a particular atom [34]. Figure 3.2 shows a set of atomic form factors given with respect to q and approximated using Equation 3.13. While the total scattering amplitude from a given atom is given by the number of electrons multiplied by the amplitude from a single free electron, this is divided into incoherent or Compton scattering as well as the elastic sort. Since elastic scattering is proportional to f^2, incoherent scattering must then be proportional to $(1\text{-}f)^2$ [31]. Given that f decreases as scattering angle increases, this means that less and less elastic scattering is observed at higher scattering angles to allow for more and more incoherent scattering. This explains why as scattering angle increases, the WAXS peaks of a material invariably decrease in intensity, which is related to amplitude by:

$$I(q) = \left|A(q)\right|^2. \tag{3.14}$$

As shown in Figure 3.2, at the low scattering angle regime of SAXS (generally, under $q <$ 0.7 Å^{-1}, or for Cu-Kα X-rays, $2\theta < 10°$), f is practically constant and equal to the scattering from the number of electrons in the atom, and so incoherent scattering can be safely ignored.

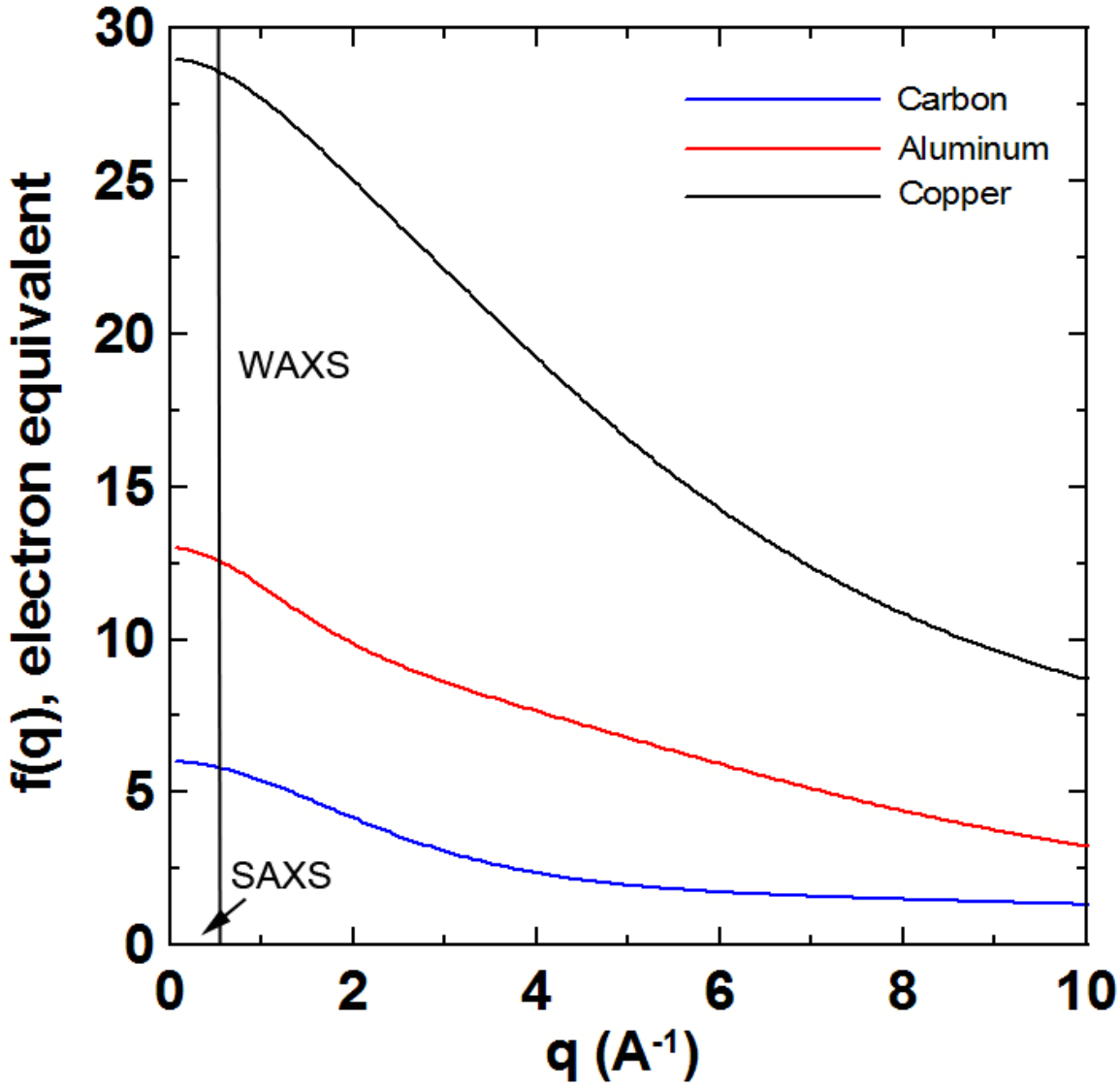

Figure 3.2 The atomic form factors of selected atoms, calculated from Equation 3.13 and using the data found in Table A.1, in Appendix 1. The typical angular region of SAXS is marked for reference.

The more complicated SAXS analogue of the WAXS atomic form factor, Equation 3.13, is in a form similar to the structure factor, but since the form factor of a particular object with continuous charges is now being described, the electron density $\rho(\boldsymbol{r})$ is used in place of form factors, and the summation of discrete charges is replaced by an integral over the

real-space volume of concern V (typically, where the electron density is non-zero or differs from the mean):

$$f(q)_{SAXS} = \int_V \rho(\vec{r}) e^{-i\mathbf{q}\cdot\mathbf{r}} dv_r . \tag{3.15}$$

This is nothing more than the Fourier transform of the electron density, going from real space (position vector $\boldsymbol{r}$ and volume element $\boldsymbol{dv_r}$) to reciprocal space (scattering vector $\boldsymbol{q}$).

Equation 3.12, the structure factor, takes into account the relative locations of atoms in a repeating crystal in WAXS, there represented by the atomic form factors f_j, to determine interference and the resulting amplitude. However, the typical procedure in SAXS is slightly different, as in general crystals and other structures with long range order are not being observed. As long as the sample objects are "dilute", with average separation distance being much larger than the X-ray wavelength used, the structure factor and thus total amplitude becomes simply the summation of the SAXS scattering factors $\boldsymbol{f(q)_j}$ of each object, calculated using Equation 3.15. This can be seen by modeling the SAXS structure factor, using Equations 3.12 and 3.14:

$$I(q) = \sum_{j=1}^{n} f(q)_j \exp(-i\vec{q}\cdot\vec{r}_j) \sum_{k=1}^{n} f^*(q)_k \exp(i\vec{q}\cdot\vec{r}_k), \tag{3.16}$$

which, assuming the system is isotropic or centrosymmetric, becomes:

$$I(q) = \sum_{j=1}^{n} \sum_{k=1}^{n} f(q)_j f(q)_k \cos(q \cdot (\vec{r}_j - \vec{r}_k)), \quad (3.17)$$

where $\boldsymbol{r}_j$ - $\boldsymbol{r}_k$ is simply the vector between the objects *j* and *k*. This can be simplified further by separating the terms with *j* = *k*:

$$I(q) = \sum_{j=1}^{n} f^2(q)_j + \sum_{j=1}^{n} \sum_{j \neq k} f(q)_j f(q)_k \cos(q \cdot (\vec{r}_j - \vec{r}_k)). \quad (3.18)$$

This can be interpreted as the sum of the intensities from scatterers plus an interference term from interactions between scattering objects. Since for large *n*, an isotropic distribution of scatterers, and a large distance between particles *j* and *k* compared to the X-ray wavelength, the cosine terms should on average cancel out, Equation 3.18 thus shows that "dilute" systems with these characteristics in SAXS can be described in terms of the form factor alone. In mathematical terms, for a set of *n* identical particles, $A(q) = nf(q)$ and $I(q) = (nf(q))^2$. However, this is not always a good assumption, especially with high concentrations of scattering objects in solution, which is difficult to compensate for theoretically. Typically, information would be gathered at low concentration to determine the form factor of a particle, and separate samples at high concentration would be examined to construct a structure factor for the same particle [32].

For dilute systems, where the amplitude is directly proportional to the form factor, a knowledge of the amplitude could yield the electron density since the Fourier transform in Equation 3.15 is reversible:

$$\rho(\vec{r}) = \left(\frac{1}{2\pi}\right)^3 \int_V A(q) e^{i\mathbf{q}\cdot\mathbf{r}} dv_{\mathbf{q}}. \tag{3.19}$$

Unfortunately, the amplitude cannot be directly measured, only the intensity! This means that SAXS is not quite like an "X-ray microscope", but instead is a tool that observes a complicated function of the electron density of some object of interest. As SAXS deals with larger structures than WAXS, SAXS modeling often then becomes, in essence, an exercise in accurately describing the form factors of randomly oriented, widely dispersed, structured collections of atoms. This also means that without a form factor or other model of the target object, SAXS is extremely difficult to use. Other tools such as scanning electron microscopy can be enlisted in confirming the physical form (sphere, cylinder, etc) of a given structure in order to aid in a model's construction [31].

One important consideration in X-ray scattering is that small objects give scattering intensity at large angles, and large objects scatter at small angles. This can be seen from the Bragg equation of X-ray diffraction from parallel planes of a regular crystal lattice:

$$\sin(\theta) = \frac{n\lambda}{2d_{hkl}}, \tag{3.20}$$

where θ is the angle between the incident X-ray beam and scattering planes, n is an integer, λ is the X-ray wavelength, and d_{hkl} is the spacing between the crystal planes. While the Bragg equation is not directly applicable to SAXS, it can be used to estimate the angle at which particles of a given size will show scattering intensity.

3.3 MODELING OBJECTS AND THE AUTOCORRELATION FUNCTION

Before going into more depth and deriving the general form of the equation used in SAXS modeling, as well as "going backwards" and using the scattering intensity to determine useful information about a sample (instead of using models to predict intensity), the simplest model of the target object will be examined: a monodisperse, dilute, identical set of N hard spheres of radius R and constant electron density ρ inhabiting a void. Under these conditions, the scattering amplitude (and intensity) can be determined exactly, being simply proportional to the form factor of a sphere:

$$A(q) = Nf(q)_{Sphere}. \tag{3.21}$$

Equation 3.16 can be used directly by integrating in spherical co-ordinates over the sphere, with vectors $\boldsymbol{q}$ and $\boldsymbol{r}$ separated by angle θ:

$$f(q) = \iiint_V \rho \exp[-iqr\cos(\theta)]r^2 \sin(\theta) dr d\theta d\varphi. \tag{3.22}$$

This expression can be progressively simplified:

$$f(q) = 2\pi\rho \int_{r=0}^{R} 2r^2 \frac{\sin(qr)}{qr} dr, \tag{3.23}$$

$$f(q) = 4\pi\rho\left(\frac{\sin(qR) - qR\cos(qR)}{q^3}\right), \tag{3.24}$$

and, given in terms of the volume of a sphere,

$$f(q) = 3V\rho\left(\frac{\sin(qR) - qR\cos(qR)}{(qR)^3}\right). \tag{3.25}$$

The intensity is then the square of the amplitude (shown for N spheres):

$$I(q)_{Sphere} = (3V\rho N)^2\left(\frac{\sin(qR) - qR\cos(qR)}{(qR)^3}\right)^2. \tag{3.26}$$

This expression, first derived by Rayleigh in 1911 [35], is plotted in Figure 3.3. SAXS graphs are typically given in log *I(q)* vs log *q* form to make features of the data more visible. As can be seen, increasing the number of spheres simply makes intensity at all angles rise, while changing the radius of the spheres changes the intensity pattern, shifting the scattering "hills" to smaller angles. This shows that larger objects show scattering intensity at smaller angles.

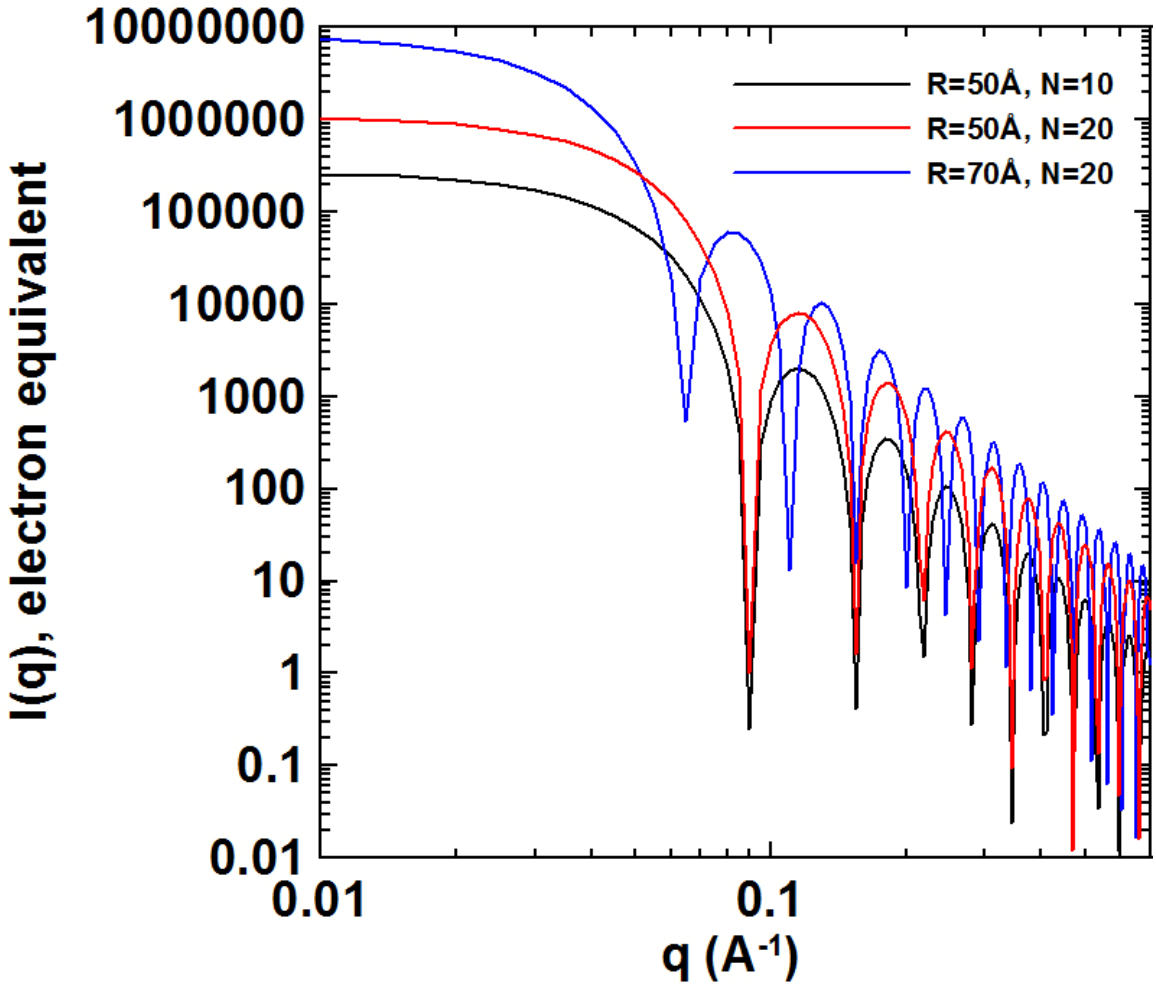

Figure 3.3 An illustration of the scattering intensity from three sets of widely separated hard spheres, each with electron density of 10^{-4} $e^-/Å^3$. Intensity is given in electron scattering equivalent units, and calculated intensity is shown from q = 0.01 to 0.7 $Å^{-1}$ (scattering angle of 0.14 to 10° for Cu-Kα wavelength).

The sharp intensity extinction points in Figure 3.3, where $tan(qR) = qR$ and $f(q)$ becomes zero, are eliminated when a polydisperse collection of spheres is considered. In Figure 3.4 the effect of using a normal distribution of hard spheres instead of a single radius becomes apparent, as the "hills" and "valleys" quickly become damped as the standard deviation increases. Also noticeable is the fact that the intensity tends to decline linearly

on the log-log graph, or exponentially on a linear graph: this is a wide-ranging result known as Porod's law [36], which states for sufficiently high q, SAXS intensity will change proportional to q^{-4}. Ignoring the oscillations (behaviour particular to spheres), this can be derived by taking the limit of Equation 3.26 ($N = 1$) as qR gets very large:

$$qR >> 1 \Rightarrow \left(\frac{\sin(qR) - qR\cos(qR)}{(qR)^3} \right)^2 \cong \left(\frac{-\cos(qR)}{(qR)^2} \right)^2 \cong (qR)^{-4}, \tag{3.27}$$

$$I(q)_{Sphere} \cong (9\rho^2) \times \left(\frac{16}{9}\pi^2 R^6 \right) \times (qR)^{-4} = \frac{4\pi\rho^2(4\pi R^2)}{q^4} = \frac{4\pi\rho^2 S}{q^4}, \tag{3.28}$$

where S is the surface area of the hard spheres and ρ is in general the electron density contrast between the particle and its surroundings. Porod's law holds for many systems studied under SAXS and can be also derived from more general SAXS equations.

While Equation 3.26 gives the intensity from a collection of dilute hard spheres of radius R, there are many materials that exhibit polydispersity and close-packing behaviour while having the form factor of hard spheres, and thus a structure factor and size distribution function must be taken into account with the model. This process can quickly become computationally difficult! Various specialized software exists which aims to ameliorate this situation. Unfortunately, numerical calculations are a necessity at this level of detail and no closed form equations are possible.

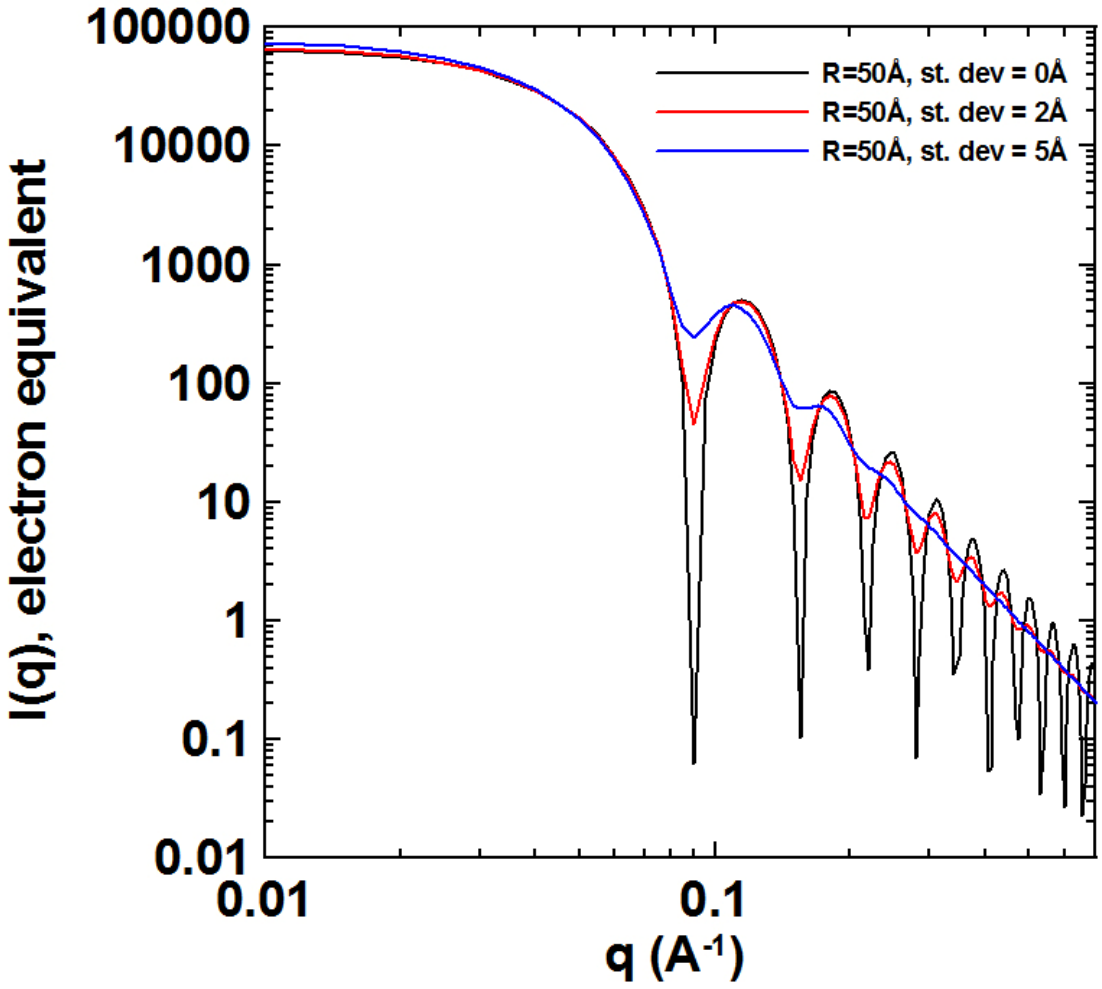

Figure 3.4 The scattering intensity from three sets of widely separated hard spheres, with radius distributed normally (standard deviation varying by set) and with electron density of 10^{-4} $e^-/Å^3$. Intensity is given in electron scattering equivalent units, and calculated intensity is shown from q = 0.01 to 0.7 $Å^{-1}$ (scattering angle of 0.14 to 10° for Cu-Kα wavelength).

A similar approach to that of the hard sphere may be made with ellipsoids, cylinders, core-shell particles, etc [35], but there are many situations and objects where Equation 3.15 is not directly calculable without the aid of numerical procedures and modeling must take a different, more indirect approach. To attack these problems, another technique is

used: the concept of the autocorrelation function. Assuming dilute particles for simplicity, and starting from the equation for scattering intensity:

$$I(q) = \left|A(q)\right|^2 = A^*(q)A(q), \tag{3.29}$$

the scattering amplitudes can be replaced by integral formulations reminiscent of Equation 3.15, since for dilute particles *A(q)* is just the summation of all *f(q)*:

$$I(q) = \int_V \rho(\mathbf{u}) e^{i\mathbf{q}\cdot\mathbf{u}} dv_u \int_V \rho(\mathbf{u}') e^{-i\mathbf{q}\cdot\mathbf{u}'} dv_{u'}, \tag{3.30}$$

where the position vectors ***u*** and ***u′*** are used for convenience. This can be rewritten by taking both integrals together and merging the exponential terms:

$$I(q) = \iint \rho(\mathbf{u})\rho(\mathbf{u}') e^{-i\mathbf{q}\cdot(\mathbf{u}'-\mathbf{u})} dv_u dv_{u'}. \tag{3.31}$$

In WAXS a similar approach applies, except with the integrals substituted by summations and the electron densities by atomic scattering factors, which leads to the diffraction conditions that determine at which angles a crystal will scatter X-rays that then interfere constructively. In SAXS, defining the position vector ***r* = *u′* - *u***, Equation 3.31 can be rewritten:

$$I(q) = \iint \rho(\mathbf{u})\rho(\mathbf{u}+\mathbf{r}) e^{-i\mathbf{q}\cdot\mathbf{r}} dv_{\mathbf{r}} dv_{\mathbf{u}} = \int_V \wp(\mathbf{r}) e^{-i\mathbf{q}\cdot\mathbf{r}} dv_{\mathbf{r}}, \tag{3.32}$$

where the autocorrelation function of the electron density, $\wp(\boldsymbol{r})$, is defined as:

$$\wp(\mathbf{r}) = \int_V \rho(\mathbf{u})\rho(\mathbf{u}+\mathbf{r})dv_u. \tag{3.33}$$

This function is what the intensity from a SAXS experiment can describe directly, through the inverse Fourier transform. The autocorrelation function is a complicated function of the distribution of matter in an object, which is difficult to interpret directly. Hence it is necessary to make some hypotheses about electron density to get useful models. To clarify a previous description, SAXS is indeed not an "X-ray microscope", but it is an "autocorrelation X-ray microscope". Inside the volume of interest, one description of the autocorrelation function is that the ratio of $\wp(\boldsymbol{r})$ to volume is the average value of the product of the electronic densities at two points separated by the vector $\boldsymbol{r}$ [31]. One common companion to any discussion of $\wp(\boldsymbol{r})$ is reproduced in Figure 3.5. A particle and its "ghost", a replica translated by $\boldsymbol{r}$, have in common a volume V. If the region outside of the particle has zero electron density, then V represents the region of the particle that contributes to $\wp(\boldsymbol{r})$.

Because of the difficulty in using the autocorrelation function and deriving useful models in SAXS, two assumptions previously mentioned in discussion of the structure factor are commonly made and apply well to most objects of study. The first is that the system of particles studied is statistically isotropic, which means the phase factor in Equation 3.32 can be replaced with its average over all directions:

$$\left\langle e^{-i\mathbf{q}\cdot\mathbf{r}} \right\rangle = \frac{\sin(qr)}{qr}, \tag{3.34}$$

leading Equation 3.32 to be reformulated in spherical coordinates as:

$$I(q) = \int_{r=0}^{\infty} 4\pi r^2 \wp(r) \frac{\sin(qr)}{qr} dr. \tag{3.35}$$

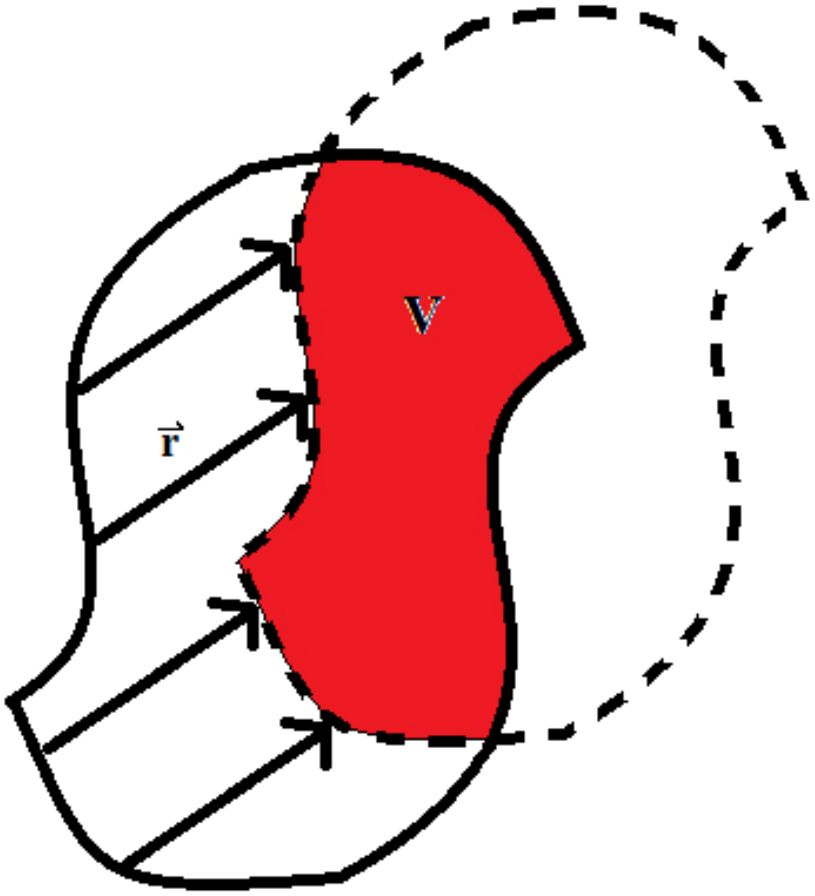

Figure 3.5 A particle of constant electron density and its "ghost", created by shifting the particle by an arbitrary vector ***r***. The volume *V* that both figures have in common is shaded for visibility. The region of space outside of the particle is assumed to be void.

The second assumption is that there exists no long range order in the system of particles, implying that there is no electronic correlation between two points separated widely enough. Of course, this is not in conflict with the possibility of a high concentrations of objects in the system, with models possibly needing a structure factor, but it does mean that in modeling a particle, at large *r* the electron density can be assumed to tend toward some average. We can then return to the analysis of the autocorrelation function to deal with situations where there are objects of interest embedded in some medium with the entire system having average electron density ρ_{av}. At large distances, the autocorrelation function will become its minimum:

$$\wp(\mathbf{r}) = \int_V \rho(\mathbf{u})\rho(\mathbf{u}+\mathbf{r})dv_u = \int_V \rho(\mathbf{u})\rho_{av}dv_u = \rho_{av}\int_V \rho(\mathbf{u})dv_u = V{\rho_{av}}^2, \tag{3.36}$$

while for $\boldsymbol{r} = 0$, the autocorrelation function yields its maximum:

$$\wp(\mathbf{r}) = \int_V \rho(\mathbf{u})\rho(\mathbf{u}+0)dv_u = \int_V \rho^2(\mathbf{u})dv_u = V{\rho^2}_{av}, \tag{3.37}$$

where the last constant is the average of the squared electron density (as opposed to the square of the average electron density). Since the Fourier transform of a constant is the Dirac delta function $\delta(r)$, which is zero everywhere save for at $r = 0$, from Equation 3.35 the scattering intensity resulting from a constant autocorrelation function is zero everywhere but at $q = 0$, which is unattainable experimentally. This means that only fluctuations in electron density give rise to scattering intensity! It is therefore convenient

to neglect the scattering background and focus on the deviations from the average of electron density, i.e, the region of particles where the correlation function is variable. Instead of using electron density in the definition of the autocorrelation function, the electron density fluctuation $\eta = \rho - \rho_{av}$ can be inserted instead:

$$\xi(\mathbf{r}) = \int_V \eta(\mathbf{u})\eta(\mathbf{u}+\mathbf{r})dv_u, \langle \xi(\mathbf{r}) \rangle = \langle \wp(\mathbf{r}) \rangle - V\rho_{av}{}^2 = V\gamma(r), \tag{3.38}$$

which introduces the correlation function $\gamma(r)$ [35]. This can be thought of as the average of the product of two electron density fluctuations separated by a distance r (since isotropy is assumed, we use the magnitude of the vector):

$$\gamma(r) = \langle \eta(\mathbf{u})\eta(\mathbf{u}+\mathbf{r}) \rangle, \tag{3.39}$$

with the properties that $\gamma(0) = \eta^2_{av}$, and $\gamma(r) = 0$ for large enough r. Returning to Equation 3.35 with this correlation function:

$$I(q) = V \int_{r=0}^{\infty} 4\pi r^2 \gamma(r) \frac{\sin(qr)}{qr} dr, \tag{3.40}$$

which is the most general form for SAXS intensity in a system that is isotropic and has no long range order. The inverse Fourier transform is of importance as well, yielding the correlation function:

$$V\gamma(r) = \frac{1}{2\pi^2} \int_{q=0}^{\infty} q^2 I(q) \frac{\sin(qr)}{qr} dq, \tag{3.41}$$

which has a special significance at $r = 0$:

$$V\gamma(0) = V\overline{\eta^2} = \frac{1}{2\pi^2} \int_{q=0}^{\infty} q^2 I(q) dq = \frac{1}{2\pi^2} Q, \tag{3.42}$$

where Q is the "invariant", which is directly related to the mean square of electron density fluctuations, a property that can remain constant while other aspects of the material do not [35].

3.4 THE KALLIAT MODEL AND EXTENSIONS

With Equation 3.40 more complex models of SAXS can be examined. Debye found that for a two-phase system with a random distribution of void and solid, modeling the probabilities of a hypothetical rod thrown at random within the material having ends in one or the other phase yielded a correlation function of [37]:

$$\gamma(\mathrm{r}) = \eta^2{}_{av} \cdot \mathrm{e}^{-r/a}, \tag{3.43}$$

where a is defined as:

$$a = 4(\varphi - \varphi^2)\frac{V}{S}; \tag{3.44}$$

η^2_{av} is the average squared fluctuation from mean electron density, φ is the fraction of void in the material, and *V/S* the volume to surface area ratio of the material. When Equation 3.43 is placed into Equation 3.40, the integration can be performed and the result is:

$$I(q) = \frac{8\pi a^3 \overline{\eta^2} V}{(1 + q^2 a^2)^2}. \tag{3.45}$$

The constant *a* is also called the Debye autocorrelation length, and can be related to the radius of gyration (R_g), a measure of the average feature size that is the electronic analogue to the radius of inertia of an object [32]:

$$R_g = \sqrt{6}a. \tag{3.46}$$

Here, Babinet's principle may be discussed. In SAXS, the scattering intensity depends on the square of the electron density fluctuations, not the value itself. Since a negative number squared is positive, this means that a random system of voids in a support medium of electron density ρ will scatter identically to a system of particles of electron density ρ randomly distributed in a void. It is the contrast that matters, not the absolute value.

Kalliat *et al.* further developed Debye's description of the two-phase system by applying it to coal-based carbons [4]. Many activated carbon materials have different classes of pores: micropores (≤ 20 Å in width), mesopores (20-500 Å in width) and macropores (≥ 500 Å in width) [13]. The idea that Kalliat put forward was to treat the carbon as a set of multiple two-phase systems that can each be described by some variation of the Debye term of Equation 3.45 combined with Porod's Law. The end result is a versatile model of scattering intensity that has described many porous materials such as pyrolized sugars, coals, carbide-derived carbons and activated carbons [38-43]. For a theoretical carbon with micropores, mesopores and macropores, one simple variation of the Kalliat model is:

$$I(q) = \frac{A}{q^n} + \frac{B}{\left(1 + a^2 q^2\right)^2} + \frac{C_{mi}}{\left(1 + b^2 q^2\right)^2}, \tag{3.47}$$

where the first term represents the macropores, the second the mesopores, and the third the micropores. A is proportional to the surface area of macropores, B and C_{mi} are proportional to the volume of mesopores and micropores respectively, a and b are the Debye autocorrelation lengths for their respective pore classes, and finally n is a fitting constant that is related to the fractal dimension of the carbon surface [44, 45]. Porod's law holds for perfectly smooth macropores, with a value of $n = 4$, but values of $3 < n < 4$ are indicative of scattering from rough, fractal-like surfaces. A constant D can be added to Equation 3.47 to account for scattering background if necessary.

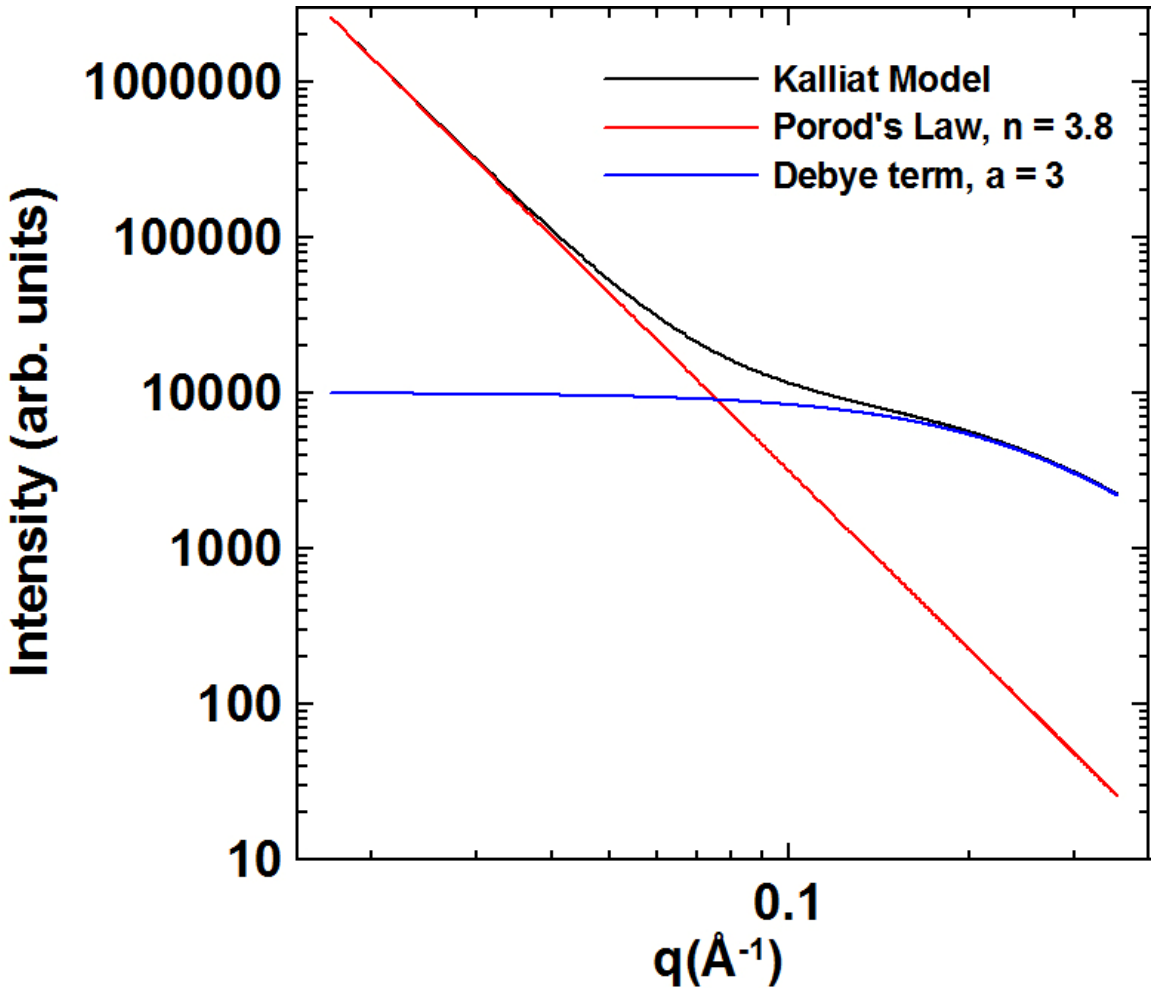

Figure 3.6 A calculation of the Kalliat model intensity for a porous carbon with both micropores and macropores. *A* and *B* values are set for the visibility of each contribution to total intensity at 0.5 and 10000 respectively. Data is shown over a scattering range of q = 0.015 - 0.356 $Å^{-1}$ (scattering angle of 0.23 º - 5.00º).

Figure 3.6 shows a theoretical calculation of a carbon with just macropores and micropores, while Figure 3.7 gives a real example of SAXS data of Kuraray GC, a carbon that fits this profile well. Immediately it is apparent that the fit is not perfect: the fit and data diverge somewhat at very low q and near the "hump" at around 0.1 $Å^{-1}$. The former is due in this case to experimental error, specifically the beam-stop of the Bruker-AXS

nanoSTAR SAXS instrument blocking some small-angle radiation from reaching the detector and causing the low-angle data to appear to curve inward. The latter can be traced back to the discussion of the structure factor and Equation 3.18. In essence, Kuraray GC is a highly microporous carbon and it has been suggested that either pores or small planar aggregates [4] interfere with each other. The Kalliat model assumes dilute particles (or in this case, voids). When this assumption becomes less suitable, without a structure factor the model is unable to compensate and fitting error occurs. However, this error is relatively small and does not remove the significance of fitting, as will be discussed in Chapter 4.

Fitting experimental activated carbon data using some variation of Equation 3.47 allows for only an "average" pore dimension to be determined as per the nature of the two-phase model correlation function. Since activated carbons have a variety of pore sizes, it is worth modeling the effects of distributions of pores on this model. To that end, calculations can be performed to determine the difference between SAXS curves constructed using an average pore dimension and those calculated using a distribution of pore sizes.

One approach is to use a Kalliat pore term in the calculations with an average pore dimension, while utilizing Gaussian and Weibull probability distribution functions to generate the range of pore sizes. These distributions have been used to help describe the physical adsorption of gases or vapours on microporous adsorbents. For example, the

Weibull and Gaussian distributions have been used in the development and explanation of the Dubinin-Radushkevich and Dubinin-Astakhov equations [45, 46].

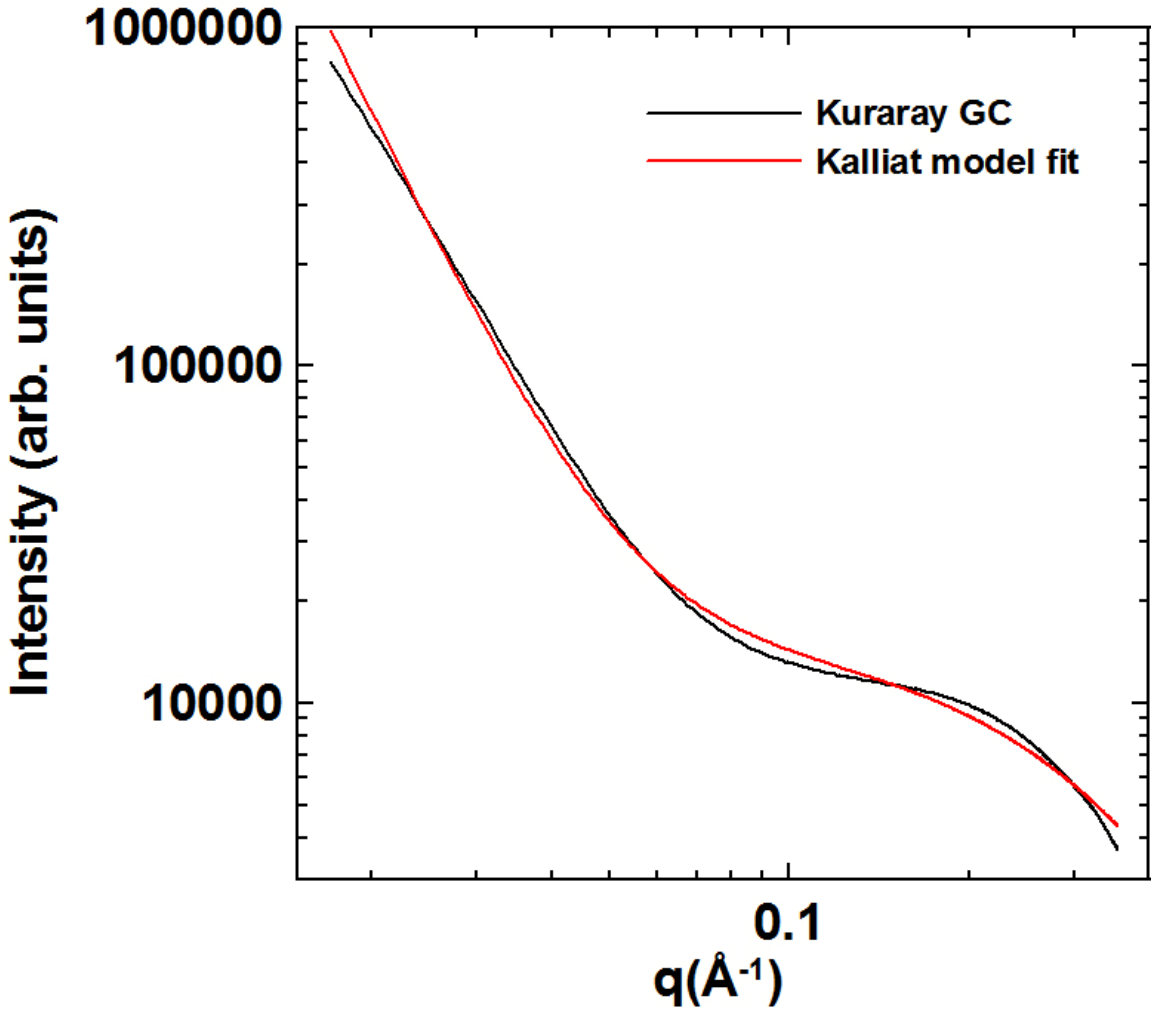

Figure 3.7 SAXS data obtained from unimpregnated Kuraray GC carbon, together with a fit using Equation 3.47. Data is shown over a scattering range of q = 0.015 - 0.356 Å^{-1} (scattering angle of 0.23 º - 5.00º).

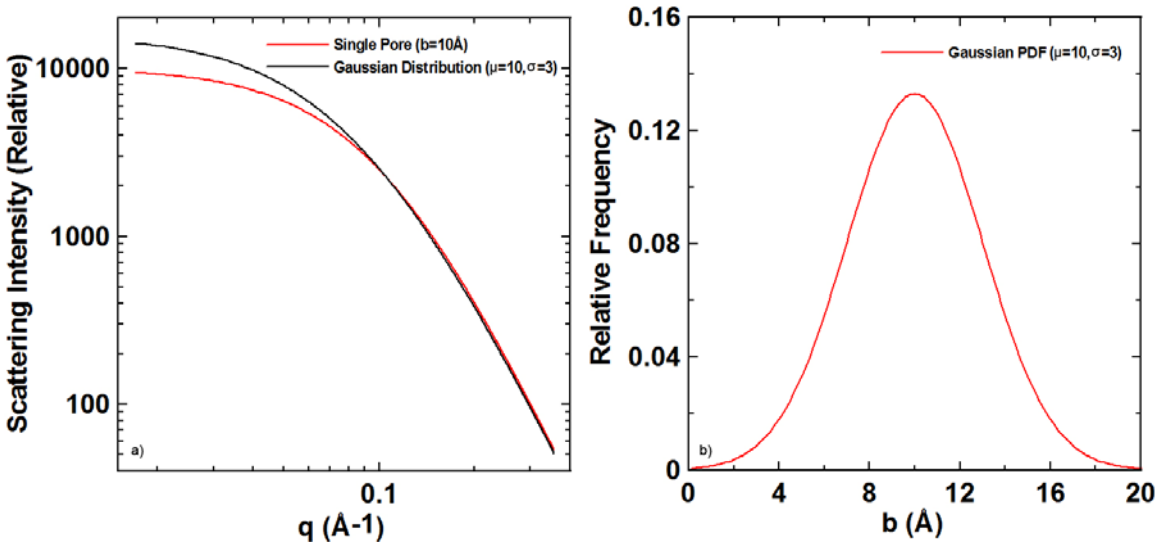

Figure 3.8 a) The Kalliat pore term modeled for a monodisperse system of b = 10 Å pores and for a set of pores weighted by a Gaussian probability density function (PDF) with mean 10 Å and standard deviation 3 Å. b) The Gaussian PDF used to model the Kalliat term for the set of pores in a).

The equation used to perform the Gaussian-weighted calculations is given by:

$$I_G = \frac{1}{\sigma\sqrt{2\pi}} \int_0^\infty \frac{b^4}{\left(1+b^2q^2\right)^2} \times \exp\left(\frac{-1}{2}\left[\frac{b-\mu}{\sigma}\right]^2\right) db, \tag{3.48}$$

where σ is the standard deviation and μ is the mean. The equation used to perform the Weibull-weighted calculations is given by:

$$I_W = \int_0^\infty \frac{b^4}{\left(1+b^2q^2\right)^2} \times \frac{k}{\alpha} \times \left(\frac{b}{\alpha}\right)^{k-1} \times \exp\left(-\left(\frac{b}{\alpha}\right)^k\right) db, \tag{3.49}$$

where k is the shape parameter and α is the scale parameter. These calculations can be done on any desktop computer with commercially available software such as Mathematica or Maple.

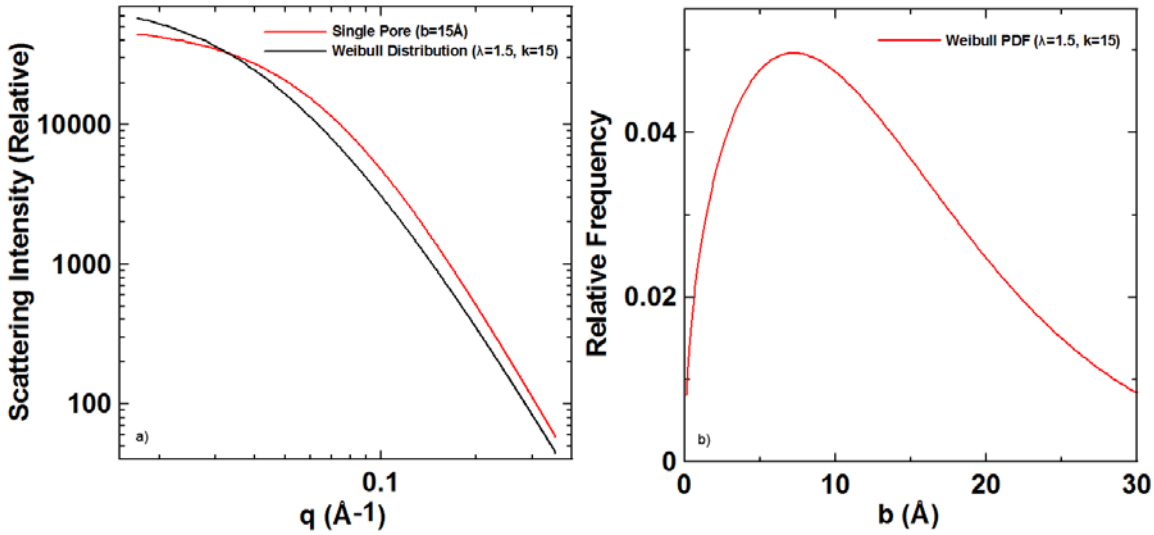

Figure 3.9 a) The Kalliat pore term modeled for a monodisperse system of b = 15 Å pores and for a set of pores weighted by a Weibull PDF with scale parameter 1.5 Å and shape parameter 15 Å. b) The Weibull PDF used to model the Kalliat term for the set of pores in a).

Figure 3.8 a) shows that there is little difference between the scattering intensity contributions of the Kalliat term with b = 10 Å and the distribution of pores with μ = 10 Å. The $q > 0.1$ Å^{-1} "tail" is nearly identical for both curves, with only slight differences between the models in the $q < 0.1$ Å^{-1} region. Figure 3.8 b) shows the calculated Gaussian distribution. Figure 3.9 a) shows a Weibull distribution with scale parameter 1.5 Å and shape parameter 15 Å. The Kalliat pore term with b = 15Å is also shown. There is a constant but small difference between the calculated curves for all regions of q. The

calculated data in Figures 3.8 a) and 3.9 a) suggest that the modified Kalliat model is effective at fitting scattering intensities as long as each distinct group of pore or particle sizes is taken into account with a representative Debye autocorrelation parameter and an associated term in the model. For example, Kuraray GC requires only one pore size term to describe micropore scattering and a Porod (A/q^n) term to describe scattering from large meso- and macropores.

Before going into more depth with the Kalliat model, Equation 3.47 should be updated to include the absolute calibration of an instrument as well as the electron density contrast:

$$I(q) = \rho^2 I_{0K}\left[\frac{A}{q^n} + \frac{C_{mi}}{\left(1 + b^2 q^2\right)^2}\right], \tag{3.50}$$

where ρ is the electron density of graphite, I_{0K} is the Kalliat constant in $g \cdot W \cdot m^{-2}$, defined as:

$$I_{0K} = \frac{2\pi}{t} I_e \frac{M}{A_{sample}} A_{beam}, \tag{3.51}$$

where t is the transmission of the sample, I_e is the intensity scattered by a single electron, calculated from Equation 3.3, M is the sample mass in g, A_{sample} is the cross sectional area of the sample, A_{beam} is the area of the X-ray beam penetrating the sample, and as before, A is proportional to the surface area of large mesopores and macropores, while C_{mi} is proportional to the volume of micropores in the sample.

Kalliat *et al*. have shown [47] that the micropore volume for a given sample of activated carbon can be determined from C_{mi}, the constant associated with the micropore term, when scattering intensity is measured in absolute units. This requires the SAXS equipment to be absolutely calibrated. The procedure for getting the intensity in photons of the direct beam is detailed in Chapter 2. Using Equation 3.3, this number can be converted into I_e, the scattered intensity per electron, while converting solid angle into area using the sample to detector distance. The micropores can then be modeled as identical spheres with radius R_{sp}:

$$R_{sp} = \sqrt{\frac{5}{3}} R_g, \tag{3.52}$$

where R_g is the radius of gyration, given in terms of the Debye autocorrelation length in Equation 3.46. Assuming micropores scatter independently, then the fitting constant C_{mi} in units of cm^6/g can be related to micropore volume per unit mass in cm^3/g:

$$C_{mi} = \frac{1}{2\pi} V^0{}_{mi} \frac{\overline{V^2}}{\overline{V}}, \tag{3.53}$$

where the volume-average volume in cm^3 for identical spheres of radius R_{sp} , given in terms of the autocorrelation length b, is:

$$\frac{\overline{V^2}}{\overline{V}} = \frac{4\pi}{3} (10)^{\frac{3}{2}} b^3. \tag{3.54}$$

The micropore volume per unit mass of a given type of activated carbon can then be estimated using these relations.

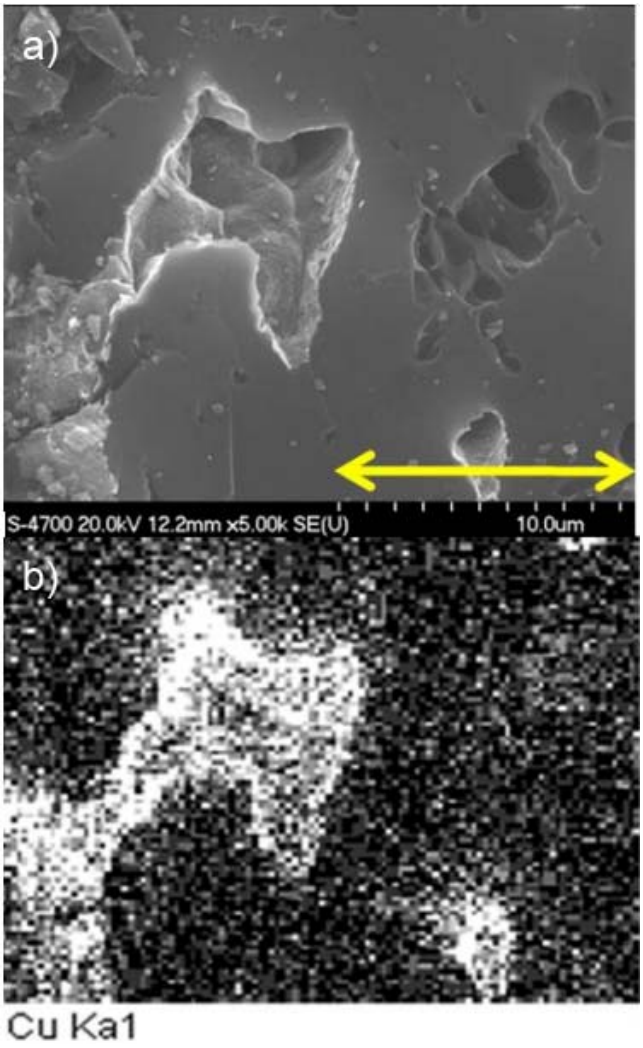

Figure 3.10 a) SEM imagery of the pore structure of a carbon sample impregnated by CuO. The copper impregnant is distributed well. b) An EDX pixel map of the area shown in a), where the white pixels represent areas where copper is present. Adapted from Figure 5.12 in reference [15].

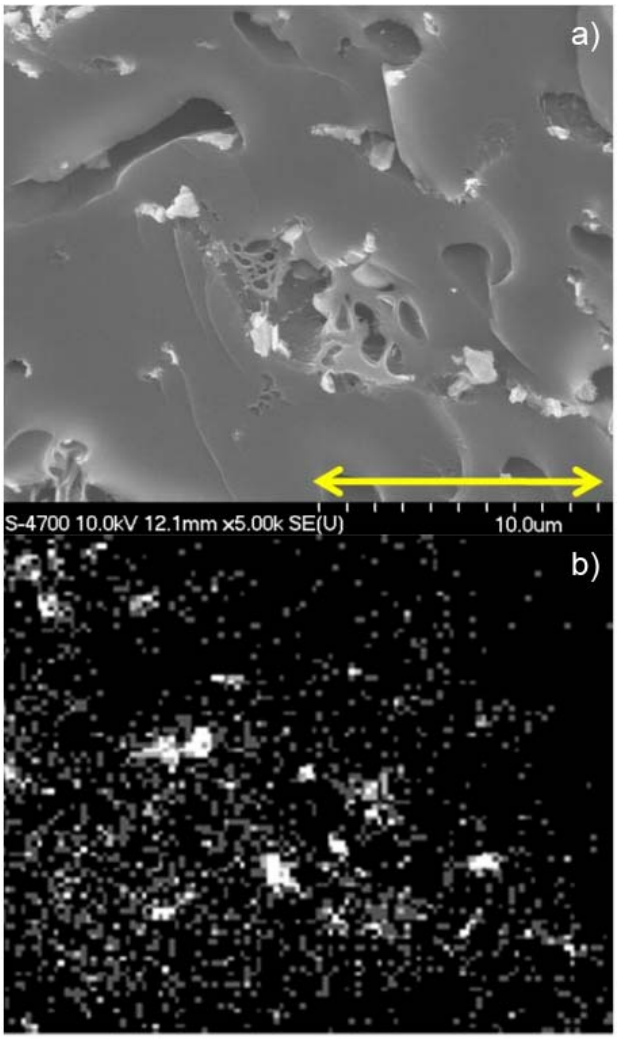

Figure 3.11 a) SEM imagery of the pore structure of a carbon sample impregnated by copper compounds. Large grains of material are visible. b) An EDX pixel map of the area shown in a), where the white pixels represent areas where copper is present. Adapted from Figure 7.2 in reference [15].

So far, discussion has been limited to "base" microporous carbon consisting of carbon and void, but activated carbons impregnated with various chemical species presents a new problem. Impregnated material can form grains of varying sizes in all classes of pores, from filling micropores to agglomerating on the surface of the larger mesopores

and macropores. This can be seen in SEM images. In Figure 3.10, CuO impregnant is distributed well in the pores, as evidenced by both the SEM and energy-dispersive X-ray spectroscopy (EDX) images, while in Figure 3.11, CuO is seen forming large grains of approximately a micron in size in large mesopores and macropores. Often the distribution and behaviour of this impregnant is important to determine [19, 20]. To handle this new situation a further modification of the Kalliat model is introduced:

$$I(q) = I_{0K}\left[\rho_{av}{}^{2}\frac{A}{q^{n}} + \frac{\rho_{x}{}^{2}B_{gr}}{\left(1+a^{2}q^{2}\right)^{2}}\right] + I_{0K'}\left[\left(\rho - x\rho_{x}\right)^{2}\frac{C_{mi}}{\left(1+b^{2}q^{2}\right)^{2}}\right], \tag{3.55}$$

where $\rho_{av}{}^{2}$ is the squared average electron density of large mesopores, macropores and large grains, found to a first approximation by weighting the impregnant and carbon electron densities by the mass fraction in the sample. I_{0K} is defined previously in Equation 3.51, $I_{0K'}$ is calculated similar to Equation 3.51 except the average mass of an unimpregnated sample is used, for the reason that the micropore structure is unchanged during impregnation. $\rho_{x}{}^{2}$ is the squared electron density of the impregnant, and x is the volume fraction of the impregnant in the micropore. The first term in the equation represents the contribution from large mesopores and macropores as in the unimpregnated model but with the addition of impregnant grains large enough to preclude exact characterization. The second term takes into account the intensity contribution from micrograins of the impregnant (typically ranging from 15 to 20 Å in width) and the third term corresponds to the scattering intensity from the micropores, which changes as the impregnant is embedded into the pores. Like C_{mi}, B_{gr} can be related

to the volume of the small impregnant grains by using Equations 3.53 and 3.54, while a is the Debye autocorrelation length of the small grains, with its own radius of gyration. Since macrograins (many nm in size) show up in the available range of data only as Porod tails or q^{-4} contributions to overall intensity [48], they qualitatively manifest as vertical scaling of the data in the low q range as chemical loading increases and macrograins continue to form, and quantitatively cause A to increase.

The system of grains, pores and carbon structure is a three phase system, but can be viewed as a set of three parallel quasi two-phase subsystems by extending the insight of Kalliat *et al*. If partially filled pores are treated as completely filled with the average electron density, then the separate two phase systems are the partially filled pores and carbon structure, the impregnant micrograins and void, and the macropores/macrograins and void (accounted for in the A/q^n term). Using a quasi two-phase approach to modeling a true three-phase system has been successfully implemented for platinum catalysts supported on porous carbon [49].

For an impregnated activated carbon, the total scattering intensity is the sum of contributions from both impregnant grains and carbon pores. A few assumptions are included:

a) Carbon micropores can be filled by impregnant but the underlying carbon structure is not shrunk, enlarged, or otherwise changed by the impregnation process.

b) In a micropore, the contrast in electron density in the quasi two-phase system can be described by:

$$\Delta\rho^2 = \left(x\rho_x - \rho\right)^2, \tag{3.56}$$

where ρ is the electron density of the carbon, ρ_x is the electron density of the impregnated species, and x is the volume fraction of impregnant in the micropore.

c) In the larger mesopores and macropores, impregnant particles tend to be much smaller than the pore and can be treated as independent grains in a vacuum in terms of their scattering contribution.

Relevant items to observe as impregnant loading increases in a carbon sample include A/q^n evaluated at a consistent value q, B_{gr} and C_{mi}, which can be used to determine the level of micropore filling and grain formation, and the more qualitative behaviour of intensities at low (< 0.04 $Å^{-1}$) and high (> 0.2 $Å^{-1}$) q values. Impregnant distribution tendencies can be effectively judged from this combined analysis.

In particular, since filling micropores with impregnant should decrease electron density contrast in a predictable way, the total amount of micropore filling and thus the fraction of impregnant going into micropores can be determined. Fitting C_{mi} from sample data after a volume of impregnant V_{xmi} has entered into the micropores of volume V^0_{mi} should yield:

$$C_{mi}' = C_{mi} \frac{\left(\frac{V_{xmi}}{V^{0}_{mi}} \rho_x - \rho \right)^2}{\rho^2}, \tag{3.57}$$

where C_{mi}' is the fitted constant of the impregnated sample, C_{mi} is the fitted constant of the original (unimpregnated) sample, ρ_x is the electronic density of the impregnant, and ρ the electronic density of carbon (graphite).

Using the fitting constant B_{gr} and assuming grains form spherically, a rough estimate of the volume of impregnant forming grains can also be made. Using Equations 3.52, 3.53 and 3.54 while replacing the autocorrelation length and radius of gyration of the micropores with those of the impregnant grains and C_{mi} with B_{gr}, all fit from Equation 3.55, will yield a V^{0}_{mi} for impregnant grains. This can be written as a fraction of the total impregnant and compared with that filling the micropores, leaving the remainder as forming large grains. The contribution to the scattering from the large grains is captured by the A/q^n term (or by the observed increase in scattering intensity at low q values).

Typically, high q intensity will decrease as micropores fill (if the species shows an affinity for micropores). Figure 3.10 a) shows a calculation of the effects of micropore filling without regard to other impregnant activity. As micropores fill, the intensity at high q drops substantially. Intermediate q intensity and B_{gr} will vary less predictably with loading as grains both form and accrete to become part of the large size group characterized by A. Figure 3.10 b) shows the result of unhindered impregnant micrograin formation on the carbon substrate relative to an unimpregnated carbon signal. For the

impregnated sample calculation, the intermediate q intensity rises substantially, while low q and high q intensity also see some increases. Low q intensity and A will increase with increasing impregnant loading from the unimpregnated carbon value as large grains form in the carbon's meso- and macropores. Figure 3.10 c) shows the result of this activity; high q intensity is barely changed while low q intensity rises substantially. High amounts of grain formation can mask a drop in high q intensity because the micropore signal "rides" on the intensity scattered from the grains, so comparing C_{mi} values, which tend to decrease with loading, is essential. Figure 3.10 d) shows the effects of both micropore filling to the same extent as Figure 3.10 a) and identical micrograin formation to Figure 3.10 b), which shows that micrograins tend to mask some of the micropore filling activity, underscoring the need for C_{mi} values.

Using this model and interpretation, the impregnated activated carbons studied in Chapter 4 can be divided into two broad groups, labeled Type A and Type B. Type A is marked by impregnant addition in micropores, and grain formation in mesopores and macropores (as evidenced by decreases in C_{mi} and increases in A and B_{gr}). Type B is characterized by grain formation in the mesopores and macropores but little to no impregnant addition in the micropores (A and B_{gr} increase, but C_{mi} stays relatively constant).

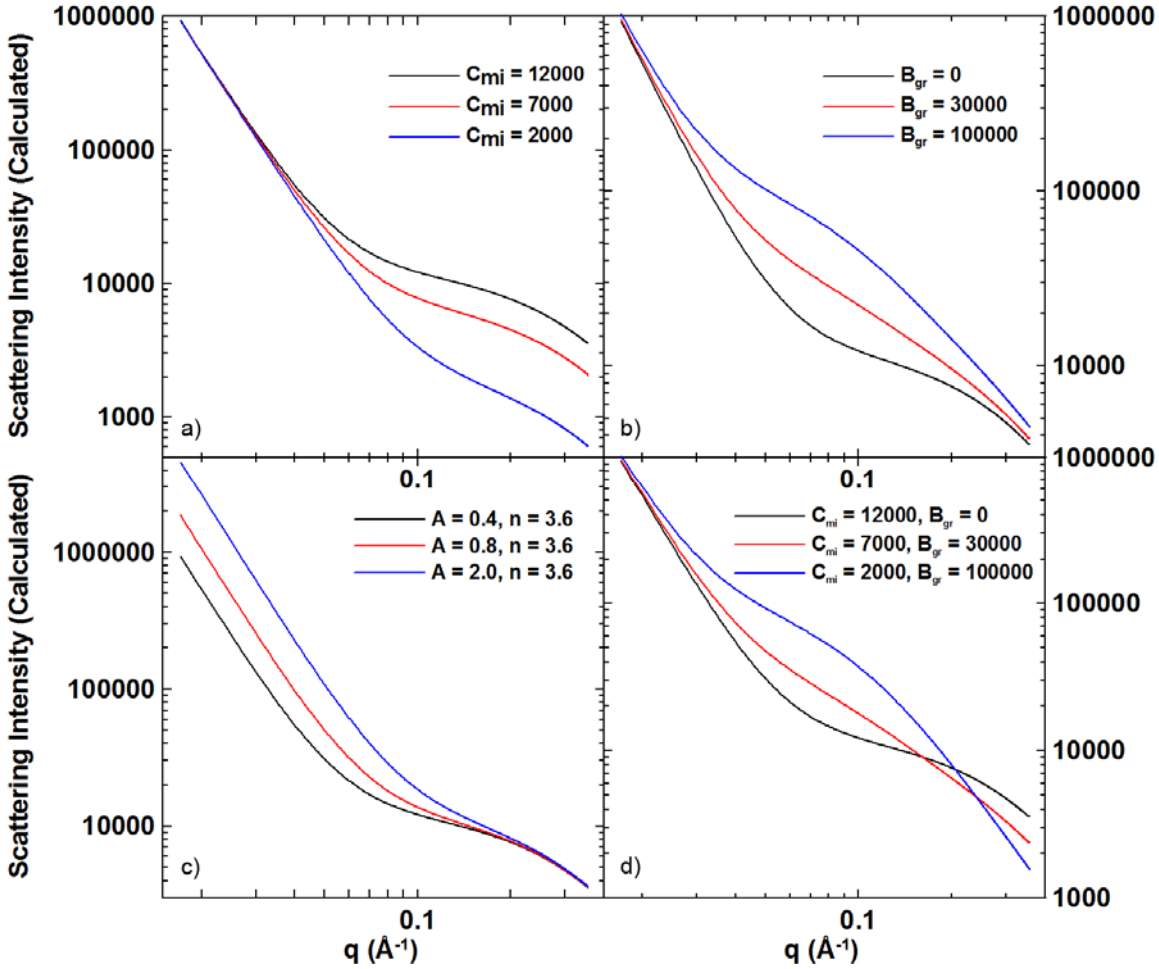

Figure 3.12 Theoretical SAXS data calculated using the modified Kalliat equation. In a), solely the effects of impregnant entering micropores are shown; in b), only the impact of micrograin formation; in c), exclusively large grain formation in meso- and macropores; in d), both micropore filling and micrograin formation. Scaling constants such as I_{0K}, $I_{0K'}$, ρ and ρ_{av} are set as unity for convenience. The black curve is an identical, unimpregnated baseline in a) through d), with A = 0.4, n = 3.6, C_{mi} = 12000, B_{gr} = 0, and b = 2.58 Å. The legends in the panels indicate which parameters have been changed for the red and blue curves. Micrograin intensity in b) and d) is calculated with a = 8.5 Å.

CHAPTER 4 IMPREGNATED ACTIVATED CARBON RESULTS

4.1 IMPREGNANT LOADING

For the five species studied, Kuraray GC impregnant loadings begin at about 5% (loading defined in Equation 2.1) and increase sequentially. Figure 4.1 shows a comparison between measured loadings and predicted loadings for the IACs in this work, with predictions calculated by the product of the volume of solution imbibed and the concentration of species in the solution. The predicted loadings ignore all reactions or out-gassing processes that might change the deposited species, such as those that create CO or CO_2 [50], and are calculated from the volume and concentration of chemical solution added to the carbon. Deviations from the prediction in panels a), b), c), and e) can be explained through measurement error and atmospheric water vapour adsorption. The silver nitrate in panel d) is the clear outlier and silver metal was observed (by WAXS) to be impregnated in the carbon in lieu of silver nitrate. Silver is formed through some unknown reaction mechanism with a probable conversion of some combination of nitrates, carbon functional groups and carbon to gases which would create the observed shortfall in mass. This has been previously observed [50, 51].

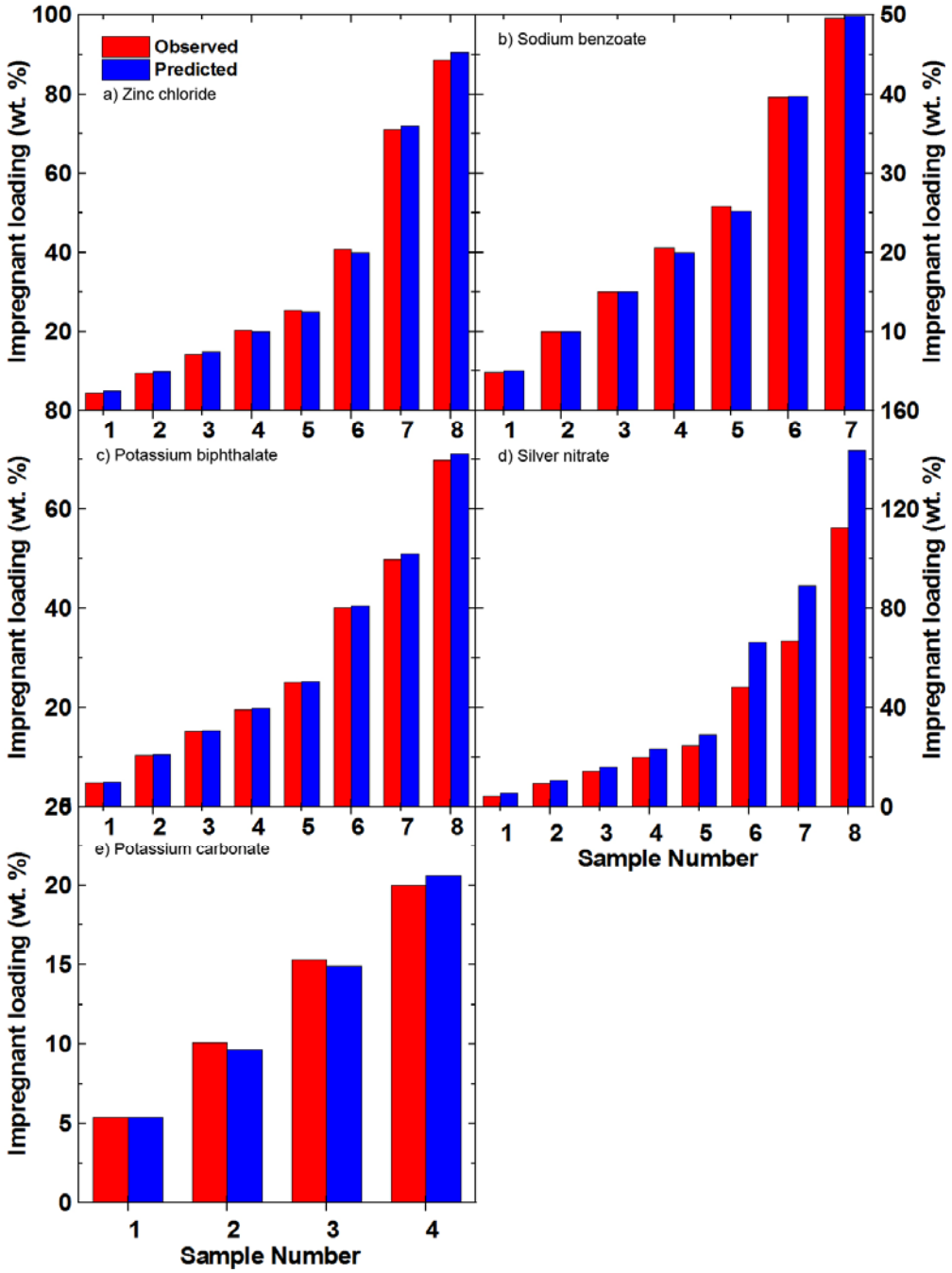

Figure 4.1 A comparison of observed (weighed) and predicted impregnant loadings for the species used in this study. Predictions were calculated from the concentration of the imbibed species, and assumed that the dry weight of the species was wholly deposited in the carbon and there were no reactions that caused a loss of mass.

4.2 SPECIES BEHAVIOUR AND FITS

As discussed in Chapter 3, the IACs can be divided into two broad groups, labeled Type A and Type B. Type A is marked by impregnant addition in micropores, and grain formation in mesopores and macropores while Type B is characterized by grain formation in the large meso- and macropores but little to no impregnant addition in the micropores and relatively small amounts of micrograin formation. It is also theoretically possible that there are other groups of behaviours beyond Types A and B, such as micropore filling and micrograin formation but a tendency against agglomeration of large grains, but these were not observed.

Categorizing a given chemical species can be most effectively accomplished by using the quantitative results of fitting to the modified Kalliat model, discussed in Chapter 3. It is important to rely on these quantitative values for the fitting parameters to judge impregnant behaviour as appearances can be deceiving. Since the signal is a summation of components, a decrease in one parameter can be qualitatively hidden by an increase in another.

Table A.2 in Appendix 1 gives data from all the IACs impregnated with different species at different loadings. Selected parameters from Equations 3.50 and 3.55 are listed as well as micrograin volume, micropore filling fraction and fitting error. Figures 4.2, 4.3, 4.4, 4.5 and 4.6 show the SAXS data collected from the five species along with Kalliat model

fits to the data, with the fit parameters found in Table A.2. All raw SAXS data found in this chapter was "normalized" as described in Chapter 2.

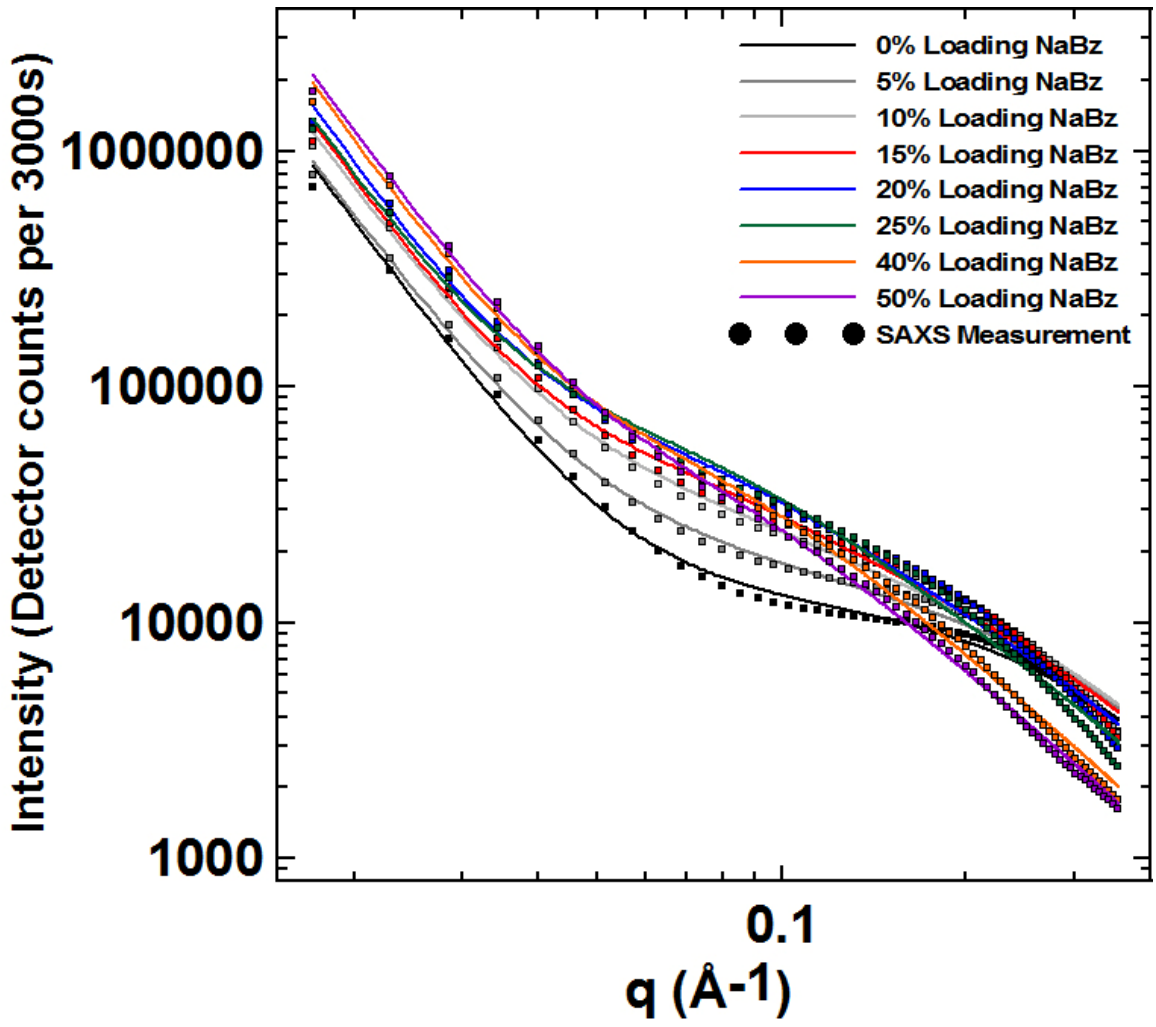

Figure 4.2 SAXS data (for clarity, only every eighth data point is shown) for a set of Kuraray GC samples impregnated at various loadings with sodium benzoate. Fits are given as solid curves. Data was collected over a scattering range of q = 0.015 - 0.356 $Å^{-1}$ (scattering angle of 0.23 º - 5.00º).

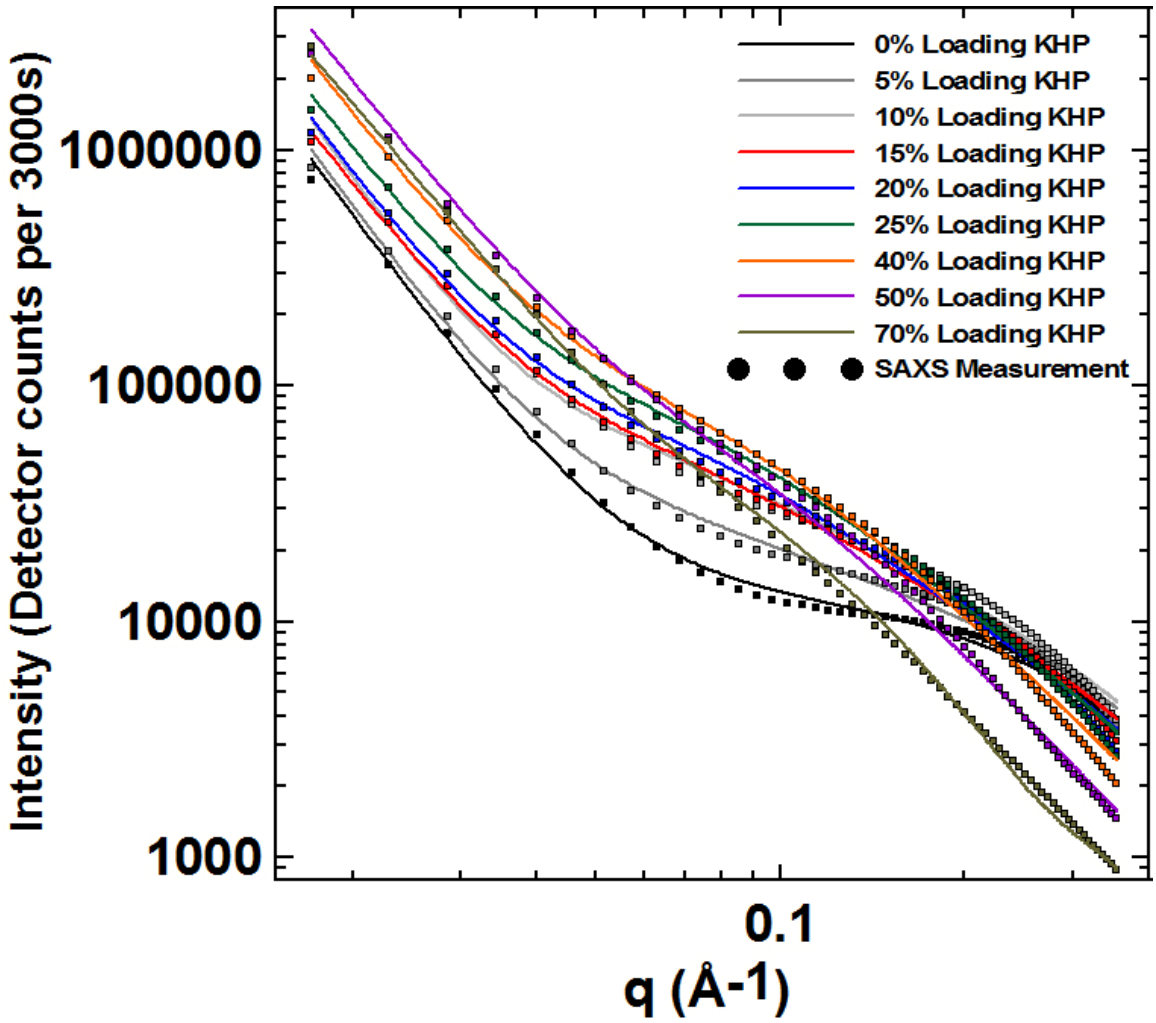

Figure 4.3 SAXS data (for clarity, only every eighth data point is shown) for a set of Kuraray GC samples impregnated at various loadings with potassium biphthalate. Fits are given as solid curves. Data was collected over a scattering range of q = 0.015 - 0.356 $Å^{-1}$ (scattering angle of 0.23 º - 5.00º).

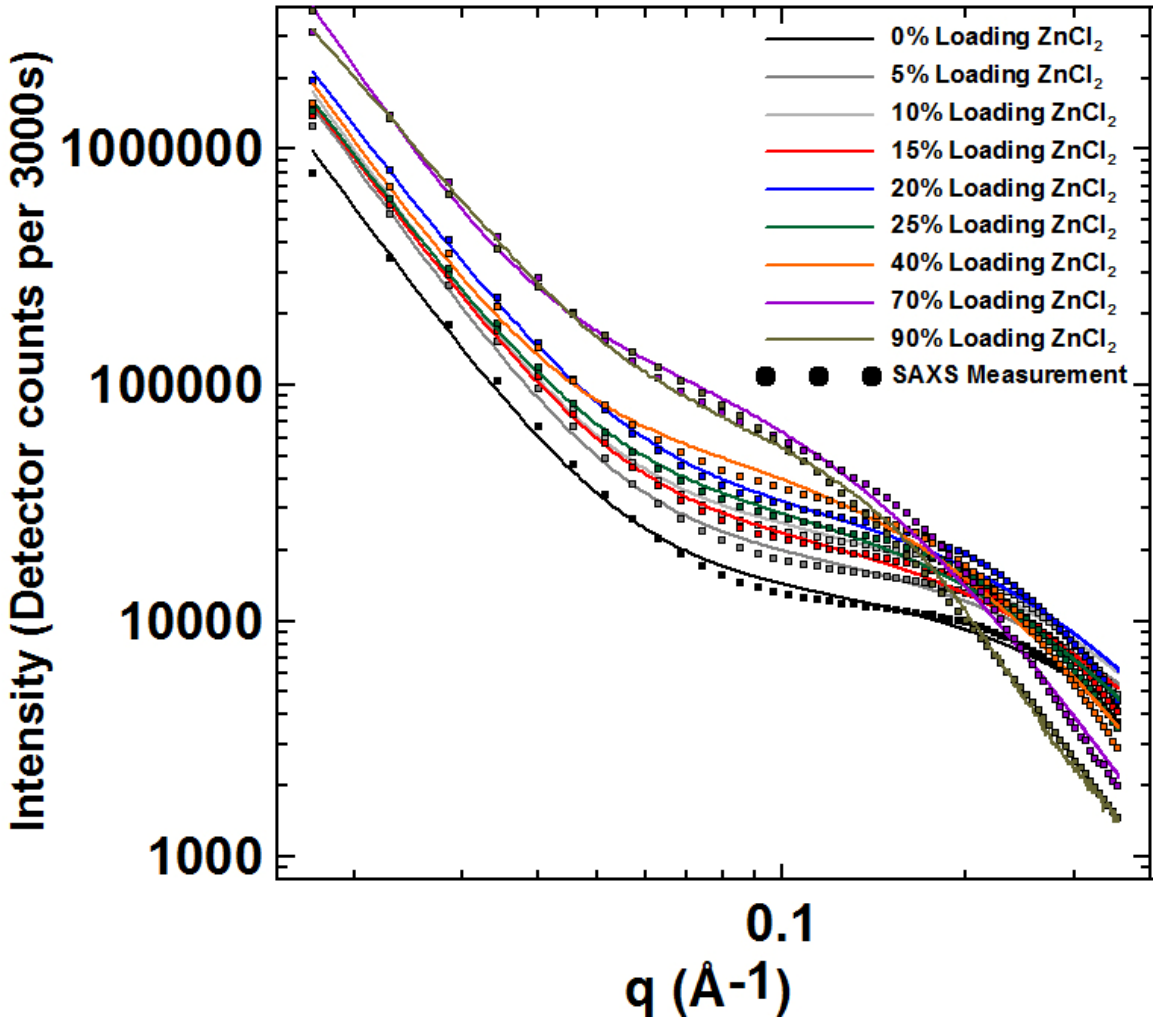

Figure 4.4 SAXS data (for clarity, only every eighth data point is shown) for a set of Kuraray GC samples impregnated at various loadings with zinc chloride. Fits are given as solid curves. Data was collected over a scattering range of q = 0.015 - 0.356 Å^{-1} (scattering angle of 0.23 º - 5.00º).

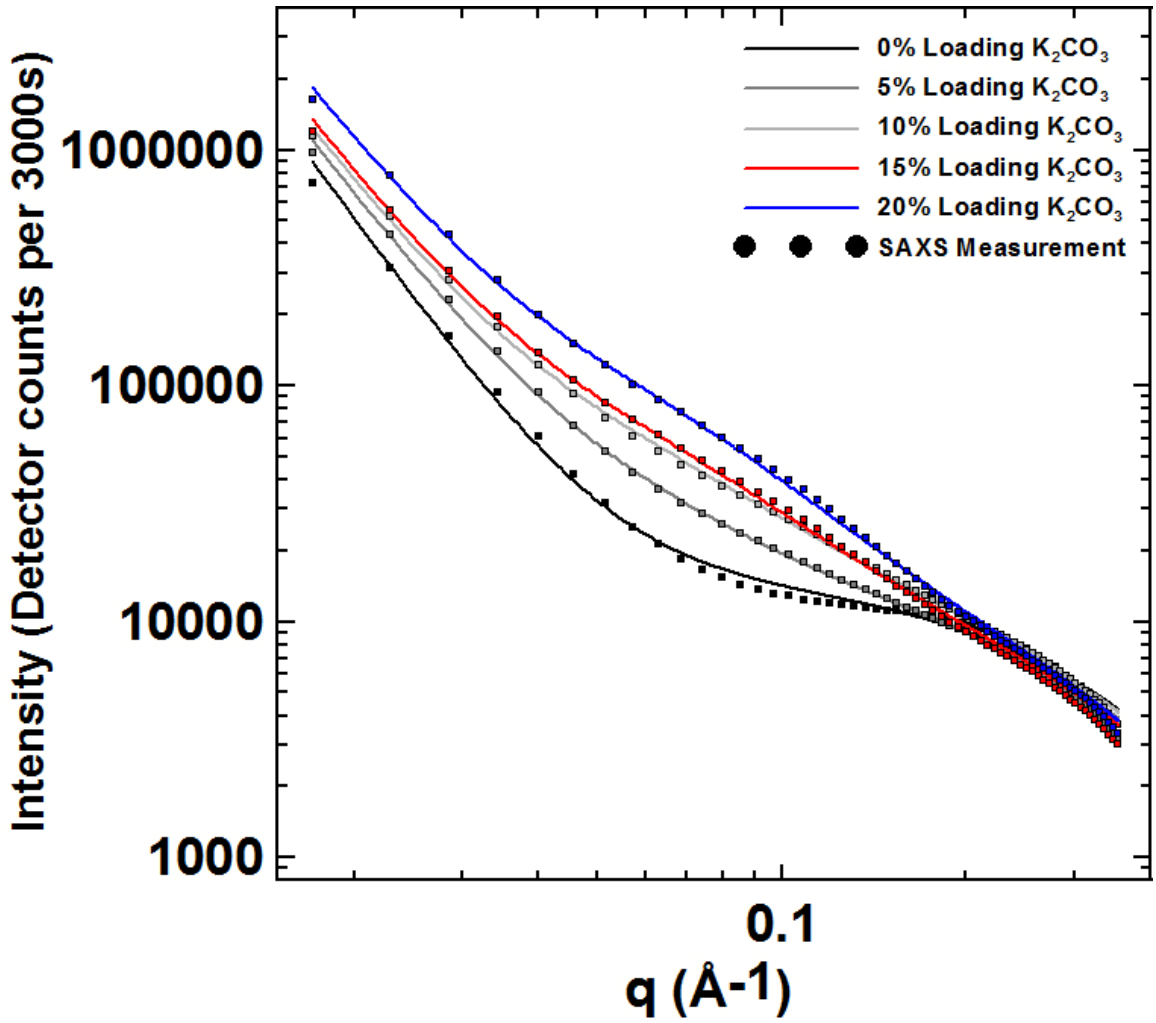

Figure 4.5 SAXS data (for clarity, only every eighth data point is shown) for a set of Kuraray GC samples impregnated at various loadings with potassium carbonate. Fits are given as solid curves. Data was collected over a scattering range of q = 0.015 - 0.356 $Å^{-1}$ (scattering angle of 0.23 º - 5.00º).

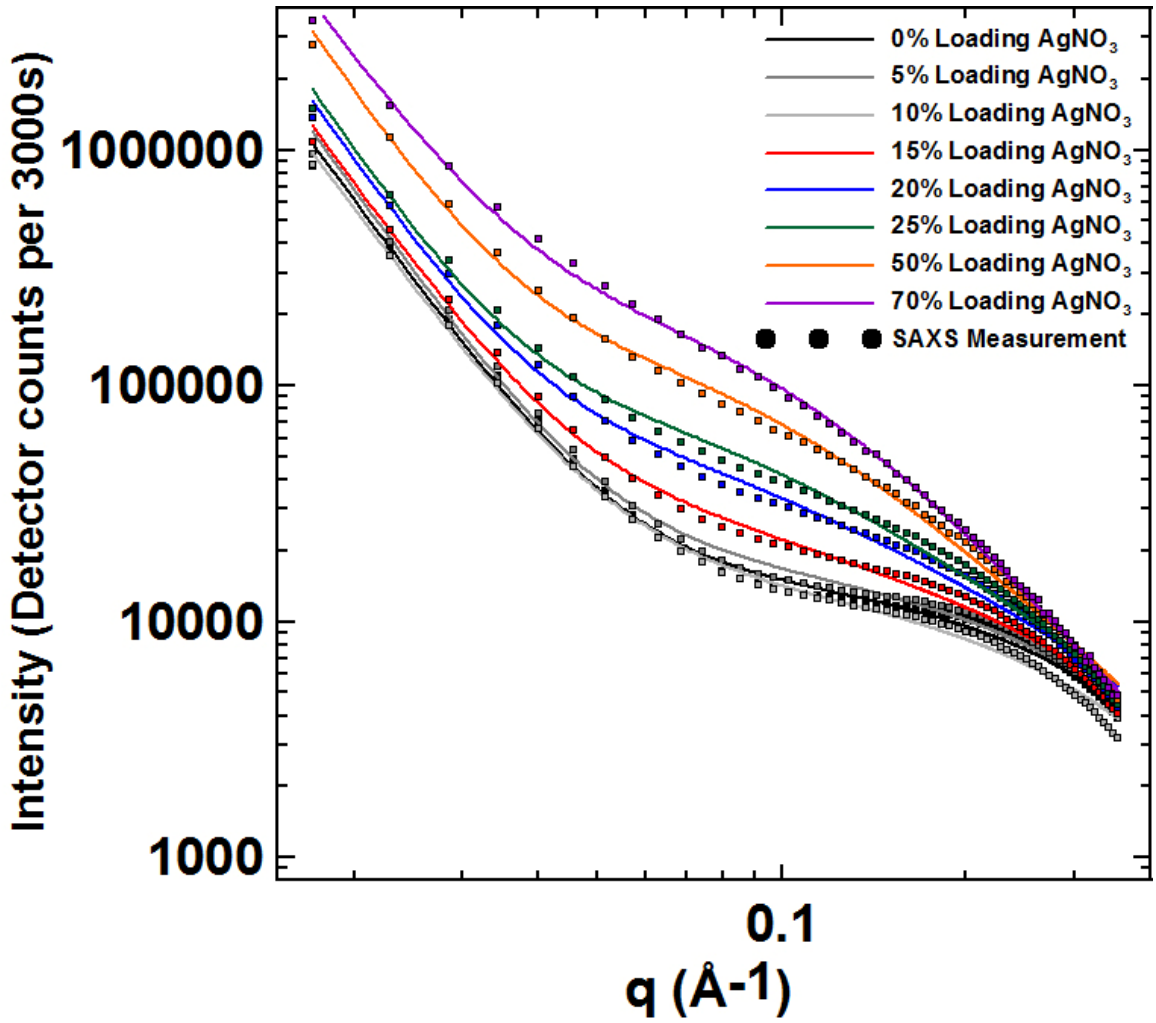

Figure 4.6 SAXS data (for clarity, only every eighth data point is shown) for a set of Kuraray GC samples impregnated at various loadings with silver nitrate. Fits are given as solid curves. Data was collected over a scattering range of q = 0.015 - 0.356 $Å^{-1}$ (scattering angle of 0.23 º - 5.00º).

In Figures 4.2 through 4.6, fitting error (measured by χ^2 and found in Table A.2) tends to increase with loading until 20-25%, then decreases to the level of the initial error. This is visible in the graphs, as trend lines progressively miss more of the middle region with loading and then capture most data at 40% and 50% loading (potassium carbonate data does not go as high in loading and is thus excluded from the discussion). This phenomenon is explored more in Figure 4.7. Because of the potential for the misidentification of signals using a simple model (i.e micropore signal being counted as micrograin intensity), one of the most effective fitting strategies for getting useable fitted parameters was forcing the micrograin size for all impregnated samples to be that of the unconstrained fit for the highest loading sample studied for a given species. It is likely micrograins grow modestly in size with loading, so this approach generates error. Letting the fit size for micrograins shrink from 8.5 Å to 6.5 Å, for example, shrinks error to χ^2 = 2.57 from χ^2 = 6.10, visible in Figure 4.7, but introduces physically impossible predictions of impregnant volume into the micropores. Allowing no constraints on the error-minimizing fitting routine results in an even lower *a* of 4.5 Å and χ^2 error of 0.34, neatly tracking the SAXS data in Figure 4.7, but removes the micropore fitting term entirely from the model, an obviously impossible outcome. The behaviour of fits as loading increases likely results in part from the interference effects previously described and may be ameliorated by using different types of carbon, however a detailed analysis of this problem and possible solutions could be conducted in future work.

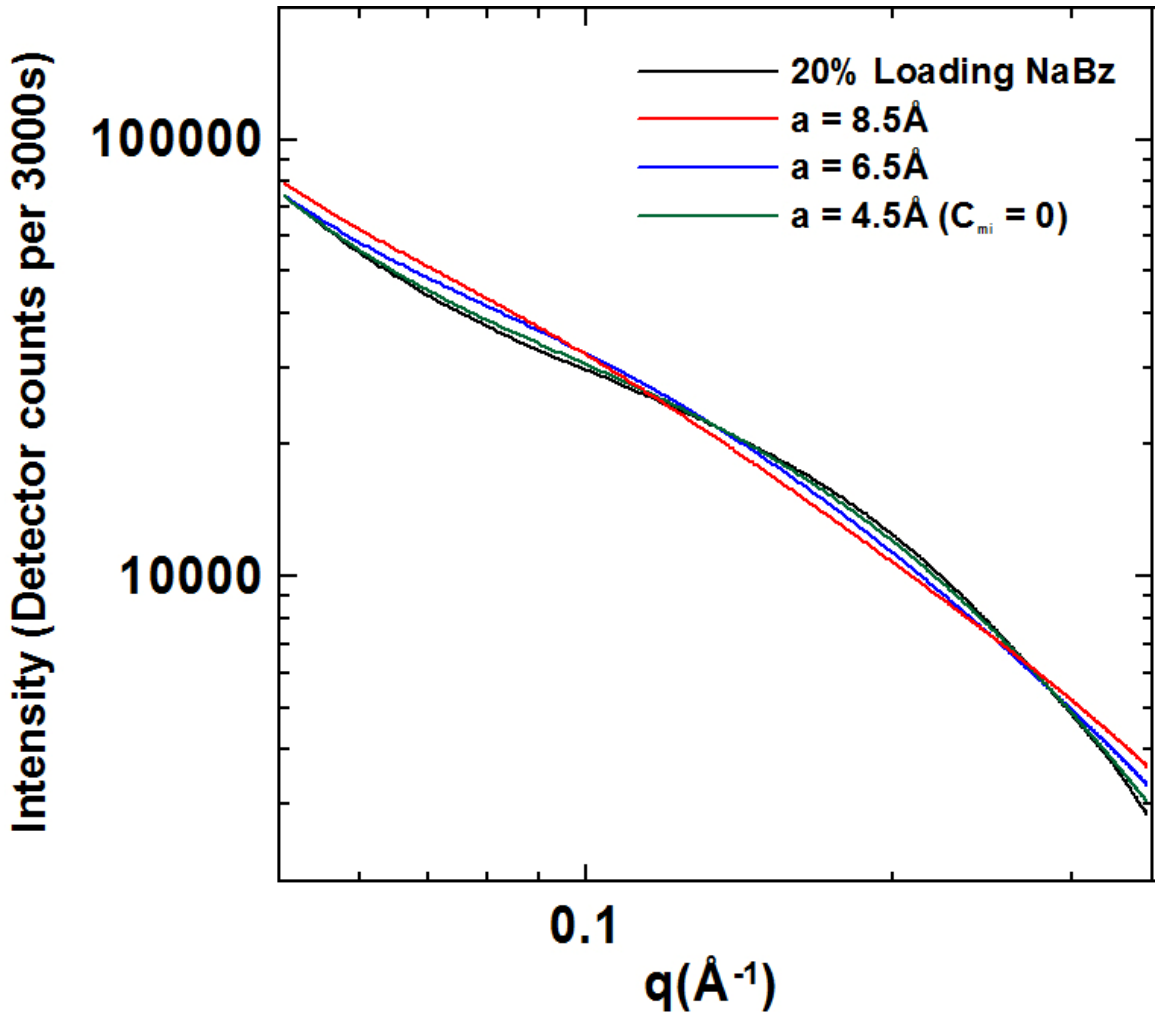

Figure 4.7 SAXS data for Kuraray GC impregnated with NaBz at 20% loading along with three fits calculated using Equation 3.55. Only data in mid-range q from 0.05 $Å^{-1}$ to 0.356 $Å^{-1}$ (scattering angle of 0.71 º - 5.00º) was shown for clarity. In the first two fits, the variable a was fixed to 8.5 Å and 6.5 Å respectively, giving nonzero C_{mi} values, while the third fit relaxed all constraints on the error minimization routine to get a of 4.5 Å and C_{mi} of 0.

4.3 SPECIES RESULTS

Table A.2 includes data from NaBz-impregnated GC with scattering curves shown in Figure 4.8. Loadings of sodium benzoate ranged from about 5% to 50%. The table suggests that n is largely constant over loading, while A/q^n calculated at a given q (not shown) tends to slowly increase with loading, a visible trend in Figure 4.8.

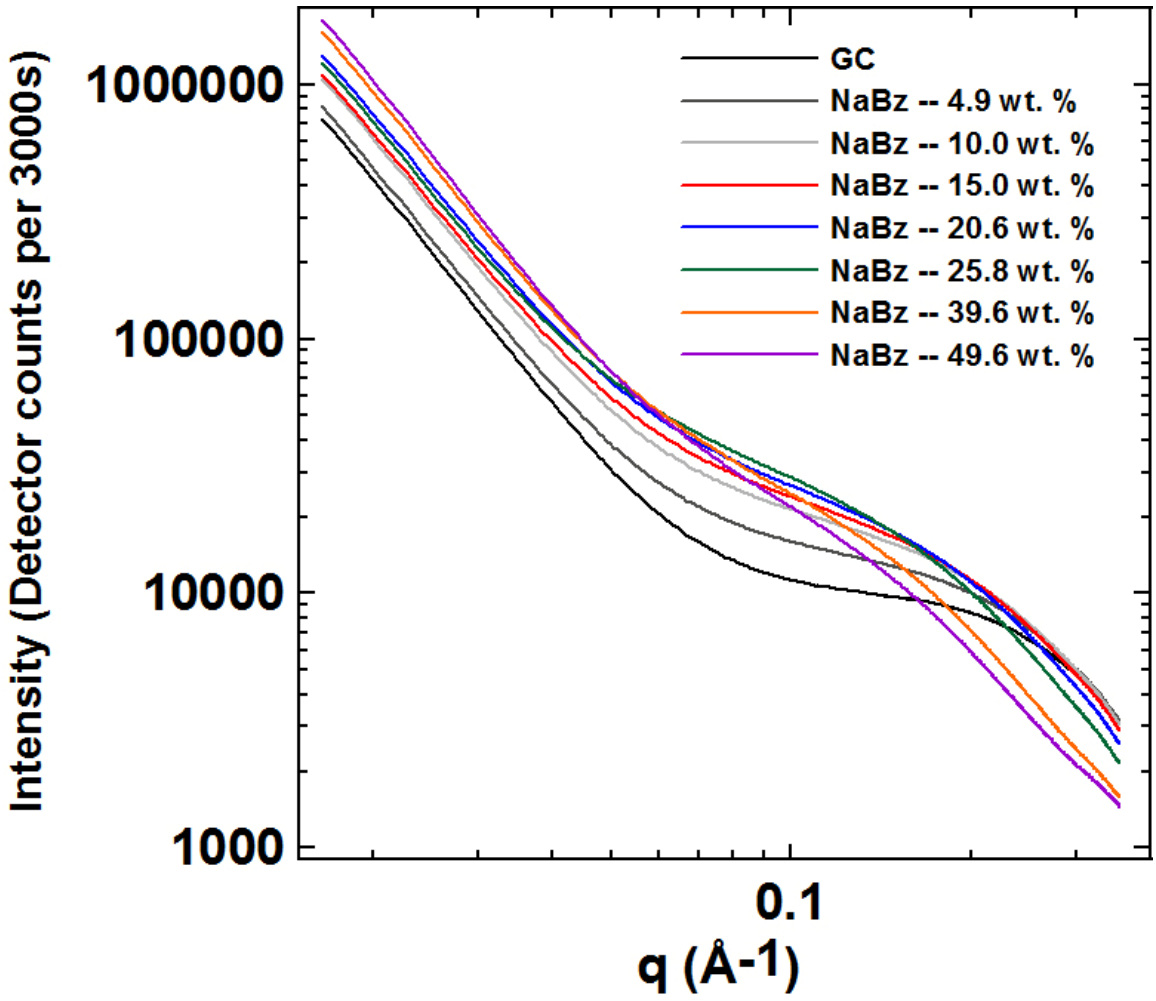

Figure 4.8 A comparison of SAXS data of Kuraray GC impregnated with the Type A species sodium benzoate at seven different loadings. Data was collected over a scattering range of q = 0.015 - 0.356 Å^{-1} (scattering angle of 0.23 º - 5.00º).

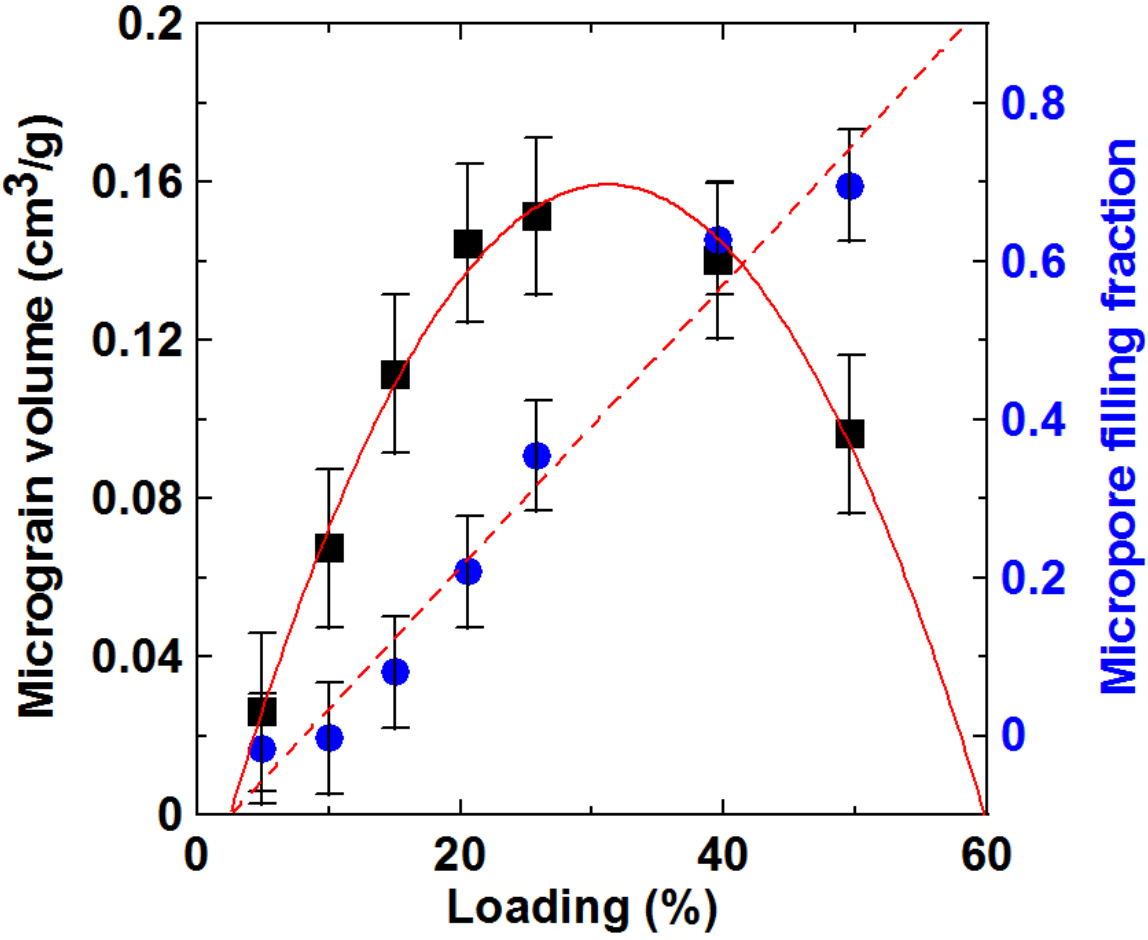

Figure 4.9 Micrograin volume and micropore filling fraction given with respect to the loading of NaBz-based IACs. Trend lines are given as a guide to the eye.

Sodium benzoate solutions have a contact angle near 65° on highly oriented pyrolytic graphite (HOPG) [22], which suggests effective micropore impregnation. Figure 4.9 shows the micrograin volume (V_{gr}) data and micropore filling fraction (V_{xmi}/V_{mi}) data plotted as a function of impregnant loading. V_{gr} roughly follows an inverted parabola and V_{xmi}/V_{mi} a linear trend. At high loadings, the linear trend is assumed to taper to a constant near full micropore filling. For the V_{gr} data, increasing amounts of relatively small grain size impregnant (< 30 Å) forms with increasing loading up to approximately 20%

impregnant loading. At higher loadings (> 20%), small grains increasingly agglomerate into large grains not included in the measure of V_{gr} and so there is a decrease in the values. As impregnant loading increases, the micropore filling fraction increases in a roughly linear manner, which is consistent with the observation in Figure 4.8 of declining intensity in the $q > 0.2$ Å^{-1} region. This shows that even at high impregnant loadings some of the impregnant is still entering the micropores. As the impregnant is entering all classes of pores and forming both small and large grains, the NaBz data shown in Figures 4.8 and 4.9 is indicative of Type A behaviour.

Data from KHP-impregnated GC can be found in Table A.2, with scattering curves shown in Figure 4.10. Loadings of potassium biphthalate ranged from about 5% to 70%. From the table it can be seen that n decreases slightly with loading, suggesting grain formation causes the carbon surface to appear more rough compared with sodium benzoate impregnated samples. A/q^n calculated at a given q increases with loading, consistent with Figure 4.10 where low q intensity steadily increases.

Figure 4.11 gives the micrograin volume (V_{gr}) data and micropore filling fraction (V_{xmi}/V_{mi}) data plotted as a function of impregnant loading for potassium biphthalate. The quantitative data is similar to that of NaBz, with V_{gr} following an inverted parabola and V_{xmi}/V_{mi} a linear trend. The explanation for this behaviour is the same: Up to medium loadings (20-30%), small grains form, as reflected in the V_{gr} data. After that point, these grains cluster into large grains too large for the micrograin fitting term, leading to a decrease in V_{gr}. Micropore filling fraction increases in a roughly linear manner,

correlating well with the visible decrease of scattering intensity in the $q > 0.2$ Å^{-1} region of Figure 4.10. This behaviour (small, large grain formation, filling of micropores) is indicative of Type A behaviour.

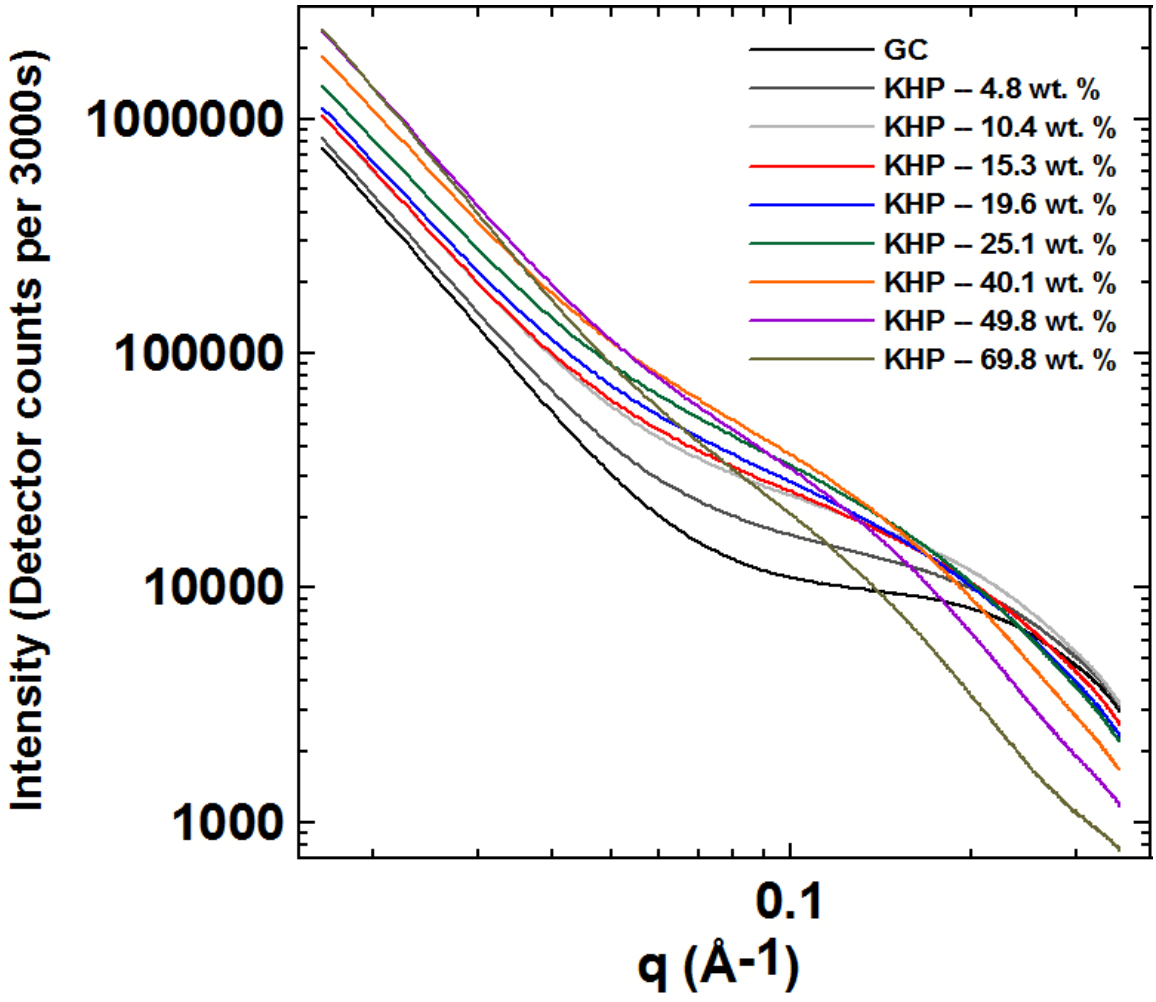

Figure 4.10 A comparison of SAXS data of Kuraray GC impregnated with the Type A species potassium biphthalate to eight different loadings. Data was collected over a scattering range of $q = 0.015$ - 0.356 Å^{-1} (scattering angle of 0.23 º - 5.00º).

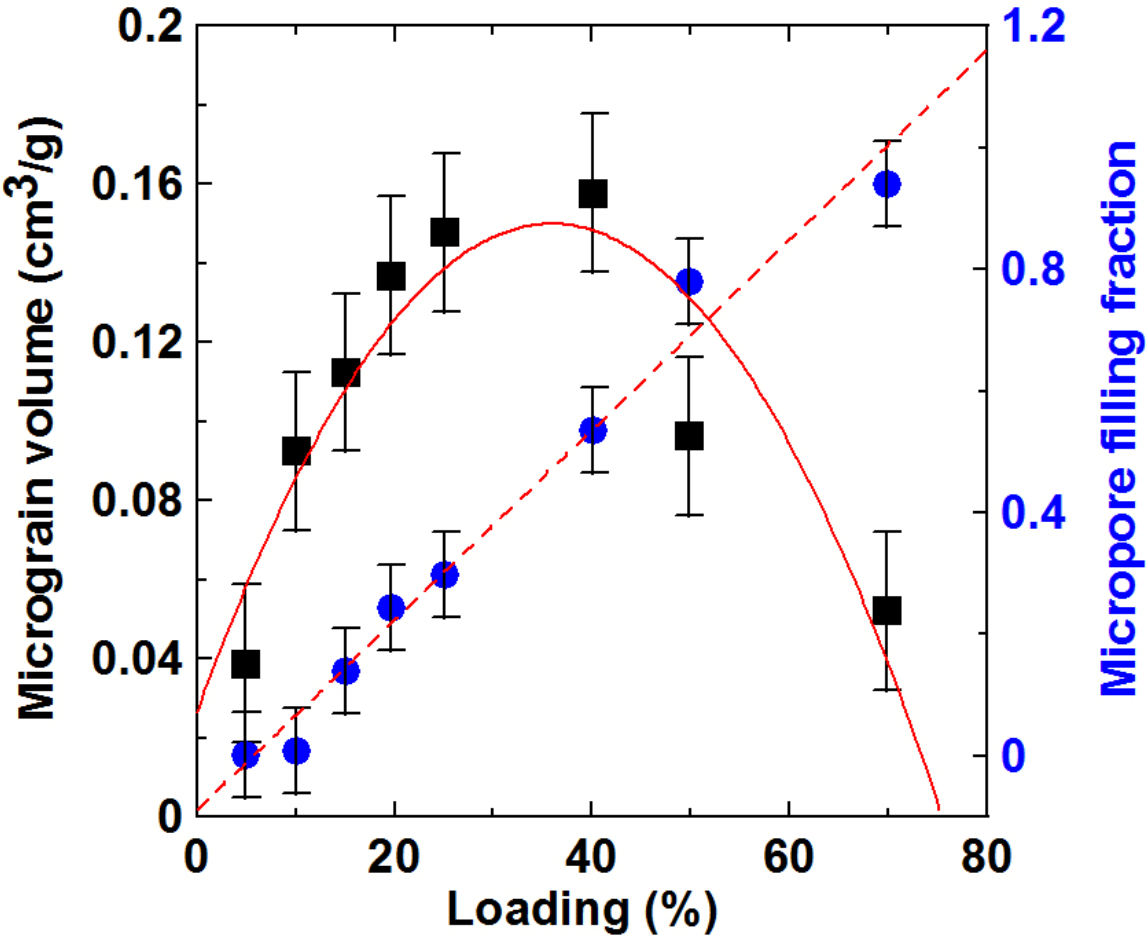

Figure 4.11 Micrograin volume and micropore filling fraction given with respect to the loading of KHP-based IACs. Trend lines are given as a guide to the eye.

Data from $ZnCl_2$-impregnated GC in Table A.2 suggests mostly similar behaviour compared to NaBz and KHP. Loadings of zinc chloride ranged from about 5% to 90%, with curves shown in Figure 4.12. One differing behaviour is apparent from a study of *n* values. *n* is constant with loading up to about 25%, but then increases to a value at high loadings indicative of a very smooth surface. A/q^n calculated at a given *q* increases with loading, making $ZnCl_2$ comparable to NaBz and KHP samples in this regard. Figure 4.12 also shows low *q* intensity steadily increasing.

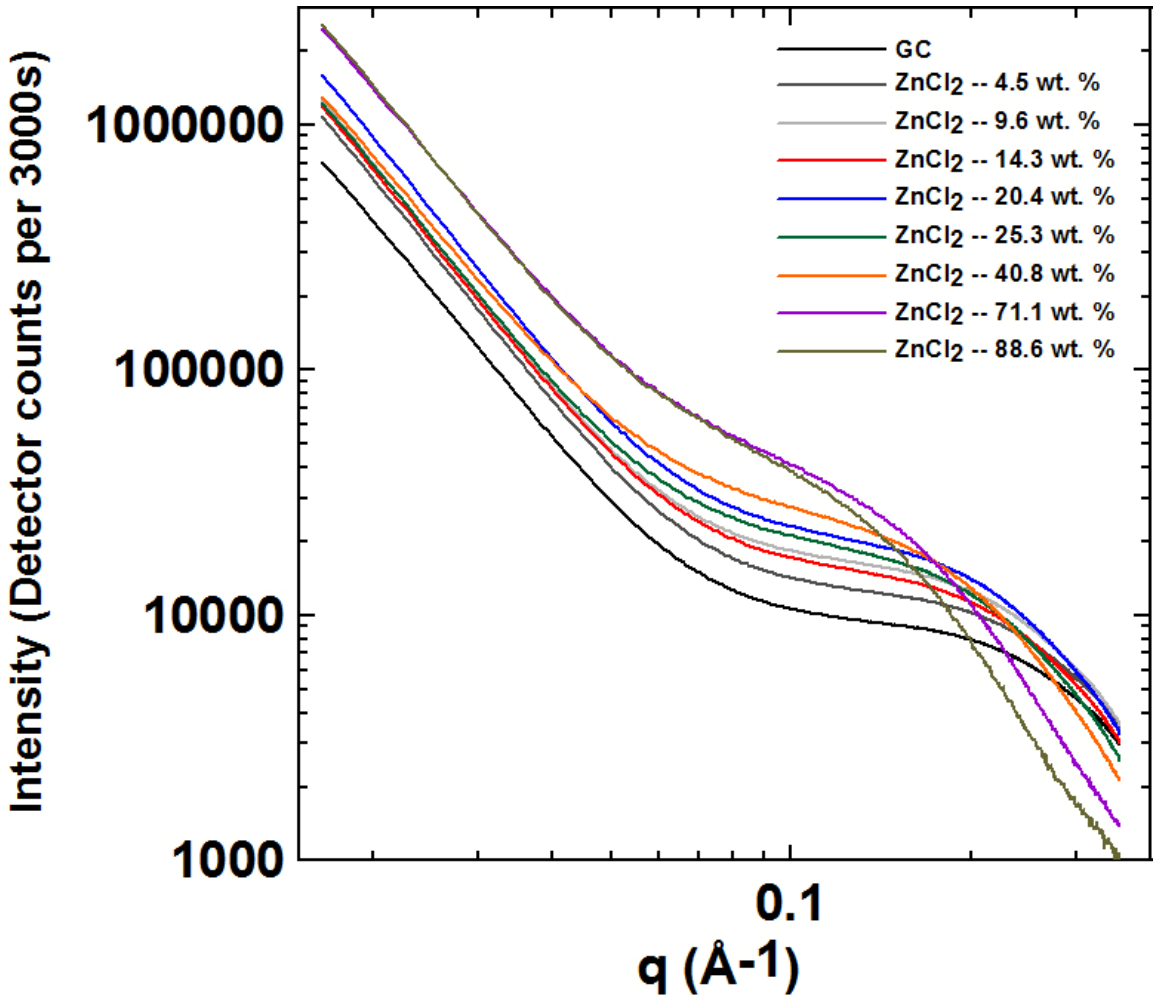

Figure 4.12 A comparison of SAXS data of Kuraray GC impregnated with the Type A species zinc chloride to eight different loadings. Data was collected over a scattering range of q = 0.015 - 0.356 Å^{-1} (scattering angle of 0.23 º - 5.00º).

The contact angle of zinc chloride solutions with HOPG has been found to be near 60^{o} [22] and decreases with concentration which suggests good micropore intake. For low loadings, this seems to be the case. Figure 4.13 displays micrograin volume (V_{gr}) data and micropore filling fraction (V_{xmi}/V_{mi}) data. As before, V_{gr} roughly follows an inverted parabola as grains form and agglomerate and V_{xmi}/V_{mi} a linear trend as micropores fill. However, micropore fitting signal beyond 25% loading was lost due to fitting constraints

and so only an extrapolation of micropore filling behaviour can be suggested, though it is likely it follows the example of NaBz and KHP samples since Figure 4.12 shows declining intensity in the $q > 0.2$ Å^{-1} region. $ZnCl_2$ can also be labeled as Type A due to this behaviour.

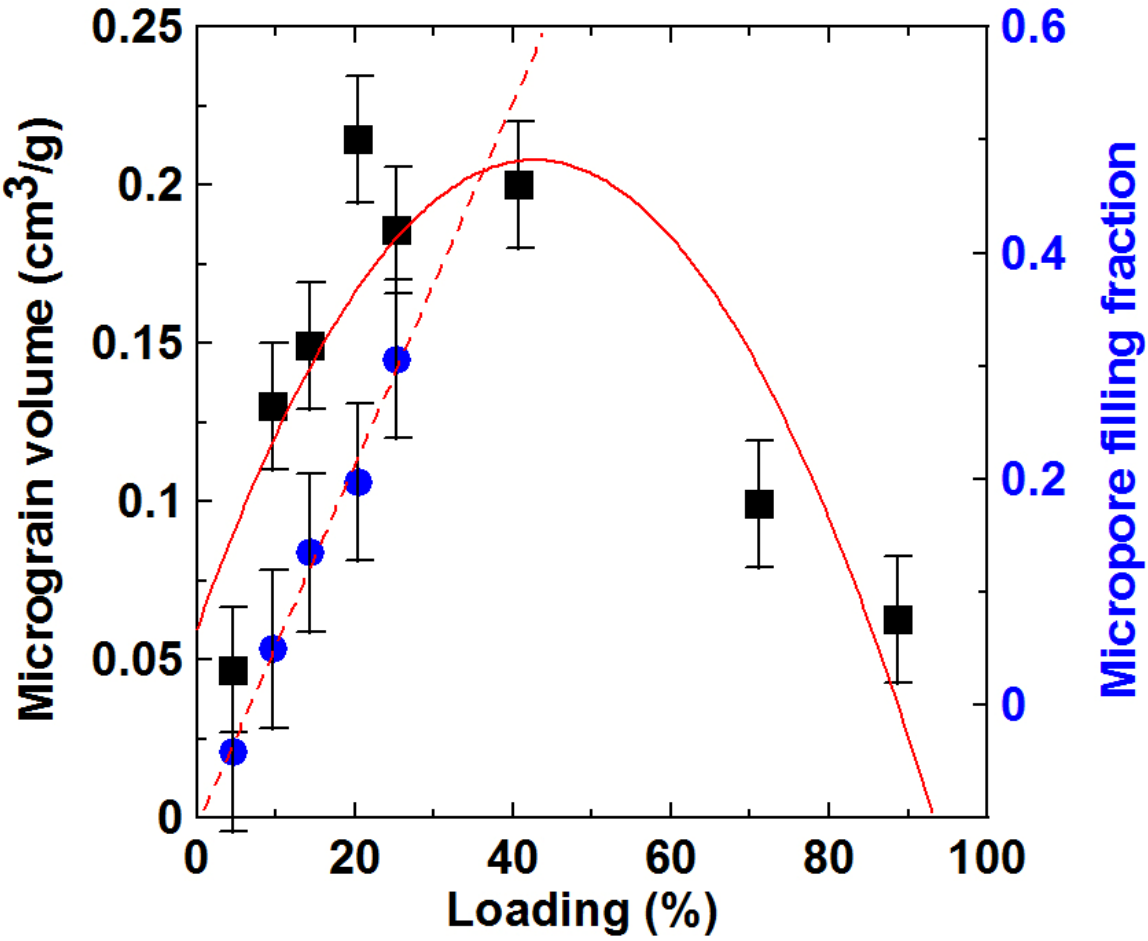

Figure 4.13 Micrograin volume and micropore filling fraction given with respect to the loading of $ZnCl_2$-based IACs. Trend lines are given as a guide to the eye.

Data from K_2CO_3-impregnated GC is listed in Table A.2, with scattering curves shown in Figure 4.14. Loadings of potassium carbonate ranged from about 5% to 20%. From the table it can be seen that *n* is constant with loading. As with IACs using other

impregnants, A/q^n calculated at a given q increases with loading, consistent with Figure 4.14 where low q intensity steadily increases.

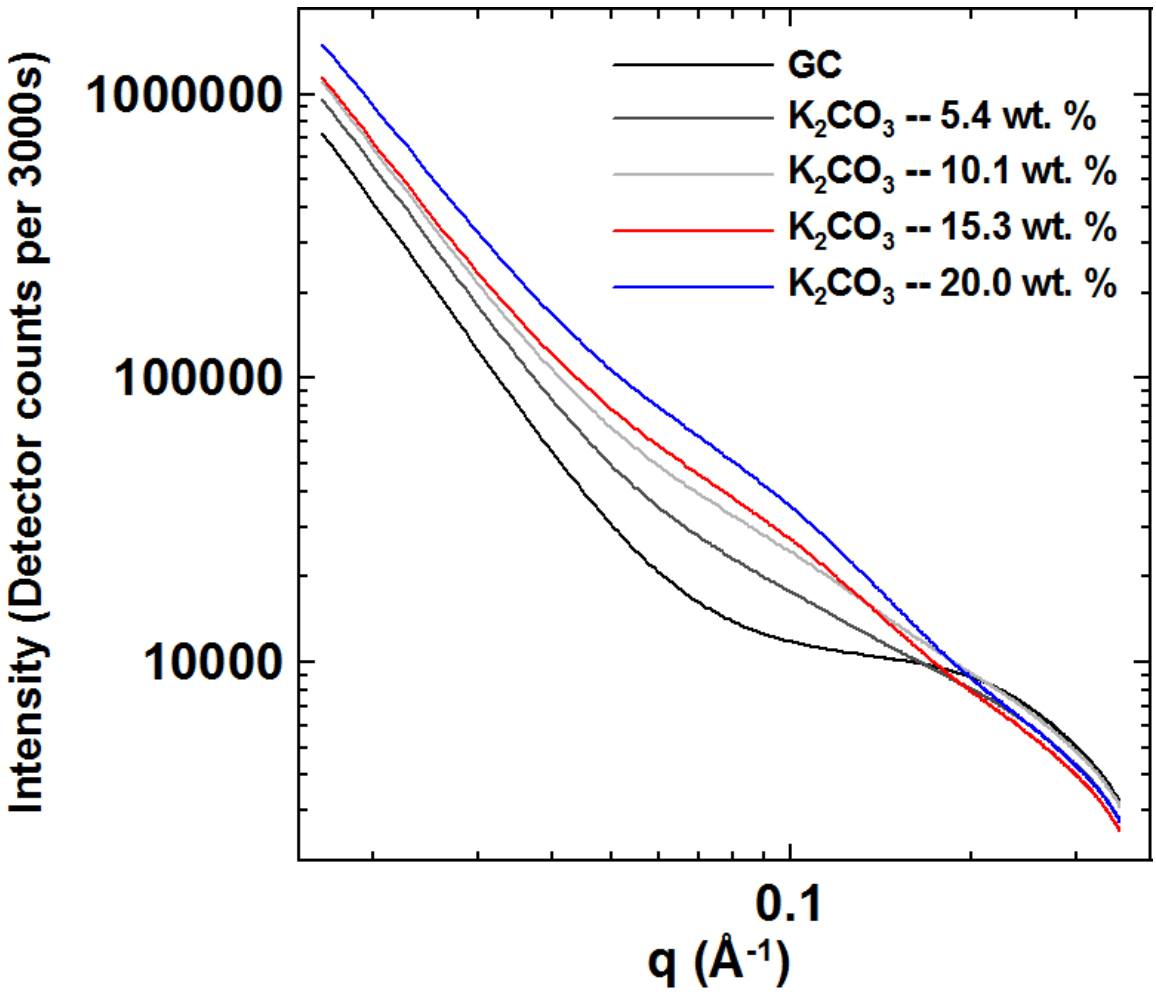

Figure 4.14 A comparison of SAXS data of Kuraray GC impregnated with the Type B species potassium carbonate to four different loadings. Data was collected over a scattering range of q = 0.015 - 0.356 Å^{-1} (scattering angle of 0.23 º - 5.00º).

Micrograin volume (V_{gr}) data and micropore filling fraction (V_{xmi}/V_{mi}) data are plotted as a function of impregnant loading in Figure 4.15. Error bars are larger here than for the other species, because experimental error for the IAC data is a constant and the

micrograin volume and micropore filling fraction values are substantially lower compared to the other impregnants. As there are less potassium carbonate samples, trends are not as defined as with other impregnants. Both micrograin volume and micropore filling seem to increase linearly, but slowly (though at the loadings studied a broad parabola could fit the micrograin volume data). Figure 4.14 seems to suggest no micropore filling at all, but qualitative trends can mislead. High q signal (i.e that of the micropores) rides on the signal from micrograins, which are also increasing gradually in Figure 4.15. Thus any visible decreases in micropore intensity (a sign of filling micropores) will be hidden at low loadings.

However, a comparison of the micropore filling fraction and micrograin volume at the highest loading (20%) with the values for the three Type A impregnants reveals that potassium carbonate is very ineffective at depositing in the micropores or forming micrograins. From the quantitative trends K_2CO_3 seems to be a Type B impregnant, albeit categorized with lower confidence than the other impregnants.

The final species studied is silver nitrate, with data given in Table A.2 and SAXS curves shown in Figure 4.16. This species is the outlier of the set. Loadings of $AgNO_3$ ranged from about 5% to 70%. n varies slightly with loading, though with no clear trend. As seen in Figure 4.16, A/q^n calculated at a given q increases fairly rapidly with loading.

It was observed that silver nitrate converts to silver metal during impregnation and drying as evidenced by wide-angle X-ray scattering (WAXS) data in Figure 4.17 a). SEM

images are formed largely by the detection of backscattered electrons, which have atomic number contrast, so the number of backscattered electrons increases almost monotonically with increasing atomic number. Regions of silver will thus appear brighter than carbon in electron microscopy, as in Figure 4.17 b). The silver crystals range from on the order of Ångstroms to some hundreds of micrometres across, depending on the loading, with a relatively even distribution of small (tens of Å) and large (hundreds of Å) grains. Since Kuraray GC carbon is washed with hydrochloric acid during manufacturing, some residual chlorine reacts to form silver chloride, also visible in Figure 4.17 a).

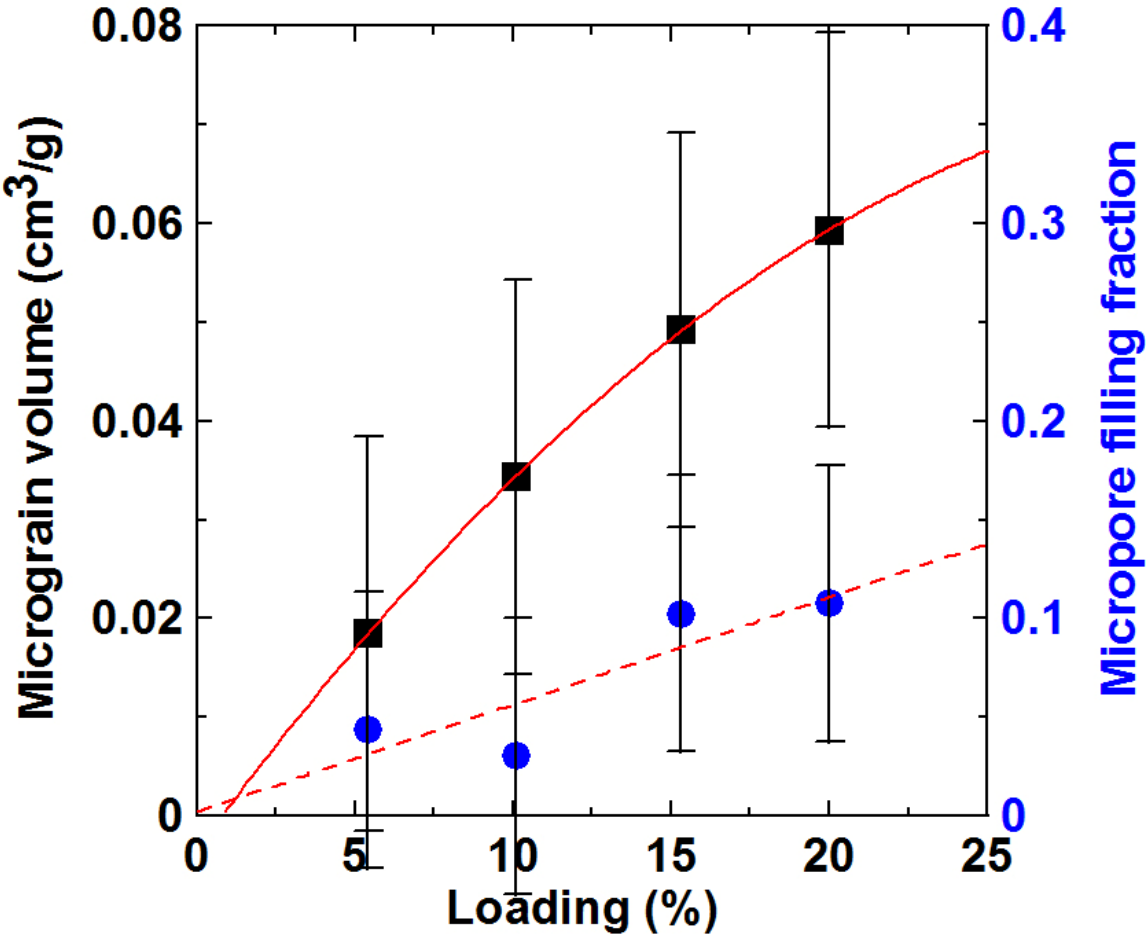

Figure 4.15 Micrograin volume and micropore filling fraction given with respect to the loading of K_2CO_3-based IACs. Trend lines are given as a guide to the eye.

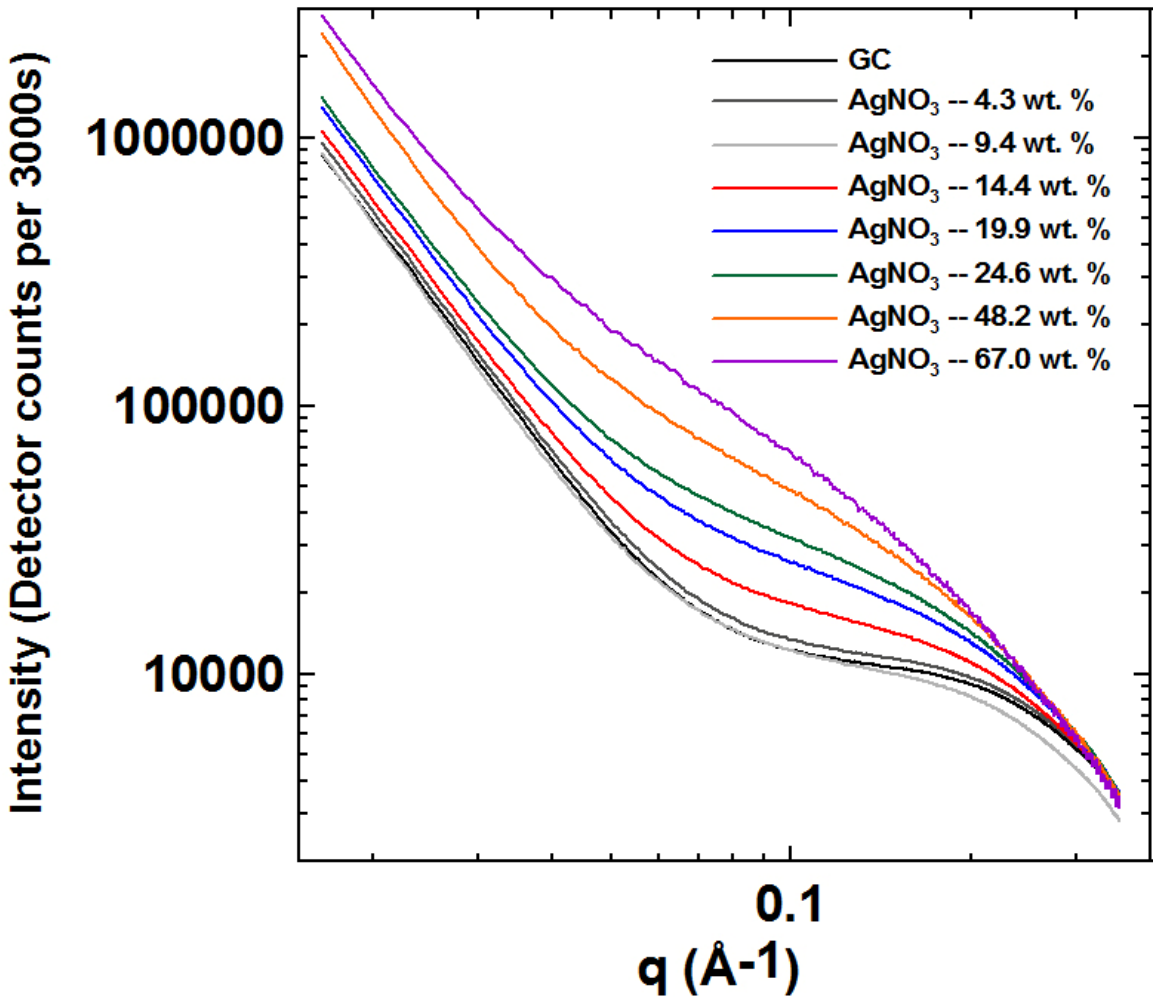

Figure 4.16 A comparison of SAXS data of Kuraray GC impregnated with the Type B species silver nitrate to seven different loadings. Data was collected over a scattering range of q = 0.015 - 0.356 Å^{-1} (scattering angle of 0.23 º - 5.00º).

Micrograin volume (V_{gr}) data and micropore filling fraction (V_{xmi}/V_{mi}) data are plotted as a function of impregnant loading in Figure 4.18. Here the behaviour is quite different compared to the first three species, and is similar to potassium carbonate. Both micrograin volume and micropore filling seem to increase linearly but extremely slowly. At high loadings micropore filling is only a small fraction of that of the Type A species

while micrograin formation is also very slow. In this case, the qualitative similarities of Figure 4.16 to Figure 4.14 (potassium carbonate) yield quantitative similarities as well. In Figure 4.18, there is very little drop in micropore signal even up to 50% loading, while micrograin growth is also slight. This behaviour is the mark of a Type B impregnant.

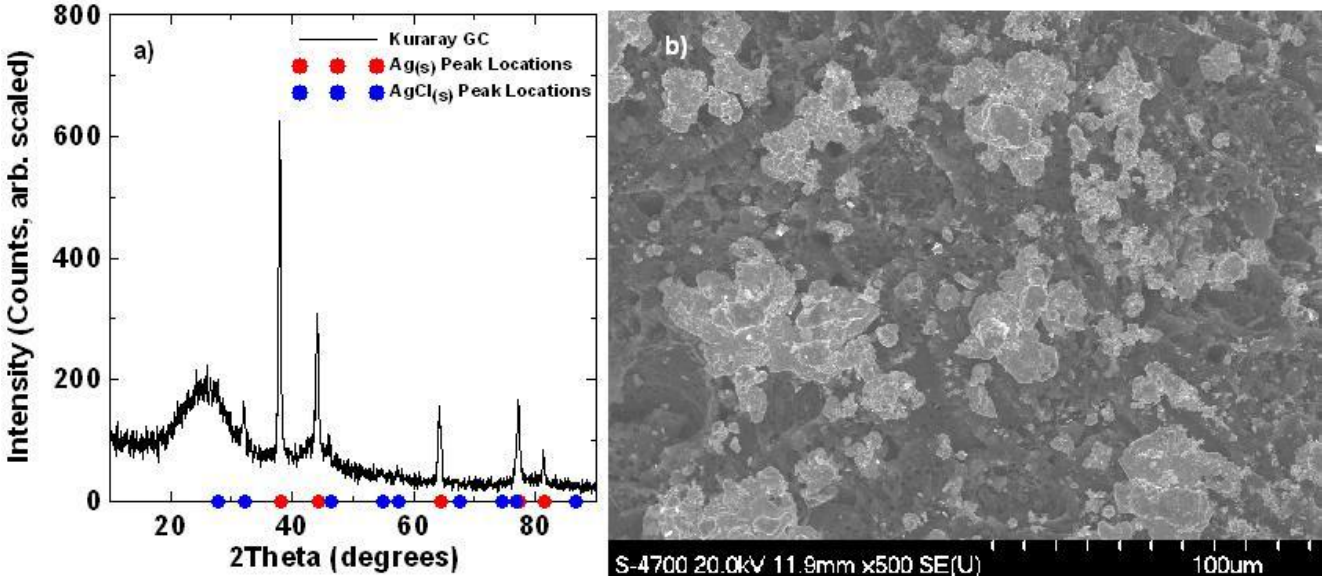

Figure 4.17 a) Wide-angle X-ray scattering data from silver nitrate-impregnated GC and b) a SEM image of the same sample. Silver crystals are visible in both. The Scherrer equation gives a mean crystallite size of 195 Å. Peak height qualitatively follows the same pattern as low q intensity in SAXS (that is, a steady increase) when measured as a function of impregnant loading.

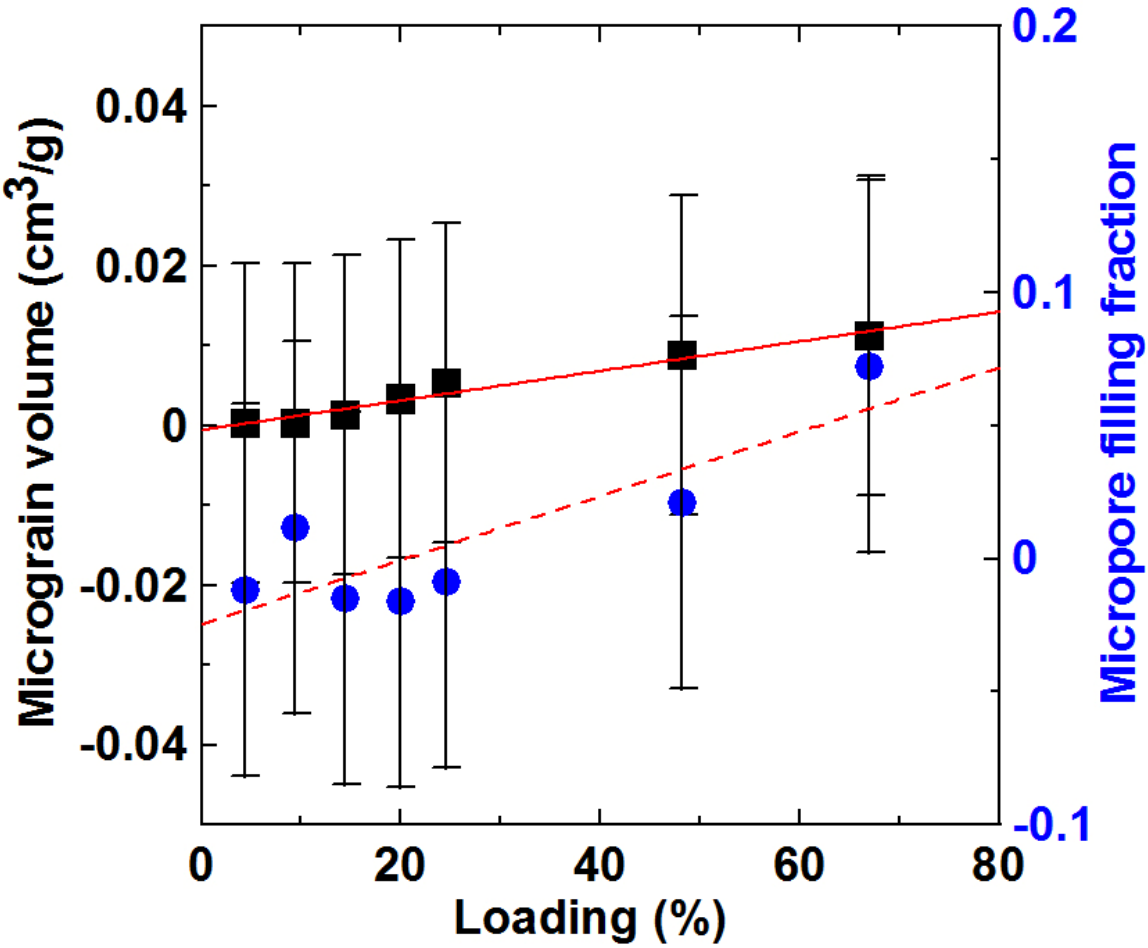

Figure 4.18 Micrograin volume and micropore filling fraction given with respect to the loading of $AgNO_3$-based IACs. Trend lines are given as a guide to the eye.

CHAPTER 5 SNCOC RESULTS

5.1 REMOVING BACKGROUND AND ISOLATING THE SNCOC SIGNAL

As described in Chapter 2, the in-situ coin cell is different from the typical coin cell because of the substitution of low-absorbing beryllium discs for the spring and spacer. However, in order to examine the SnCoC data there is still a significant background that must be stripped from the SAXS signal, primarily consisting of the copper foil electrode backing but also having small contributions from the lithium foil, beryllium discs, cell electrolyte and separators. The procedure and equation for removing a background signal is also detailed in Chapter 2. Briefly, it involves having the X-ray transmission factors and signals of both the entire cell and a "dummy cell" containing every material except SnCoC, then rearranging Equation 2.3 to calculate the required quantity (the SnCoC signal alone):

$$I_{SnCoC} = \frac{I_{SnCoCm}}{t_{SnCoC}} = \frac{I_{FCm}}{t_{FC}} - \frac{I_{DCm}}{t_{DC}}, \tag{5.1}$$

where *m* denotes "measured", I_{SnCoC}, I_{FC} and I_{DC} are the signals from the SnCoC electrode, full cell and dummy cell respectively, and t_{SnCoC}, t_{FC} and t_{DC} are their respective transmission factors. This procedure requires neither the transmission factor for SnCoC nor its "measured" intensity to be known to produce the scaled SnCoC intensity. As absolute units are not required for analysis of the SAXS data of SnCoC, as opposed to the activated carbon data in Chapter 4, its scattering intensity can also be

arbitrarily scaled as long as a method is used consistently between sets of data and henceforth the absolute value of scattering intensity is not related to any physical quantity of the SnCoC electrode.

Full cell, dummy cell and resultant SnCoC SAXS data are shown in Figure 5.1, with the SnCoC signal calculated using Equation 5.1. This cell is partially discharged; data for fully charged (delithiated) SnCoC is later given in Figure 5.4.

5.2 QUALITATIVE OBSERVATIONS

Figure 5.2 shows a set of SnCoC SAXS data, with the first five runs highlighted in red and every fifth run (up to the 80th) given in black. Data was taken for 3000s per run while runs were separated by 3220s due to the capture of glassy carbon and other reference data in order to calculate transmission factors. Cells were charged at ± 85 μA, cycling between 1.2 V and 0.005 V (approximately C/20 cycling). A graph of cell voltages versus run number is given in Figure 5.3 for comparison.

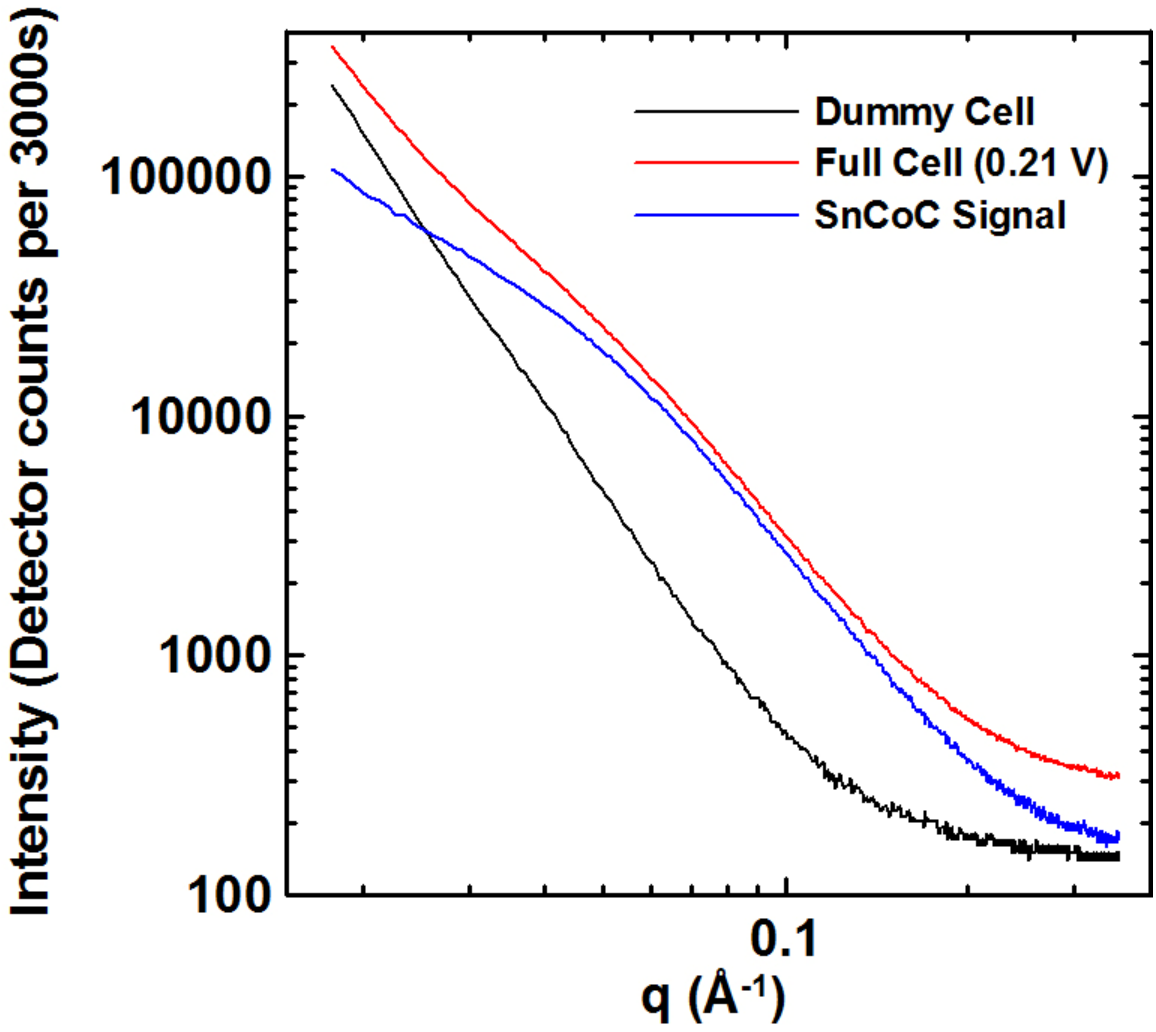

Figure 5.1 SAXS data from the dummy cell, full cell, and SnCoC electrode, where the cell is charged to 0.21 V and data was collected for 3000s. Transmission values for the dummy cell and full cell were 0.297 and 0.191 respectively. Data is shown over a scattering range of q = 0.018 - 0.356 $Å^{-1}$ (scattering angle of 0.25º - 5.00º), and is normalized by the procedures detailed in Chapter 2.

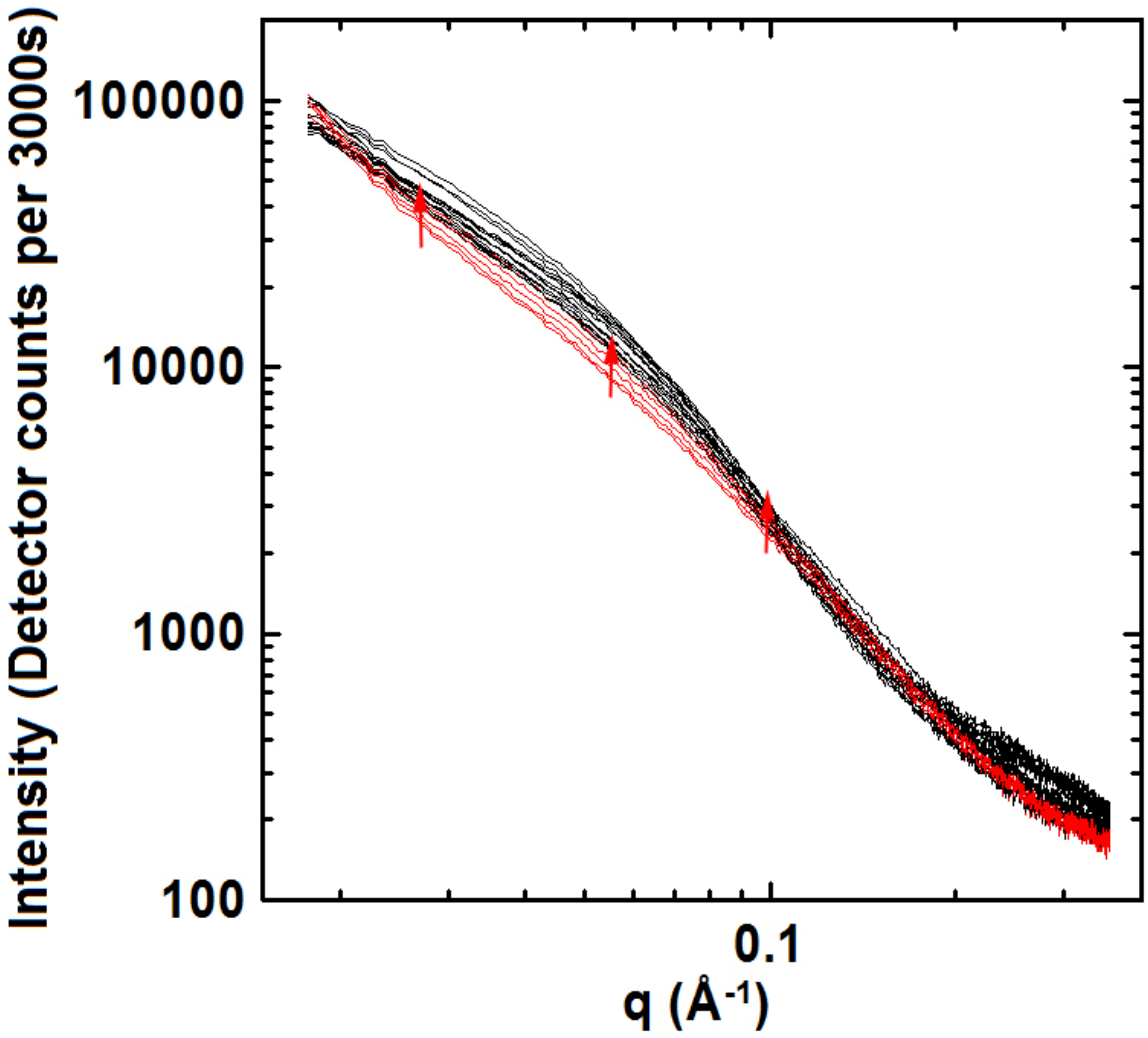

Figure 5.2 SnCoC SAXS data for the first 80 runs, representing a range of voltages. The first five runs are given in red, and the intensity initially grows as given by the arrows. The remaining SAXS patterns (every fifth run shown) then concentrate around a band of values higher than the initial intensities, even when voltage cycles back to the initial value. Data is normalized by the procedures found in Chapter 2.

Figure 5.2 shows that there is some permanent change in the cell as voltage cycles since SAXS curves never return to their original intensity, but the shape of the curves do not change as will be seen later. This is likely due to the loss of capacity in the SnCoC coin

cell with cycling, as evidenced by the voltage curve in Figure 5.3. There, the width of the cycle shortens significantly from the first cycle to the second. As each run takes 3220s, the x-axis is proportional to time. There is also a significant widening of the measured range of SAXS data at high scattering angles (around $q = 0.3$ Å^{-1}). This is a function of the concentration of SnCo grains in the material, which cause grain-grain interference as described in Chapter 3. It is not fitted by the Kalliat model used to describe the grains, as "dilute" particles or pores are assumed in the theoretical development of the model. However, this part of the SAXS signal is of little practical use as it has no impact on the examination of SnCo grain size and so can be safely ignored.

5.3 QUANTITATIVE OBSERVATIONS

The SnCoC data can be effectively described by the Kalliat model given in Chapter 3, with two or three components: a Kalliat "pore" term (here used for grains instead), a background, and a Porod's Law term with an n value varying from $n = 2$ to $n = 3$. This can be written in similar form to the carbons of Chapter 4:

$$I(q) = \frac{A}{q^n} + \frac{B_{gr}}{\left(1 + a^2 q^2\right)^2} + D, \tag{5.2}$$

where A is proportional to the surface area of SnCoC particles and n is a constant related to the mass fractal value. n values between 2 and 3 are indicative of "mass fractals", where particles are arranged in a fractal structure [52]. B_{gr} is proportional to the surface

area of SnCo grains, *a* is the Debye autocorrelation length of the grains, related to the radius of gyration in Chapter 3.

and D is a constant background term. The SnCoC data for high voltages (delithiated electrode) uses all three terms, while the data for low voltages (lithiated electrode) uses just the Kalliat pore/grain term combined with a background term. Typically, the latter case fits Porod's Law terms with $n < 1$ instead of a constant *D*: this has the effect of creating a slightly slanted background that partially compensates for the previously mentioned grain-grain interference that is apparent at high *q*. Fitting error is expressed in Chapter 2 as a chi-squared value:

$$\chi^2 = \sum_{i=1}^{n} (\ln(Icalc_i)) - (\ln(Idata_i))^2, \tag{5.3}$$

where $Icalc_i$ are fitted data points and $Idata_i$ are experimental data points. The error generally increases as the SnCoC electrode becomes lithiated and the Porod's Law component disappears.

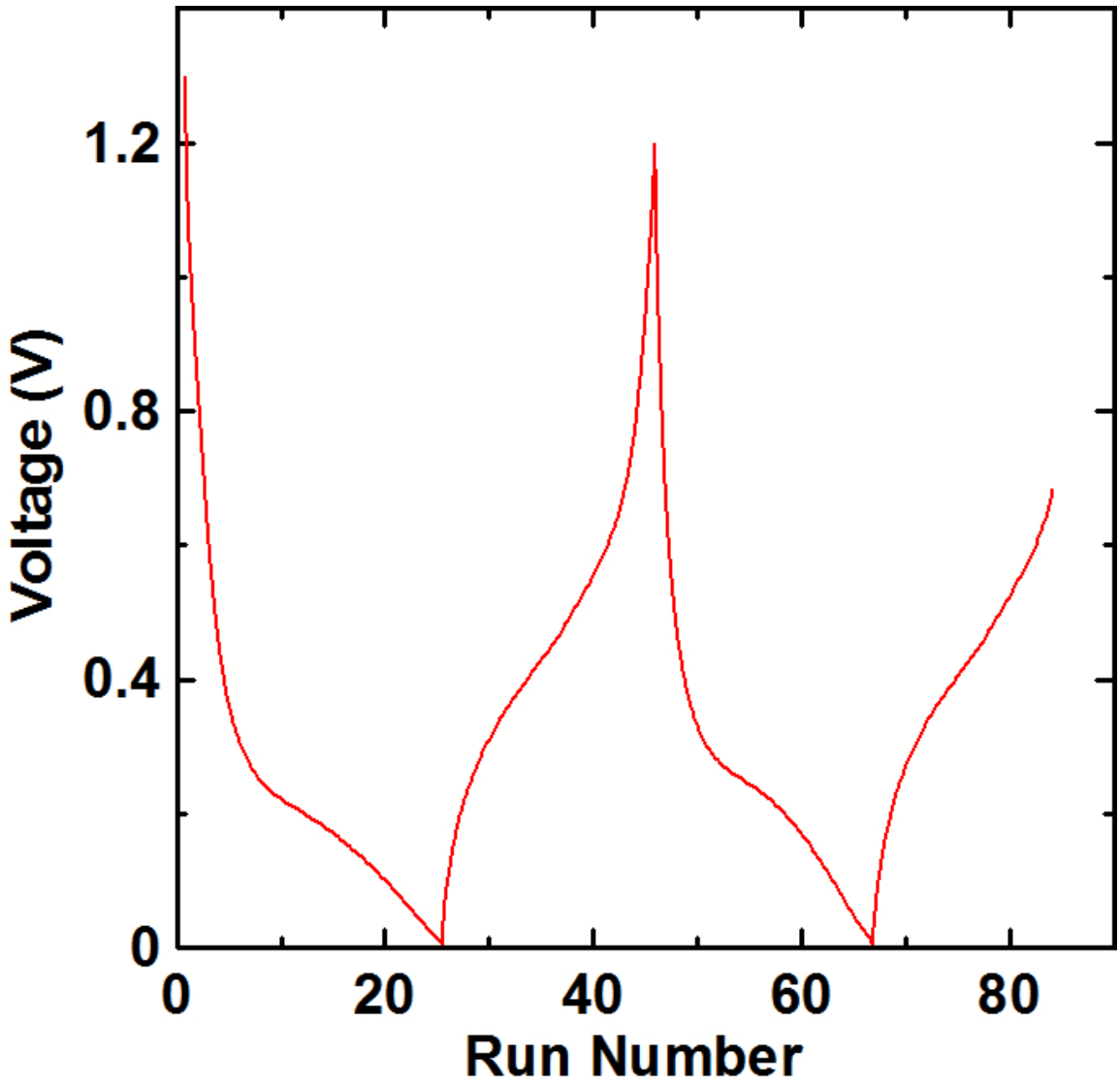

Figure 5.3 Cell voltage versus SAXS run number corresponding to the data shown in Figure 5.2.

Figure 5.4 shows four sets of SnCoC data along with their Kalliat model fits. The curves in Figure 5.4 a) are different from those in b) as the lithiation of the grains causes the Kalliat term to grow greatly in intensity while the Porod's Law term shrinks and eventually becomes negligible (except as a slanted background, described above). In Figure 5.4 a) and b), the two curves are separated by a small amount, presumably due to

cell capacity changes: the shift in b) from the first lithation to the second is enough to change the radius of gyration by a small amount as the grains hold less lithium ions.

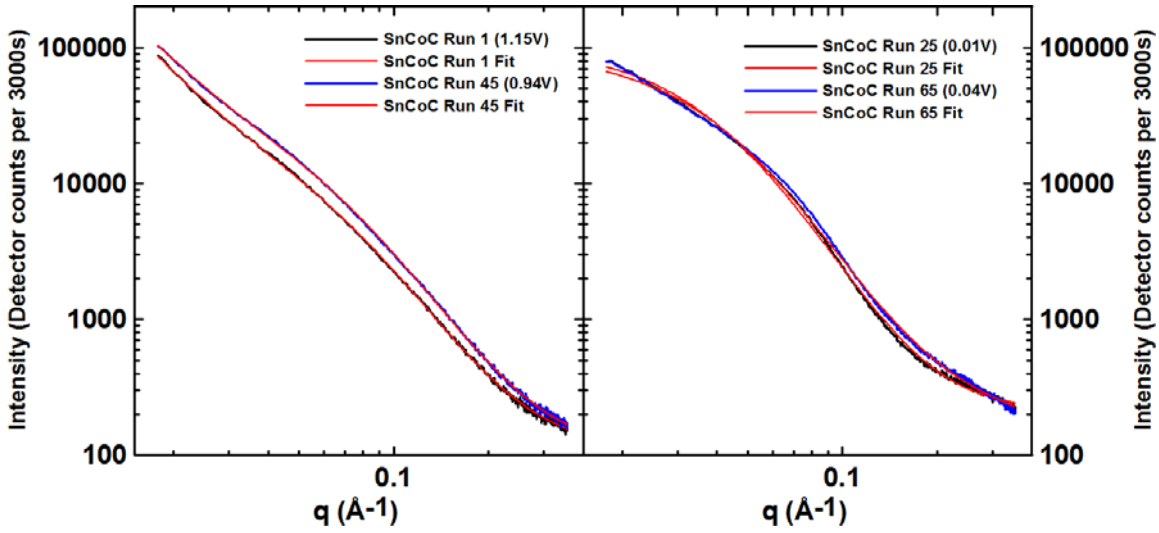

Figure 5.4 SAXS data of SnCoC a) fully delithiated and b) fully lithiated, along with respective fits.

From Figure 5.4 a) to b) the difference in intensity of the SnCo grain contribution is very large, while the Porod's Law term disappears. The radius of gyration that corresponds to the grain term also increases substantially, as is expected for the lithiation of grains. Figure 5.5 more closely examines two of the curves in Figure 5.4, with fit components detailed. The difference in fitting error between delithiated and lithiated data can be seen in the graph.

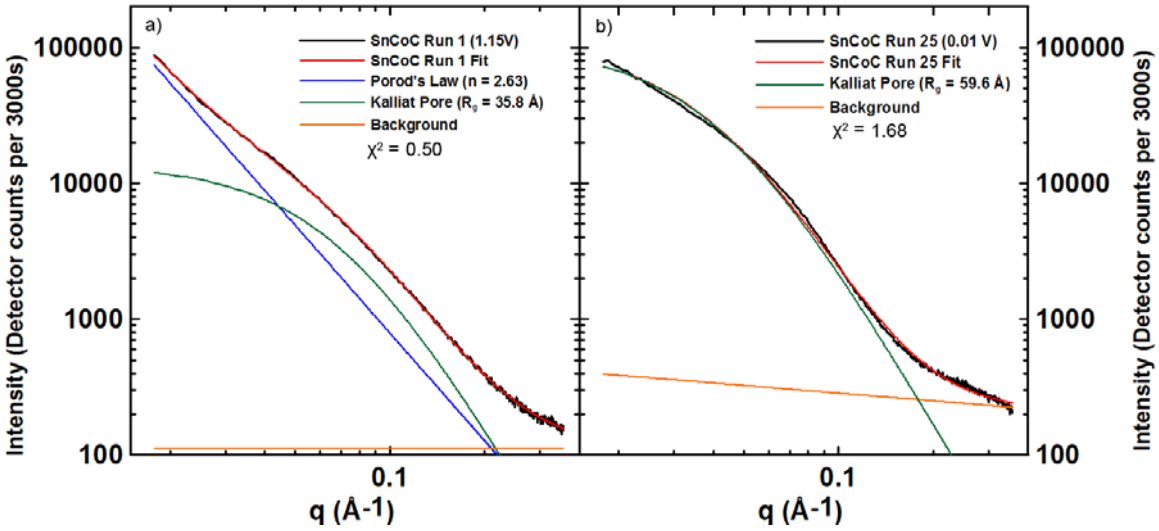

Figure 5.5 SAXS data of SnCoC a) fully delithiated and b) fully lithiated, along with respective fits and their components.

The data from every second run was fitted with the Kalliat model, with full results found in Table A.3 in Appendix 1. Figure 5.6 shows both voltage and radius of gyration plotted versus run number, which yields important results. Radius of gyration steadily increases from its base value of about 36 Å as the cell is discharged and lithium ions enter the SnCo grains. The radius of gyration peaks at about 60 Å when voltage drops below 0.2 V, then shrinks back to 36 Å as the cell is charged and lithium ions leave the grains. This is repeated during a second cycle, except with the second plateau being a slightly smaller size, 56 Å, and as cell capacity is decreased during the second cycle the plateau "width" is smaller.

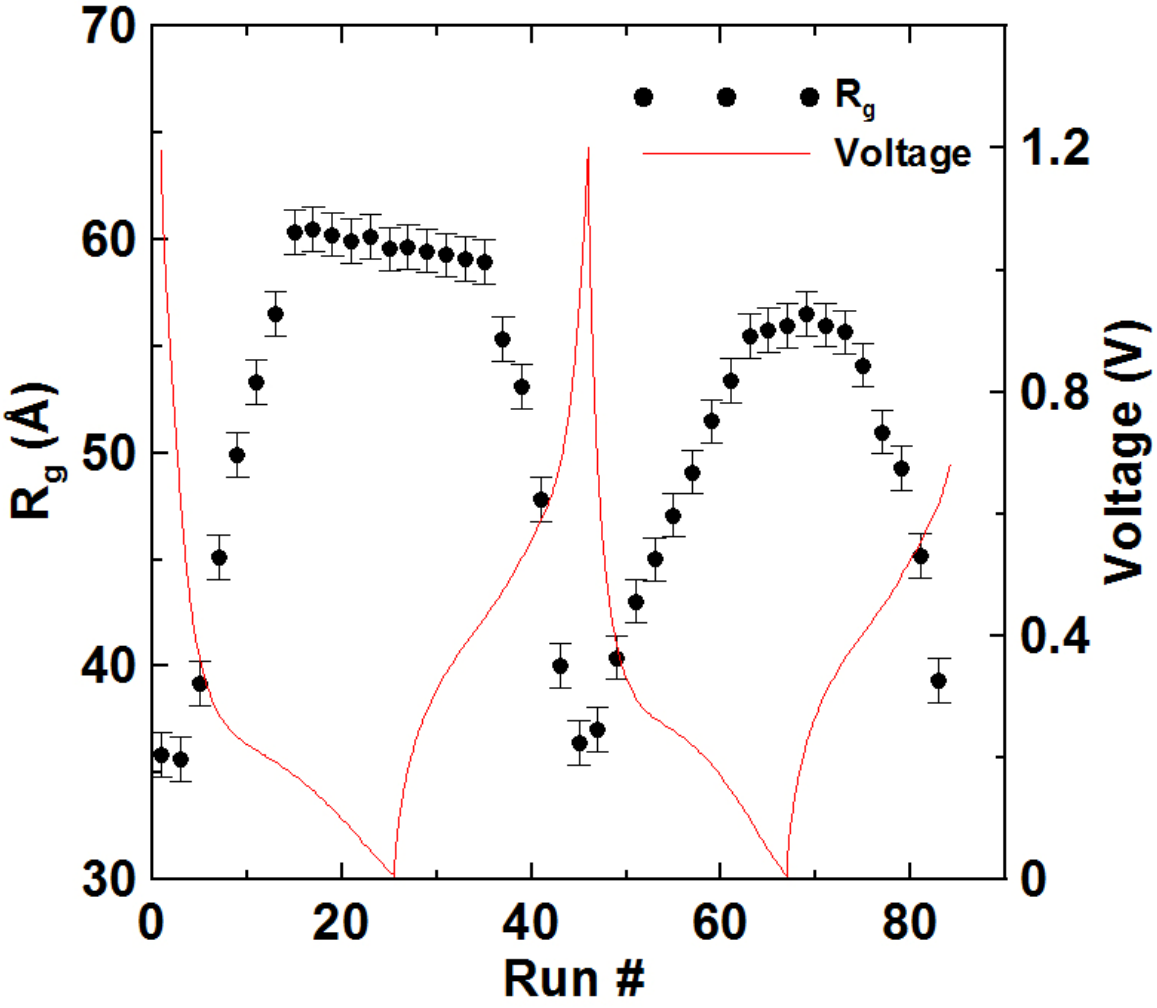

Figure 5.6 Radius of gyration (black points) and voltage (red line) data for the set of SnCoC SAXS runs. Radius of gyration plateaus can be found from Runs 15 to 35 and 63 to 73.

5.4 ELECTRODE LITHATION

Figure 5.6 suggests some important details of the process of lithiation in SnCoC. As the radius of gyration plateaus at about 0.2 V during cell discharge, this means that the SnCo grains are fully lithiated and cannot increase further in size. However, since the cell has

still more capacity, this means that the additional lithiation from 0.2 V to 0.005 V must be handled by the carbon matrix of the electrode. The delithiation process can be described similarly: up to 0.4 V the grain size is unchanged, meaning the carbon is giving up lithium ions first, then the SnCo grains.

The voltage curve in Figure 5.3 has inflection points at approximately Runs 15 and 60 (discharged to about 0.2 V), which mark the point that SnCo grains have been fully lithiated and the remainder of the cell discharge is due to carbon alone. This analysis can be corroborated by the Mossbauer spectroscopy contained in reference [53].

Since the lithiation and delithiation of SnCo grains can be separated from that of the carbon matrix, an examination of the volume change of the grains can be made with regards to previous studies of the lithiation of SnCo. It is known that the molar volume of lithiated tin compounds is linearly dependent on the molar ratio between lithium and tin, with a slope of 8.9 +/- 0.5 mL/mol [54]. This can be combined with the volume calculation method in reference [55]:

$$\Delta V = \frac{kx}{v_0} \times 100\%, \tag{5.4}$$

where ΔV is the percent change in volume, k is 8.9 +/- 0.5 mL/mol, x is the number of moles of Li per mole Sn, and v_0 is the initial volume. Assuming x is the maximum lithiation potential of Sn, 4.4 Li atoms per Sn atom, the maximum volume expansion of $Sn_{50}Co_{50}$ should be 170 +/- 10%. Using the Kalliat model grain size method, where R_g

increases from 35.8 Å to 59.6 Å, a volume expansion of 360 +/- 70% is calculated. This is substantially higher than the theoretical value, although the second charge/discharge cycle with maximum R_g of 56 Å yielded a volume expansion of 280 +/- 60%, much closer to the theoretical value. Further study is currently underway on this system to explain the discrepancy. It is possible that the Kalliat grain term is also fitting nanometre-scale features in the carbon along with the SnCo grains, increasing the lithiated R_g value.

CHAPTER 6 CONCLUSION

6.1 SUMMARY OF RESULTS

The purpose of this work was to give and explain SAXS data relating to two quite different systems: impregnated activated carbons and nanostructured $Sn_{30}Co_{30}C_{40}$ Li-ion battery electrode material. The two systems required separate methods of production and collection of raw data, but shared a modified Kalliat model for analysis.

The essential takeaways from the studies on impregnated carbons were that different chemical species behave in rather drastically dissimilar ways in terms of their distribution in the carbons. Three of the compounds, namely sodium benzoate, potassium biphthalate, and zinc chloride, effectively dispersed over all classes of pores in the carbon, a behaviour labeled as Type A. The other two compounds, potassium carbonate and silver nitrate, mainly formed large grains in the more sizeable pores and neglected to deposit in smaller grains or fill micropores, a behaviour called Type B. The modified Kalliat model and related assumptions used to gather and interpret SAXS data are not particularly complex and are exceedingly quick and easy to put into use, at the cost of neglecting minor contributions to scattering intensity from secondary effects such as pore-pore interference. This allows many samples to be analyzed quickly while maintaining interpretive accuracy, and reasonable fits to the experimental data were demonstrated at various loadings. Ultimately, knowledge on the dispersion habits of various chemicals in activated carbons is useful to many industrial applications of filtration technology.

As for the nanostructured alloy of $Sn_{30}Co_{30}C_{40}$, an in-situ SAXS experiment was developed to allow coin cells containing the electrode to be simultaneously charged and scanned. The same modified Kalliat model used to describe the activated carbons was effectively applied to this system, once the SAXS signal of the electrode was isolated, as the electrode material could be thought of as SnCo grains in a carbon matrix. When the electrode material was lithiated and delithiated (by discharging and charging the cell), the SAXS data, along with the model, evidenced a clear change in grain size. The peaks of grain size also correlated with the lithiation of carbon starting around 0.2 V (on the discharge), as grains stopped lithiating and further cell capacity was due to carbon alone.

6.2 FUTURE WORK

The studies here can easily be extended to many different systems. Under the umbrella of IAC studies, many more chemical species could be examined for impregnation behaviour and under different conditions than those given in this work. Contact angle measurement data could be correlated with SAXS information as well as SEM and WAXS data to give more fully described pictures of the behaviour (in some cases, literally) of a given impregnant. Different examples of dispersal behaviour beyond Type A and Type B could be hunted for. It is plausible to imagine a chemical species that belongs to some Type C, filling micropores and depositing small grains, yet largely avoiding the formation of sizeable grains. This has been seen when co-impregnating with nitric acid in other work [29], but it may also occur natively, without the use of a co-impregnant. With enough data from different species, the difference between Type A, B, etc could be quantified as

well: the statistical analysis of many impregnants could yield numerical floors or ceilings on micropore filling, micrograin formation or large grain formation per unit chemical loading.

For the species given in this work, the carbon base was Kuraray GC brand, which is highly microporous. Similar experiments on different types of carbon, especially those with different porosity distributions, could yield interesting results as it is likely the availability of pores affects the behaviour of a given chemical impregnant.

One other possible study related to impregnated activated carbons would be a test of the limits of SAXS and the modified Kalliat model for low-loading samples. Many industrially relevant carbon impregnants are not used at very high loadings, while most of the samples described in this work are at 15-20% loading or higher. It would be interesting to find the lower limit on loading of a given "Type" that could be effectively analyzed using the simple methods used here.

On the topic of nanostructured Li-ion electrode materials, many other substances similar to SnCoC could be studied using the in-situ apparatus created for the work in this thesis. Depending on the exact structure, the modified Kalliat model may or may not apply, but a similar strategy to that of the $Li/Sn_{30}Co_{30}C_{40}$ cell for collecting and analyzing data could be very effective in uncovering aspects of voltage curves that have been previously unexplainable. Correlating cell voltages with important parameters such as grain size

seems a versatile and malleable approach and may yield information on the charge capacities of various components in an electrode material.

Finally, the modified Kalliat model may be applied toward other porous materials such as nanostructured metal oxides or even more complex three-phase systems of base matrix, pore and grain that can be approximated into sets of two-phase systems as done here. Such a versatile model can be used in a wide range of possible systems for quickly and accurately analyzing SAXS data.

APPENDIX 1

Atom	a_1	b_1	a_2	b_2	a_3	b_3	a_4	b_4	c
C	2.31	20.8439	1.02	10.2075	1.5886	0.5687	0.865	51.6512	0.2156
Al	6.4202	3.0387	1.9002	0.7426	1.5936	31.5472	1.9646	85.0886	1.1151
Cu	13.338	3.5828	7.1676	0.247	5.6158	11.3966	1.6735	64.8126	1.191

Table A.1 The coefficients of the atomic form factor model of Equation 3.13 for three different atoms: carbon, aluminum, and copper. Taken from reference [33].

% loading	A	n	b (Å)	$C_{mi} \times 10^{-22}$ (cm^6 / g)	a (Å)	$B_{gr} \times 10^{-22}$ (cm^6 / g)	V_{gr} (cm^3/g)	V_x / V_{mi}	X^2
10 ± 1	0.43 ± .03	3.6 ± 0.2	2.58 ± 0.02	2.14 ± 0.06	8.5 ± 0.2	3.4 ± 0.1	0.03 ± 0.02	0.08 ± 0.07	2.0 ± 0.1
0 (NaBz)	0.43	3.6	2.58	2.14	0	0	0	0	2.0
5	0.66	3.5	2.58	2.34	8.5	3.4	0.03	-0.2	3.5
10	0.65	3.5	2.58	2.30	8.5	8.7	0.07	0	5.5
15	0.30	3.7	2.58	2.05	8.5	14.4	0.11	0.08	3.7
21	0.30	3.8	2.58	1.69	8.5	18.7	0.15	0.21	6.1
26	0.35	3.7	2.58	1.32	8.5	19.6	0.15	0.35	6.0
40	0.46	3.7	2.58	0.76	8.5	18.2	0.14	0.63	2.9
50	0.77	3.6	2.58	0.64	8.5	12.5	0.10	0.70	1.5
0 (KHP)	0.44	3.6	2.60	2.19	0	0	0	0	2.0
5	0.34	3.8	2.60	2.29	8.4	4.8	0.04	0	3.0
10	0.22	3.7	2.60	2.26	8.4	11.6	0.09	0.01	3.9
15	0.73	3.5	2.60	1.84	8.4	14.0	0.11	0.14	3.8
20	0.57	3.6	2.60	1.55	8.4	17.1	0.14	0.24	3.5
25	1.03	3.5	2.60	1.39	8.4	18.5	0.15	0.30	3.9
40	1.85	3.4	2.60	0.84	8.4	19.7	0.16	0.54	4.3
50	2.56	3.3	2.60	0.42	8.4	12.0	0.10	0.78	4.4
70	4.52	3.3	2.60	0.22	8.4	6.5	0.05	0.94	2.8
0 ($ZnCl_2$)	4.69	3.6	2.55	2.34	0	0	0	0	2.2
5	0.55	3.6	2.55	2.53	3.6	0.5	0.05	-0.04	2.5
10	0.62	3.6	2.55	2.03	3.6	1.3	0.13	0.05	3.2
14	0.93	3.5	2.55	1.61	3.6	1.5	0.15	0.13	4.1
20	1.72	3.4	2.55	1.33	3.6	2.1	0.21	0.20	5.7
25	1.06	3.5	2.55	0.92	4.0	2.5	0.19	0.31	6.0
41	0.55	3.7	2.55	0	4.9	5.0	0.20	n/a	4.5
71	0.41	3.9	2.55	0	7.6	9.0	0.10	n/a	4.8
89	0.38	4.0	2.55	0	8.9	9.2	0.06	n/a	3.8
0 (K_2CO_3)	0.39	3.6	2.60	2.36	0	0	0	0	2.1
5	1.16	3.4	2.60	2.10	11.0	5.2	0.02	0.04	1.6
10	1.08	3.4	2.60	2.16	11.0	9.6	0.03	0.03	0.7
15	1.34	3.4	2.60	1.85	11.0	13.8	0.05	0.10	2.5
20	2.13	3.3	2.60	1.83	11.0	16.7	0.06	0.11	1.0
0 ($AgNO_3$)	0.46	3.6	2.56	2.45	0	0	0	0	2.1
4	0.35	3.7	2.56	2.52	7.9	0	0	-0.01	2.4
9	0.52	3.5	2.56	2.08	7.9	0	0	0.01	2.2
14	0.42	3.7	2.56	2.58	7.9	0.1	0	-0.01	3.2
20	0.28	3.8	2.56	2.59	7.9	0.3	0	-0.02	3.7
25	0.21	3.9	2.56	2.46	7.9	0.5	0.01	0	3.9
48	0.39	3.9	2.56	1.92	7.9	0.9	0.01	0.02	2.3
67	1.76	3.6	2.56	1.15	7.9	1.1	0.01	0.07	0.9

Table A.2 Parameters from fits to the SAXS data graphed in Figures 4.2 through 4.7, as well as other salient calculations. Data is listed by impregnant.

Run	A	B_{gr}	D	Rg (Å)	n	Error	Voltage (V)
	1.83 ± .03 (A < 15), 160 ± 3 (A > 15)	0.30 ± 0.1	110 ± 10	36 ± 1	2.6 ± 0.2 (n > 2), .06 ± .03 (n < 2)	0.5 ± 0.1	1.15 ± 0.01
1	1.83	0.30	110	36	2.6	0.5	1.15
3	2.04	0.33	120	36	2.6	0.4	0.62
5	1.99	0.34	120	39	2.6	0.4	0.36
7	1.55	0.32	120	45	2.7	0.5	0.27
9	0.87	0.33	130	50	2.8	0.5	0.23
11	0.31	0.34	140	53	3.0	0.4	0.21
13	0.11	0.34	150	57	3.0	0.5	0.19
15	160	0.34	0	60	0.06	0.6	0.17
17	36	0.33	150	60	0.04	0.7	0.15
19	44	0.33	150	60	0.03	0.8	0.12
21	202	0.32	0	60	0.05	1.0	0.08
23	187	0.31	0	60	0.15	1.3	0.05
25	184	0.29	0	60	0.19	1.7	0.01
27	165	0.28	0	60	0.32	1.7	0.18
29	141	0.27	0	59	0.49	1.7	0.28
31	128	0.26	0	59	0.58	1.5	0.34
33	116	0.26	0	59	0.63	1.3	0.39
35	108	0.25	0	59	0.66	1.1	0.43
37	4.30	0.21	170	55	2.2	0.8	0.47
39	4.70	0.21	140	53	2.3	0.6	0.53
41	4.98	0.22	110	48	2.3	0.3	0.59
43	3.81	0.32	100	40	2.5	0.4	0.68
45	2.88	0.40	100	36	2.6	0.4	0.94
47	2.43	0.40	110	37	2.6	0.4	0.68
49	2.11	0.37	110	40	2.6	0.4	0.39
51	1.45	0.38	120	43	2.7	0.3	0.30
53	0.98	0.40	140	45	2.7	0.4	0.26
55	0.96	0.39	160	47	2.7	0.5	0.24
57	1.27	0.37	170	49	2.5	0.7	0.22
59	2.10	0.35	180	51	2.3	1.0	0.19
61	3.82	0.33	170	53	2.1	1.4	0.15
63	111	0.35	0	55	0.59	1.5	0.10
65	105	0.34	0	56	0.64	1.6	0.05
67	103	0.32	0	56	0.67	1.8	0.04
69	87	0.30	0	56	0.85	1.8	0.22
71	81	0.30	0	56	0.92	1.7	0.30
73	75	0.29	0	56	0.96	1.5	0.36
75	10.51	0.24	130	54	2.0	1.5	0.40
77	6.19	0.24	140	51	2.2	1.0	0.45
79	6.11	0.24	120	49	2.2	0.6	0.50
81	5.37	0.25	100	45	2.3	0.4	0.55
83	3.75	0.35	100	39	2.5	0.4	0.62

Table A.3 Kalliat model fitting variables, given for every second SnCoC data set.

REFERENCES

[1] Tokumoto MS, Pulcinelli SH, Santilli CV, Craievich AF. SAXS study of the kinetics of formation of ZnO colloidal suspensions. Journal of Non-Crystalline Solids 1999; 247(1):176-82.

[2] Prosa TJ, Bauer BJ, Amis EJ, Tomalia DA, Scherrenberg R. A SAXS study of the internal structure of dendritic polymer systems. Journal of Polymer Science B: Polymer Physics 1997; 25(17):2913-24.

[3] Dubinin MM, Plavnik GM. Microporous structures of carbonaceous adsorbents. Carbon 1968; 6(2):183-92.

[4] Kalliat M, Kwak CY, Schmidt PW. Small-angle x-ray investigation of the porosity in coals. New Approaches in Coal Chemistry (Washington, DC): American Chemical Society, 1981; p. 4-22

[5] Lozano-Castelló D, Raymundo-Piñero E, Cazorla-Amorós D. Characterization of pore distribution in activated carbon fibers by microbeam small angle X-ray scattering. Carbon 2002; 40(14):2727-35.

[6] Diduszko R, Swiatkowskib A, Trznadel BJ. On surface of micropores and fractal dimension of activated carbon determined on the basis of adsorption and SAXS investigations. Carbon 2000; 38(8):1153-62.

[7] Stevens DA, Dahn JR. An in situ small-angle X-ray scattering study of sodium insertion into a nanoporous carbon anode material within an operating electrochemical cell. J. Electrochem Soc 2000; 147(12):4428-31.

[8] Svergun DI, Koch MHJ. Advances in structure analysis using small-angle scattering in solution. Current Opinion in Structural Biology 2002; 12(5):654-60.

[9] Putnam CD, Hammel M, Hura GL, Tainer JA. X-ray solution scattering (SAXS) combined with crystallography and computation: defining accurate macromolecular structures, conformations and assemblies in solution. Quarterly Reviews of Biophysics 2007; 40(3):191-285.

[10] Heijman SGJ, Hopman R. Activated carbon filtration in drinking water production: model prediction and new concepts. Colloids and Surfaces A 1999; 151(1):303-9.

[11] Wood GO. Activated carbon adsorption capacities for vapors. Carbon 1992; 30(4):593-9.

[12] Wood GO, Moyer ES. A review of the wheeler equation and comparison of its applications to organic vapor respirator cartridge breakthrough data. Am. Ind. Hyg. Assoc. J. 1989; 50(8):400-7.

[13] Rouquerol J, Avnir D, Fairbridge CW, Everett DH, Haynes JH, Pernicone N, et al. Recommendations for the characterization of porous solids. IUPAC Zurich, Switzerland, 1994.

[14] Guo J, Morris JR, Ihm Y, Contescu CI, Gallego NC, Duscher G et al. Topological defects: origin of nanopores and enhanced adsorption performance in nanoporous carbon. Small 2012; 8(21):3283-88.

[15] Smith JWH. Investigation of copper based impregnation recipes for the optimization of respirator carbons. Halifax, NS, Canada. Dalhousie University, MSc thesis, 2008.

[16] Zeng H, Jin F, Guo J. Removal of elemental mercury from coal combustion flue gas by chloride-impregnated activated carbon. Fuel 2004; 83(1):143-6.

[17] Fortier H, Zelenietz C, Dahn TR, Westreich P, Stevens DA, Dahn JR. SO2 adsorption capacity of K2CO3-impregnated activated carbon as a function of K2CO3 content loaded by soaking and incipient wetness. Appl. Surf. Sci. 2007; 253(6):3201-7.

[18] Tseng HH, Wey MY. Study of SO2 adsorption and thermal regeneration over activated carbon-supported copper oxide catalysts. Carbon 2004; 42(11):2269-78.

[19] Fortier H, Westreich P, Selig S, Zelenietz C, Dahn JR. Ammonia, cyclohexane, nitrogen and water adsorption capacities of an activated carbon impregnated with increasing amounts of ZnCl2, and designed to chemisorb gaseous NH3 from an air stream. J. Colloid Interface Sci. 2008; 320(2):423-35.

[20] Smith JWH, Romero JV, Dahn TR, Dunphy K, Sullivan C, Mallay M, et al. The effect of heating temperature and nitric acid treatments on the performance of Cu- and Zn-based broad spectrum respirator carbons. J. Colloid Interface Sci. 2011; 364(1):178-94.

[21] Fortier H. The science of impregnation and the optimization of the performance of impregnated activated carbons for gas mask applications. Halifax, NS, Canada, Dalhousie University, PhD thesis, 2007.

[22] Westreich P, Fortier H, Flynn S, Foster S, Dahn JR. Exclusion of salt solutions from activated carbon pores and the relationship to contact angle on graphite. J. Phys. Chem. C 2007; 111(9):3680-4.

[23] Ferguson P. Studies of tin-transition metal-carbon alloys prepared by mechanical milling for lithium-ion battery negative electrodes. Halifax, NS, Canada, Dalhousie University, PhD thesis, 2009.

[24] Tian Y, Timmons A, Dahn JR. In situ AFM measurements of the expansion of nanostructured Sn-Co-C films reacting with lithium. J. Electrochem. Soc. 2009; 156(3): A187-91.

[25] Brunauer S, Emmett PH, Teller EJ. Adsorption of gases in multimolecular layers. J. Am. Chem. Soc 1938; 60(2):309-19.

[26] Westreich P, Selig S, Fortier H, Dahn JR. Two distinct Langmuir isotherms describe the adsorption of certain salts onto activated carbon over a wide concentration range. Carbon 2006; 44(14):3145-48.

[27] Boehm HP, Some aspects of the surface chemistry of carbon blacks and other carbons. Carbon 1994; 32 (5) 759-69.

[28] Fan Q Chupas PJ, Whittingham MS. Characterization of amorphous and crystalline tin-cobalt anodes. Electrochemical and Solid State Letters 2007; 10:A274-8

[29] Cullity BD, Stock SR. Elements of X-ray diffraction. 3rd ed. New Jersey: Prentice Hall. 2001:664.

[30] Smith JWH. A study of respirator carbons. Halifax, NS, Canada. Dalhousie University, PhD thesis, 2012.

[31] Guinier A. X-ray diffraction in crystals, imperfect crystals, and amorphous bodies. 2nd ed. San Francisco CA: WH Freeman, 1963.

[32] Guinier A, Fournet G. Small-angle scattering of X-rays. New York: John Wiley & Sons, 1955.

[33] Kittel C. Introduction to solid state physics. 8th ed. Hoboken NJ: John Wiley & Sons, 2005.

[34] Brown PJ, Fox AG, Maslen EN, O'Keefe MA, Willis BTM. Intensity of diffracted intensities. International Tables for Crystallography 2006; Vol. C: 554-95.

[35] Glatter O, Kratky O. Small-angle X-ray scattering. New York NY: Academic Press, 1982.

[36] Ciccariello S, Goodisman J, Brumberger H. On the Porod law. J. Appl. Cryst. 1988; 21:117-28.

[37] Debye P, Anderson HR, Brumberger H. Scattering by an inhomogeneous solid. II. The correlation function and its application. J. Appl. Phys. 1957; 28:679-83.

[38] Buiel ER, George AE, Dahn JR. Model of micropore closure in hard carbon prepared from sucrose. Carbon 1999; 37(9):1399-1407.

[39] Gibaud A, Xue JS, Dahn JR. A small angle X-ray scattering study of carbons made from pyrolyzed sugar. Carbon 1996; 34(4):499-503.

[40] Dash R, Chmiola J, Yushin G, Gogotsi Y, Laudisio G, Singer J, Fischer J, Kucheyev S. Titanium carbide derived nanoporous carbon for energy-related applications. Carbon 2006; 44(12):2489-97.

[41] Laudisio G, Dash RK, Singer JP, Yushin G, Gogotsi Y, Fischer JE. Carbide-Derived Carbons: A Comparative Study of Porosity Based on Small-Angle Scattering and Adsorption Isotherms. Langmuir 2006; 22(21):8945-50.

[42] Zheng T, Xing W, Dahn JR. Carbons prepared from coals for anodes of lithium-ion cells. Carbon 1996; 34(12):1501-07.

[43] Yang R, Dahn TR, Dahn JR. Fe–N–C Oxygen-Reduction Catalysts Supported on "Burned-Off" Activated Carbon. J. Electrochem. Soc. 2009; 156(4):B493-98.

[44] László K, Czakkel O, Josepovits K, Rochas C, Geissler E. Influence of surface chemistry on the SAXS response of polymer-based activated carbons. Langmuir 2005; 21(18):8443-51.

[45] Dubinin MM, Astakhov VA. Development of the concepts of volume filling of micropores in the adsorption of gases and vapors by microporous adsorbents. Russian Chem. Bulletin 1971; 20(1):3-7.

[46] Chen SG, Yang RT. Theoretical basis for the potential theory adsorption isotherms. The Dubinin-Radushkevich and Dubinin-Astakhov equations. Langmuir 1994; 10(11):4244-9.

[47] Kalliat M, Kwak CY, Schmidt PW. Small angle X-ray scattering measurement of porosity in wood following pyrolysis. Wood Sci. Technol. 1983; 17(4):241-57.

[48] Dékány I, Turi L, Homonnay Z, Vértes A, Burger K. Preparation of nanosize FeS particles on SiO2 and clay mineral supports: SAXS and Mössbauer spectroscopic measurements. Colloids Surfaces A: Physicochem. Eng. Aspects 1996; 119(2):195-203.

[49] Stevens DA, Zhang S, Chen Z, Dahn JR. On the determination of platinum particle size in carbon-supported platinum electrocatalysts for fuel cell applications. Carbon 2003; 41(14):2769-77.

[50] Summary Technical Report of Division 10, NDRC, vol. 1, Part 1, Military

Problems with Aerosols and Nonpersistent Gases. Washington, DC, 1946. Available from NTIS, Springfield, VA 22161.

[51] Piccione S, Urbanic JE. Impregnation of carbon with silver. US Patent 3294572, 1966.

[52] Martin JE. Scattering exponents for polydisperse surface and mass fractals. J. Appl. Cryst. 1986; 19(1):25-7.

[53] Ferguson PP, Dunlap RA, Dahn JR. An in situ study of the electrochemical reaction of Li with nanostructured $Sn_{30}Co_{30}C_{40}$. J. Electrochem. Soc. 2010; 157(3):A326-32.

[54] Obrovac MN, Christensen L, Le DB, Dahn JR. Alloy design for lithium-ion battery anodes. J. Electrochem. Soc. 2007; 154(9):A849-55.

[55] Tian Y. In-situ AFM measurements of the expansion of Sn-Co-C films reacting with lithium. Halifax, NS, Canada. Dalhousie University, MSc thesis, 2008.